

# Ultra-peripheral $J/\psi$ production in PbPb collisions at $\sqrt{s_{NN}}=2.76$ TeV with CMS

By

R. Patrick Kenny III

Submitted to the Department of People who read Abstracts and the  
Graduate Faculty of the University of Kansas  
in partial fulfillment of the requirements for the degree of  
Doctor of Philosophy

Committee members

---

MEMBER 1, Chairperson

---

MEMBER 2

---

MEMBER 3

---

MEMBER 4

Date defended: October 02, 2012

The Dissertation Committee for R. Patrick Kenny III certifies  
that this is the approved version of the following dissertation :

Ultra-peripheral  $J/\psi$  production in PbPb collisions at  $\sqrt{s_{NN}}=2.76$  TeV with CMS

---

MEMBER 1, Chairperson

Date approved: October 03, 2012

# Abstract

The first is some L<sup>A</sup>T<sub>E</sub>X code, don't change it.

## **Acknowledgements**

I would like to thank all of the little people who made this thesis possible.

# Contents

<b>1</b>	<b>Introduction</b>	<b>1</b>
1.1	Theoretical Context . . . . .	1
1.2	History . . . . .	1
<b>2</b>	<b>Theory</b>	<b>2</b>
2.1	Introduction . . . . .	2
2.2	QCD/QGP . . . . .	3
2.3	CGC/initial state . . . . .	3
2.4	Weizsäcker-Williams Approximation . . . . .	5
2.5	Vector Meson Dominance . . . . .	10
2.6	Leading Twist Approach Derivation . . . . .	15
2.7	Perturbative Quantum Chromo-dynamics . . . . .	18
2.8	Incoherent Photoproduction . . . . .	20
2.9	Photon Induced Nuclear Break-up . . . . .	20
2.10	Theoretical Results . . . . .	25
<b>3</b>	<b>The CMS Detector</b>	<b>29</b>
3.1	Tracker . . . . .	30
3.2	ECAL . . . . .	31
3.3	HCAL . . . . .	32
3.4	ZDC . . . . .	33

3.5	Muons . . . . .	34
3.6	Trigger . . . . .	38
<b>4</b>	<b>Analysis</b>	<b>41</b>
4.1	MC simulation . . . . .	41
4.2	Trigger development . . . . .	45
4.2.1	L1 trigger . . . . .	46
4.2.2	HLT trigger . . . . .	47
4.3	Event selection . . . . .	47
4.3.1	Data sets . . . . .	48
4.3.2	Event selection cuts . . . . .	49
4.4	Break up determination . . . . .	52
4.4.1	ZDC signal reconstruction . . . . .	52
4.4.2	Determination of the one neutron thresholds . . . . .	54
4.5	Signal extraction . . . . .	56
4.6	Efficiency determination . . . . .	60
4.6.1	Muon efficiencies . . . . .	60
4.6.2	ZDC trigger efficiency . . . . .	66
4.7	Systematic checks . . . . .	67
4.7.1	HF noise threshold . . . . .	67
4.7.2	Template fit normalization . . . . .	69
4.7.3	Mass fit . . . . .	71
4.7.4	MC acceptance . . . . .	72
4.7.5	ZDC reconstruction . . . . .	73
4.7.6	ZDC trigger efficiency . . . . .	75
4.7.7	ZDC reconstruction method comparison . . . . .	77
4.7.8	Tag and probe . . . . .	79
4.7.9	MC vs Data compairson . . . . .	81

<b>5</b>	<b>Results</b>	<b>83</b>
5.1	Coherent cross section . . . . .	83
5.2	Incoherent cross section . . . . .	85
5.3	Break up ratios . . . . .	85
5.4	diMuon-neutron correlations . . . . .	87
<b>6</b>	<b>Conclusion</b>	<b>95</b>
6.1	xsection results . . . . .	95
6.2	correlation results . . . . .	95
<b>7</b>	<b>Future Works</b>	<b>96</b>
7.1	Studies of 2011 PbPb data . . . . .	96
7.1.1	High mass $\gamma - \gamma \rightarrow e^+ e^-$ in PbPb 2011 . . . . .	96
7.1.2	UPC Hadronic Overlap and PbPb 2011 . . . . .	97
7.1.3	UPC with muons in HF . . . . .	99
7.2	Studies of 2013 pPb data and 2015 PbPb data . . . . .	99
7.2.1	pPb $J/\psi$ . . . . .	100
7.2.2	UPC $J/\psi$ and $\Upsilon$ in 2015 . . . . .	101
7.2.3	UPC jets . . . . .	101
<b>A</b>	<b>My Appendix, Next to my Spleen</b>	<b>107</b>

# List of Figures

2.1	A representation of HERA deep inelastic scattering data, which shows the accumulation of low- $x$ partons from Reference [1]. . . . .	4
2.2	The electromagnetic field boosted and at rest. . . . .	5
2.3	The zero and first order modified Bessel functions. . . . .	8
2.4	AB is the pQCD method, RSZ-LTA is the LTA method, and STARlight is the VMD model. . . . .	26
2.5	Nuclear suppression factor, $S$ , in the pQCD and LTA methods. . . . .	27
2.6	Nuclear suppression factor, $S$ , in VMD method. . . . .	28
3.1	The Compact Muon Solenoid from Reference [2]. . . . .	30
3.2	The energy resolution of ECAL as a function of energy from Reference [2]. . . . .	31
3.3	The $E_T$ resolution of HCAL as a function of $ \eta $ and $E_T$ from Reference [2]. . . . .	32
3.4	The CMS muon system showing the four DT stations in the barrel (MB1-MB4), the four CSC stations in the endcap (ME1-ME4), and the RPC stations. . . . .	35
3.5	Schematic of the DT chambers and an individual DT cell. . . . .	35
3.6	Schematic of a RPC cell. . . . .	36
3.7	Schematic of the CSC chambers and an individual CSC cell. . . . .	37
3.8	The amount of material in CMS as a function of $\eta$ in number of interaction lengths. . . . .	38
3.9	The momentum resolution of the muon system using only the tracker and the whole muon system in the barrel (left) and end cap (right). . . . .	38



4.1	Generator level rapidity (left) and $p_T$ (right) distributions for the coherent (black), incoherent (red), and photon-photon process (green). . . . .	44
4.2	The $J/\psi$ polarization of the particle gun (red), coherent (blue), and incoherent samples are plotted as the cosine of the helicity angle. . . . .	44
4.3	Comparison of HF noise distributions in zero bias data, physics triggered data, and MC. . . . .	51
4.4	Average ZDC pluse shape is plotted as the charge as a function of time slice for the first hadronic from $ZDC^-$ (left) and $ZDC^+$ (right). . . . .	53
4.5	The fraction of signal in time slice 5 over time slice 4 as a function of the signal in time slice 5 in $ZDC^-$ (left) and $ZDC^+$ (right). . . . .	54
4.6	Fit to the signal spectra for $ZDC^-$ (left) and $ZDC^+$ (right) . . . . .	55
4.7	ZDC noise spectra from $ZDC^-$ EM section (upper left), $ZDC^+$ EM section (upper right), $ZDC^-$ HAD section (lower left), and $ZDC^+$ HAD section (lower right). . .	56
4.8	Mass fit to $J/\psi$ using Gaussian for the signal and a first order polynomial for the photon-photon continuum . . . . .	57
4.9	Fit to MC $p_T$ templates. . . . .	58
4.10	68%, 95%, and 99% confidence contours from the $p_T$ template fit. . . . .	59
4.11	Simultaneous fit to the mass and $p_T$ spectra. . . . .	59
4.12	68%, 95%, and 99% confidence contours from the simultaneous fit. . . . .	60
4.13	Muon daughter detectability from coherent $J/\psi$ . . . . .	61
4.14	Dimuon acceptance from coherent $J/\psi$ (top left), incoherent $J/\psi$ (top right), and photon-photon interactions (lower). . . . .	62
4.15	Fits to tag and probe pairs in the $J/\psi$ mass region. . . . .	63
4.16	Muon trigger efficiencies in $p_T$ and $\eta$ bins from the tag and probe method. . . . .	64
4.17	The trigger efficiency from tag and probe averaged over candidates in each $(p_T,  y )$ bin. . . . .	65
4.18	The acceptance times averaged trigger efficiency from tag and probe. . . . .	65

4.19	Coherent, incoherent, and photon-photon process $p_T$ template fit to data. . . . .	70
4.20	Various mass distribution fits and the corresponding $p_T$ template fit. . . . .	70
4.21	Mass fit to $J/\psi$ using Gaussian (Left) and Crystal Ball (Right) for the signal and a polynomial for the background . . . . .	71
4.22	Simultaneous fit to the mass and $p_T$ using mass templates for the mass fit. . . . .	72
4.23	Yields corrected by the MC incoherent acceptance map. . . . .	73
4.24	Yields corrected by an unpolarized $J/\psi$ sample. . . . .	74
4.25	Fit to charge spectrum from $ZDC^-$ (left) and $ZDC^+$ (right) using the standard reconstruction method . . . . .	75
4.26	Comparison of the <b>new</b> ZDC reconstruction method and the <b>standard</b> method for $ZDC^-$ (left) and $ZDC^+$ (right). . . . .	77
4.27	Effects of requiring in-time signal in successively more ZDC hadronic channels, no timing, at least <b>one</b> , at least <b>two</b> , at least <b>three</b> , and all <b>four</b> HAD channels have a maximum signal in the fourth time slice. . . . .	78
4.28	Effect of ZDC signal timing requirements after noise subtraction. . . . .	79
4.29	Tag and probe trigger efficiencies from counting (left) compared to fitting (right) .	80
4.30	Comparison of the of the dimuon rapidity distributions between coherent MC sam- ple and Data. . . . .	81
4.31	Comparison of the of the dimuon $\phi$ distributions between coherent MC sample and Data. . . . .	82
4.32	Comparison of the of the dimuon $p_T$ distributions between coherent MC sample and Data. . . . .	82
5.1	Raw yield for the Coherent cross section measurement. . . . .	84
5.2	Corrected yields for the coherent $p_T$ region. . . . .	84
5.3	Ratio between $J/\psi$ yeilds $X_n X_n$ and $1n0n$ break-up modes compared the $X_n 0n$ break-up mode for $J/\psi$ with $p_T$ below 150 MeV. . . . .	86

5.4	Ratio between $J/\psi$ yields $XnXn$ and $1n0n$ break-up modes compared the $Xn0n$ break-up mode for $J/\psi$ with $0.2 < p_T < 1.5$ GeV. . . . .	87
5.5	Transverse momentum distribution of the $J/\psi$ when $J/\psi$ and neutron have the opposite rapidity direction and the transverse momentum distribution of the $J/\psi$ when $J/\psi$ and neutron have the same rapidity direction for low- $p_T$ (top left) and high- $p_T$ (top right) $J/\psi$ . Bottom: Ratios $R_{opp/same}$ for low- $p_T$ ( left) and high- $p_T$ (right) $J/\psi$ . . . . .	89
5.6	Ratio between the transverse momentum distribution of the $J/\psi$ when $J/\psi$ and neutron have the opposite direction and the transverse momentum distribution of the $J/\psi$ when $J/\psi$ and neutron have the same direction. . . . .	90
5.7	Rapidity distribution of the $J/\psi$ when $J/\psi$ and neutron have the opposite rapidity direction and the rapidity distribution of the $J/\psi$ when $J/\psi$ and neutron have the same rapidity direction for low- $p_T$ (top left) and high- $p_T$ (top right) $J/\psi$ . Bottom: Ratios $R_{opp/same}$ for low- $p_T$ ( left) and high- $p_T$ ( right) $J/\psi$ . . . . .	91
5.8	Rapidity ratios $R_{opp/same}$ for low- $p_T$ ( left) and high- $p_T$ ( right) $J/\psi$ . . . . .	91
5.9	Rapidity distribution of $J/\psi$ in the case of the events having the neutron in negative and positive rapidity for the low- $p_T J/\psi$ (top), high- $p_T J/\psi$ (middle) and dimuons from $\gamma\gamma$ sample (bottom). . . . .	93
5.10	$R_{(\mu\mu)^-}^{\varepsilon_{ZDC}(n^-/n^+)}$ and $R_{(\mu\mu)^+}^{\varepsilon_{ZDC}(n^-/n^+)}$ integrated over one side in rapidity for low- and high- $p_T J/\psi$ and also for dimuons from $\gamma\gamma$ sample. . . . .	94
7.1	Coherent excess in inclusive $J/\psi$ $p_T$ spectrum. . . . .	98
7.2	$v$ efficiency times acceptance in CMS from STARlight for $\sqrt{s_{NN}} = 5.1$ TeV as function of $y$ . . . . .	102
7.3	Comparison of $v$ and $J/\psi$ efficiency times acceptance in CMS from STARlight for $\sqrt{s_{NN}} = 5.1$ TeV as function of $p_T$ . . . . .	103

# List of Tables

2.1	$\sigma_{AA \rightarrow AAJ/\psi}(mb)$ the LTA, VMD, pQCD methods. Four different gluon density models are used in the pQCD method. STARlight is a simulation software package that utilizes the VMD model. . . . .	25
4.1	List of 2011 L1 seeds. . . . .	46
4.2	List of 2011 HLT trigger. . . . .	47
4.3	Integrated luminosities and number of events for the three samples used in this analysis. . . . .	49
4.4	Effects of event selection cuts. . . . .	50
4.5	ZDC trigger efficiencies for ZDC reconstruction method 1 and 2 . . . . .	67
4.6	Summary of systematic uncertainties . . . . .	67
4.7	HF noise thresholds for various noise measurement methods. . . . .	68
4.8	Candidate yields below 1.05 GeV $p_T$ for various HF noise cuts. . . . .	68
4.9	Values of the energy cuts for the HF calorimeter for RecHit and CaloTower in GeV. . . . .	69
4.10	Number of dimuon candidates with $p_T < 1.05$ when changing HF calorimeter cuts for RecHit and CaloTower. . . . .	69
4.11	ZDC trigger efficiencies for ZDC reconstruction method 1 and 2 for different trigger samples . . . . .	76
5.1	Number of coherent $J/\psi$ integrated over $p_T$ and $y$ with statistical uncertainty. . . . .	86
5.2	Number of coherent $J/\psi$ integrated over $p_T$ and $y$ with statistical uncertainty. . . . .	87

5.3	Number of $J/\psi$ integrated over $p_T$ and $y$ with statistical uncertainty. . . . .	88
5.4	Number of dimuon pairs for different directions of the neutron rapidity direction together with $R_{(\mu\mu)^-}^{n^-/n^+}$ and $R_{(\mu\mu)^+}^{n^-/n^+}$ . . . . .	92
5.5	Ratios $R_{(\mu\mu)^-}^{\varepsilon_{ZDC}(n^-/n^+)}$ and $R_{(\mu\mu)^+}^{\varepsilon_{ZDC}(n^-/n^+)}$ i.e. $R_{(\mu\mu)^-}^{n^-/n^+}$ and $R_{(\mu\mu)^+}^{n^-/n^+}$ corrected by the $ZDC^+$ and $ZDC^-$ efficiencies. . . . .	92

# **Chapter 1**

## **Introduction**

### **1.1 Theoretical Context**

### **1.2 History**

# Chapter 2

## Theory

### 2.1 Introduction

Microseconds after the big bang, the universe existed in a state known as the Quark Gluon Plasma (QGP). In the QGP, quarks and gluons are not in hadronic bondage, forced to the confines of bound states such as protons and neutrons. The Large Hadron Collider (LHC) produces QGP in the lab in PbPb (lead-lead) collisions. The high energies and rates of the collisions at the LHC make it possible to do detailed studies of the QGP. The LHC is producing rare experimental probes such as suppressed jets and heavy quarkonia at an unprecedented rate in heavy-ion collisions. Physicists now have better constraints on the properties like temperature, viscosity, and energy density of the QGP.

The detailed studies of PbPb collisions coming out of the LHC experiments require an understanding of the initial state of the ions before they collide. Without knowledge of the initial state, physicists cannot determine which experimental effects are due to the QGP and which effects are inherent to the nuclei themselves. For example, suppression of heavy quarkonia is a signature of the QGP but also appears to occur in deuterium-gold collisions where the QGP is not expected to arise [3]. Because it is not certain how much of the reduction of quarkonia production is due to the initial state of the nuclei, the reduction due to the QGP is unclear. Without a clean probe of the

initial state, physicists' knowledge of the QGP is limited. Ultra-Peripheral Collisions (UPC) at the LHC fill this need for a clean probe.

The colliding nuclei interact electromagnetically in an UPC event, avoiding the complicated mixing of final state and initial state effects found in nuclear collisions. In UPC events, no QGP state emerges, and the effects arising from the QGP no longer obscure the initial state effects. Other initial state probes such as peripheral nuclear collisions and proton-nucleus collisions have the potential to create the QGP obscuring which effects come from the initial state. It is impossible to create the QGP in UPC events because the nucleons within the nucleus do not collide. UPC events provide clarity by enhancing physicists' understanding of the initial state.

The interactions between the field of photons surrounding the colliding nuclei and the gluons of nuclei can produce a  $J/\psi$  probing the gluon density. The UPC  $J/\psi$  photoproduction cross section is therefore a probe of the initial state of the nucleus. The Weizsäcker-Williams approximation provides a way to calculate the density of probing photons that surrounds the nucleus. The electron-proton scattering data gives a value for the proton photoproduction cross section at lower energies. The perturbative Quantum Chromo-dynamics (pQCD), Vector Meson Dominance (VMD), and Leading Twist (LTA) methods all combined the nuclear photon flux with the proton scattering data to calculate the nuclear photoproduction cross section. Each of these methods handle the gluon density of the nucleus differently producing a measurable difference in the value of the  $J/\psi$  photoproduction cross section.

## 2.2 QCD/QGP

## 2.3 CGC/initial state

The color glass condensate (CGC) is an effective theory of parton saturation and coupling that aims to explain the initial state of hadronic matter in high energy heavy ions collisions [4]. CGC was developed to calculate the distribution of partons within a nucleus. The theory's name is instructive



of how this is achieved [1]. The first term color steams simply from the fact that the partons carry a color charge. The second terms refers to a coupling within the theory of the low momentum partons to the high momentum partons. In CGC the low momentum partons take on the time scales of the higher momentum partons, which can be described perturbatively. This behavior is analogous to glass, which behaves like a solid on short time scales and a liquid on long time scales. The last term condensate refers to saturation. The CGC predicts that as the hadronic matter is boosted to higher and higher energies, low momentum states are filled and become increasingly less favorable to higher momentum states. In the theory the higher momentum states are treated as the source of the lower momentum states in the same manor that an electron is the source of an electric and magnetic field. This couples the low momentum partons to the weakly coupled high momentum partons.

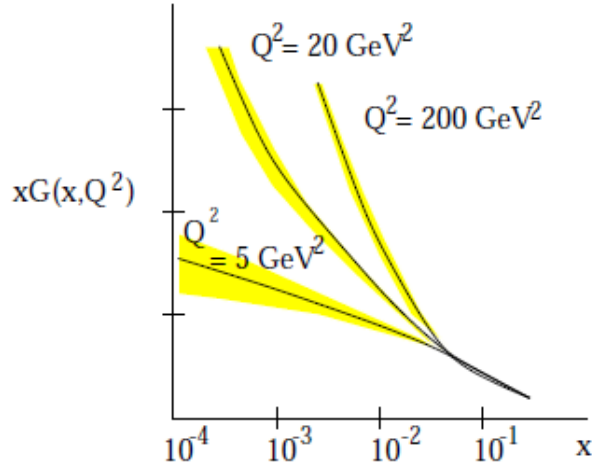


Figure 2.1: A representation of HERA deep inelastic scattering data, which shows the accumulation of low- $x$  partons from Reference [1].

The CGC was inspired by and gives a natural explanation of deep inelastic scattering data. Figure 2.1 gives a representation of the data collected by the HERA experiment. The HERA data shows that as the constituents of a heavy ion are explored the number constituents at lower momentum grows. Following from right to left in Figure 2.1 the gluon density increases as  $x$  decreases, where  $x$  is the fraction of the total momentum the constituent holds. The number of low momentum constituents can not however grow without bound, a plateau must emerge. A

plateau is required in order to assure unitarity, which requires that the probability of scattering off the nucleus does not exceed one. Emergence of a plateau would indicate evidence of saturation, the point where it becomes less favorable to produce more low momentum constituents. As seen in Figure 2.1, the saturation scale increases as the momentum transferred to the probe  $Q^2$  increases. This effect suggests that the saturation scale can be used to measure the running of the strong coupling constant predicted by standard perturbative QCD.

## 2.4 Weizsäcker-Williams Approximation

The Weizsäcker-Williams approximation relates the electric field of a stationary point charge to the photon field that arises at ultra relativistic velocities. The approximation is semi-classical and combines both classical and quantum elements. A Fourier transform of Maxwell's equations combine with Einstein's equation for the energy of a photon in the Weizsäcker-Williams approximation.

The frequency modes of the electrostatic field are treated as photons. The conversion of the electric field to a flux of photons simplifies the calculation of interaction cross sections. The Weizsäcker-Williams approximation makes the calculation of electromagnetic interactions with the nucleus tractable.

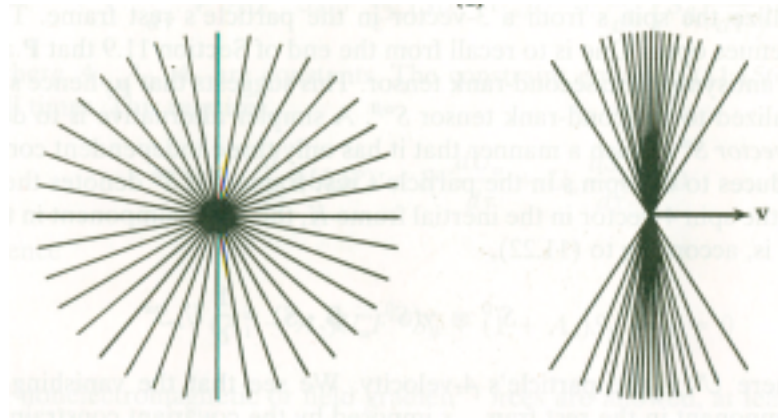


Figure 2.2: The electromagnetic field boosted and at rest.

The Weizsäcker-Williams approximation begins with the equation for the electric field of the projectile nucleus at rest. The electromagnetic field only needs to be considered at the position of

the target nucleus. From the projectile's point of view, the target is moving and contributes  $-vt$  to Eq. 2.1, the equation for the electric field of the projectile nucleus at rest.

$$x' = -vt' \quad y' = b \quad z' = 0 \quad \vec{E}' = \left( \frac{eZ}{4\pi\epsilon_0 \left( (-vt')^2 + b^2 \right)^{3/2}} \right) (-vt'\hat{\mathbf{x}}' + b\hat{\mathbf{y}}') \quad (2.1)$$

In Eq. 2.1,  $b$  is the impact parameter, the distance of separation at closest approach,  $v$  is the velocity of the projectile nucleus,  $Z$  is the number of protons in the nucleus, and  $e$  is the charge of the electron. Two simplifications occur due to the coordinates of Eq. 2.1. The magnetic field is equal to zero, because the projectile is at rest, and the  $z$  coordinate can be ignored, reducing the equation to two dimensions.

The Lorentz transformation converts the field equations in the projectile's frame to equations in the target's frame. The result is a set of equations that relate the electric and magnetic field components in one frame to the components of the electric and magnetic field in another frame moving at a different constant velocity. Eq. 2.2 gives the result of the transformation from the projectile's primed frame to the target's rest frame for the field components [5]:

$$\begin{aligned} E'_x &= E_x & \gamma(E'_y/c + \beta B'_z) &= E_y/c & \gamma(E'_z/c + \beta B'_y) &= E_z/c \\ B'_x &= B_x & \gamma(B'_y - \beta E'_z/c) &= B_y & \gamma(B'_z + \beta E'_y/c) &= B_z \end{aligned} \quad (2.2)$$

The transformation equations for the fields, Eq. 2.2, and the transformation of the coordinates reduce to Eq. 2.3 [5]:

$$\begin{aligned} E'_x &= E_x & \gamma E'_y &= E_y & \gamma \beta E'_y/c &= B_z \\ ct' &= \gamma ct & x' &= -\gamma \beta ct \end{aligned} \quad (2.3)$$

The simplicity of Eq. 2.1 creates the simplicity of Eq. 2.2. The Lorentz transformation reduces the six components of the electromagnetic field in the target's frame to the three equations in Eq. 2.2

by relating them to the fields of the projectile's frame.

The combination of Eq. 2.1 and Eq. 2.2 produce equations for the electric and magnetic fields in the target's rest frame. Eq. 2.1 gives the expression for the field components as seen in the projectile frame.

$$\begin{aligned}\vec{\mathbf{E}} &= \left( \frac{\gamma e Z}{4\pi\epsilon_0 \left( (\gamma vt)^2 + b^2 \right)^{3/2}} \right) (vt\hat{\mathbf{x}} + b\hat{\mathbf{y}}) \\ \vec{\mathbf{B}} &= \frac{\gamma\beta e Z b}{4\pi c \epsilon_0 \left( (\gamma vt)^2 + b^2 \right)^{3/2}} \hat{\mathbf{z}} = \frac{\gamma\mu_0 v e Z b}{4\pi \left( (\gamma vt)^2 + b^2 \right)^{3/2}} \hat{\mathbf{z}}\end{aligned}\quad (2.4)$$

If the impact parameter  $b$  goes to zero, the target sits in the line of the projectile particle's motion, and the denominator carries a factor of  $\gamma$  squared. If  $vt$  goes to zero, the projectile particle is directly above or below in the  $y$  direction, and the numerator carries a factor of  $\gamma$ . This results in fields that are a factor of  $\gamma^3$  higher in the  $y$  direction than in the  $x$  direction (see Fig. 2.2). The boost compresses the electric field of the charge in the direction of the boost and produces a magnetic field resulting in a form similar to radiation. The point charge at ultra relativistic velocities produces a strong electric field in the plane transverse to its motion resembling a plane wave.

Separating the even and odd functions of the electromagnetic field simplify the decomposition of the field equations into Fourier modes. The even functions decompose into cosine functions, odd functions into sine functions. The  $y$ -component of the electric field and the  $z$ -component of the magnetic field are even functions in time, and the  $x$ -component of the electric field is an odd function in time. Eq. 2.5 gives the Fourier transformation integrals.

$$\begin{aligned}E_x(\omega) &= \sqrt{\frac{2}{\pi}} \frac{eZ}{4\pi\epsilon_0 b^2} \int_0^\infty \frac{(\gamma vt/b) \sin(\omega t)}{\left( (\gamma vt/b)^2 + 1 \right)^{3/2}} dt & E_y(\omega) &= \sqrt{\frac{2}{\pi}} \frac{\gamma e Z}{4\pi\epsilon_0 b^2} \int_0^\infty \frac{\cos(\omega t)}{\left( (\gamma vt/b)^2 + 1 \right)^{3/2}} dt \\ B_z(\omega) &= \frac{\beta E_y(\omega)}{c}\end{aligned}\quad (2.5)$$

With the appropriate substitutions, tables provide solutions to the integrals of Eq. 2.5 as seen in Ref. [6].

$$u = \frac{\gamma v t}{b} \quad du \left( \frac{b}{\gamma v} \right) = dt \quad \omega' = \frac{\omega b}{\gamma v}$$

$$\int_0^\infty \frac{u \sin(\omega' u)}{(u^2 + 1)^{3/2}} du = \omega' K_0(\omega') \quad \int_0^\infty \frac{\cos(\omega' u)}{(u^2 + 1)^{3/2}} du = \omega' K_1(\omega') \quad (2.6)$$

The Fourier transformation replaces the time variable with a frequency variable in the field equations. The frequency relates to photon energy by the Einstein's photon energy equation,  $E = \hbar \omega$ . The substitution of time with frequency allows for a flux of photons to replace the classical electromagnetic field.

The  $\gamma$  dependence of the field components is different because of the different  $t$  dependence of Eq. 2.6. The integrals in Eq. 2.6 shift the  $\gamma$  dependence of the field component equations. Eq. 2.7 gives the result of the integrals:

$$E_x(\omega) = \sqrt{\frac{2}{\pi}} \frac{eZ}{4\pi\epsilon_0 b^2} \frac{b}{\gamma v} \frac{\omega b}{\gamma v} K_0\left(\frac{\omega b}{\gamma v}\right) \quad E_y(\omega) = \sqrt{\frac{2}{\pi}} \frac{\gamma eZ}{4\pi\epsilon_0 b^2} \frac{b}{\gamma v} \frac{\omega b}{\gamma v} K_1\left(\frac{\omega b}{\gamma v}\right) \quad (2.7)$$

$\gamma$  is subsumed into the substitution from  $t$  to  $\omega$  in the numerator of the x-component and becomes a part of the zeroth-order modified Bessel function upon integration. The y-component does not have a factor of  $t$  in the numerator, therefore the factor of  $\gamma$  remains outside of the integral, and it does not get subsumed into the first-order modified Bessel function. In Eq. 2.7,  $E_y$  carries an additional factor of  $\gamma$  in the numerator relative to the  $E_x$ .  $E_y$  is  $\gamma$  times larger than  $E_x$ .

In the ultra-relativistic limit, the electric and magnetic fields have the same configuration as electromagnetic plane wave radiation. The electric and magnetic fields are perpendic-

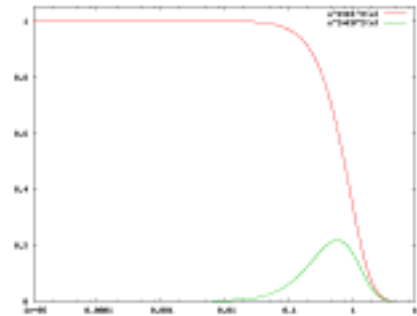


Figure 2.3: The zero and first order modified Bessel functions.

ular and related by a factor of  $c$  in the ultra relativistic limit. When  $v$  approaches  $c$ ,  $\beta \approx 1$ , the y-component of the electric field and the z-component of the magnetic field are related by a factor of  $c$ ,  $E_y/c = B_z$ . Because  $K_0(x)$  is smaller than  $K_1(x)$  for all  $x$ , when  $\gamma \gg 1$ ,  $E_y$  is approximately equally to  $\gamma E_x$ . The conditions imposed by the ultra-relativistic limit result in the relationship of Eq. 2.8.

$$\gamma \gg 1 \rightarrow \gamma E_x \gg E_x \rightarrow E_y \gg E_x \quad (2.8)$$

The x-component of the electric field can therefore be ignored and the magnetic and electric fields are left perpendicular to each other. The six field components reduced to one electric component and one perpendicular magnetic field component, which have a configuration identical to a plane wave.

As with plane waves, the energy per area per time transfered by the electromagnetic field is given by the Poynting vector. The Poynting vector takes the simple form of a plane pulse propagating in the x direction.

$$\vec{S} \equiv \vec{E} \times \vec{B}/\mu_0 = (E_y^2/c\mu_0) \hat{x} = c\epsilon_0 E_y^2 \hat{x} \quad (2.9)$$

The Poynting vector relates to the fluence (energy per unit area) [7],

$$I(b) = \hat{x} \cdot \int_0^\infty \vec{S} d\omega = \int_0^\infty (c\epsilon_0 E_y^2) d\omega = \int_0^\infty \left( \frac{dI}{d\omega} \right) d\omega \quad (2.10)$$

and the spectral fluence (energy per area per frequency).

$$\frac{dI}{d\omega} = c\epsilon_0 E_y^2 = \frac{e^2 Z^2 c}{4\pi^3 b^2 v^2 \epsilon_0} \left( \frac{\omega b}{\gamma v} \right)^2 K_1^2 \left( \frac{\omega b}{\gamma v} \right) = \alpha \hbar \left( \frac{Z}{b\beta\pi} \right)^2 \left( \frac{\omega b}{\gamma v} \right)^2 K_1^2 \left( \frac{\omega b}{\gamma v} \right) \quad (2.11)$$

Substituting Eq. 2.7 into Eq. 2.10 gives the Poynting vector as a function of frequency. Eq. 2.11

paves the way for Einstein's equation. The spectral fluence given by Eq. 2.11 relates the frequency to energy, which are the same quantities present in Einstein's equation.

Einstein's equation,  $E = \hbar\omega$ , gives the energy of a photon, which is related to the spectral fluence. If the fluence is due to a photon number density,  $N$ , Einstein's equation relates  $N$  to the fluence. The relationship between the number of photons per unit area in an infinitesimal energy range and the spectral fluence in an infinitesimal frequency range is given by Eq. 2.12 [5].

$$\frac{dI}{d\omega}d\omega = \hbar\omega N(\omega)d(\hbar\omega) \rightarrow \frac{1}{\hbar^2\omega} \frac{dI}{d\omega} = N(\omega) \quad (2.12)$$

Plugging Eq. 2.11 into Eq. 2.12 yields the semiclassical photon flux of an ultra-relativistic nucleus.

$$N(\omega, b) = \frac{\alpha}{\hbar\omega} \left( \frac{Z}{b\beta\pi} \right)^2 \left( \frac{\omega b}{\gamma v} \right)^2 K_1^2 \left( \frac{\omega b}{\gamma v} \right) \quad (2.13)$$

Eq. 2.13 replaces the classical electric field of a point charge with a semiclassical field of photons. Physicists can calculate the electromagnetic interactions between nuclei with the final result of the Weizsäcker-Williams approximation, Eq. 2.13. The photon flux in Eq. 2.13 provides the electromagnetic input to the  $J/\psi$  photoproduction cross section calculation.

## 2.5 Vector Meson Dominance

The Vector Meson Dominance method for calculating the  $J/\psi$  photoproduction cross section has three main components. VMD approach is constructed from the Weizsäcker-Williams photon flux, the VMD fit to the proton-electron data, and the Glauber model for calculating the nuclear cross sections from the proton-electron cross sections. The Weizsäcker-Williams photon flux provides the probe. The proton-electron scattering data combine with the Glauber model create a picture of the initial state of the nucleus. Each of the different approaches to calculating the UPC  $J/\psi$  photoproduction cross section use these same elements. However, the different models each use the last two elements differently to produce different pictures of the nucleus and different cross

sections values.

The photon flux in the photoproduction cross section calculation must be finite in order for the cross section to be meaningful. The Weizsäcker-Williams approximation, Eq. 2.13, produces a divergence at  $b = 0$ . The probability of the nuclei interacting would exceed one if the photon flux were infinite. The divergence that arises at  $b = 0$  from  $K_1$  results in an unphysically infinite photon flux. Removing the divergence is necessary. Special treatment of impact parameter,  $b$ , where the colliding nuclei overlap eliminates the divergence.

A modulation of the photon flux can subdue the divergence at  $b = 0$ . A convolution of the photon flux with the nucleon number density functions of the colliding nuclei produces the necessary modulation. Eq. 2.14 gives the nucleon density of a single nucleus,

$$\rho_A(s) = \frac{\rho_0}{1 + \exp[(s - R_{WS})/d]} \quad (2.14)$$

In Eq. 2.14,  $s$  is the distance from the center of the nucleus,  $R_{WS}$  is the radius of the nucleus, and  $d$  is the skin depth, which determines how quickly the nucleon density falls off beyond the nuclear radius. In Eq. 2.15 the depth of the nucleus is integrated out leaving just the transverse dimension in  $T_A$ . The average number of nucleons in the overlap region is given by a convolution of  $T_A$  from each of the two nuclei to produce  $T_{AA}$ .

$$\begin{aligned} T_A(\vec{r}) &= \int dz \rho_A(\sqrt{|\vec{r}|^2 + z^2}) \\ T_{AA}(|\vec{b}|) &= \int d^2\vec{r} T_A(\vec{r}) T_A(\vec{r} - \vec{b}) \end{aligned} \quad (2.15)$$

$T_{AA}$  is the function that modulates the photon flux. As input to the Poisson distribution,  $T_{AA}$  reduces Eq. 2.13 at values of  $b$  where the nuclei overlap significantly and eliminates the divergence in the photon flux.

Modulating the photon flux by the probability that no nucleon-nucleon collisions occur limits the photon flux at low  $b$  in Eq. 2.13. The convolution of the photon flux with the  $b$  dependent probability that no nucleon-nucleon collisions occur removes the divergence in Eq. 2.13. Using



the mean number of nucleons in the overlap region given by  $T_{AA}$ , the Poisson distribution gives the probability that no collisions occur at a given  $b$ :

$$P_0(b) = \exp[-T_{AA}(b)\sigma_{NN}] \quad (2.16)$$

In Eq. 2.16,  $\sigma_{NN}$  is the cross section for a nucleon-nucleon interaction, which gives the probability that a collision will occur given the average number of nucleons in the overlap region. The average photon flux over impact parameter,  $b$ , can be calculated from the integration of the  $b$ -dependent photon flux, Eq. 2.13, with the  $b$ -dependent probability of having no nucleon-nucleon interactions, Eq. 2.16.

$$\frac{dN_\gamma(k)}{dk} = \int_0^\infty 2\pi b db P_0(b) \int_0^R \frac{r dr}{\pi R_A^2} \int_0^{2\pi} d\phi \frac{d^3 N_\gamma(k, b + r \cos(\phi))}{dk d^2 r} \quad (2.17)$$

Eq. 2.17 goes down to  $b = 0$  where the photon flux is infinite, but because the probability of having a nucleon-nucleon collisions is high, the divergence is eliminated. The result of Eq. 2.17 does not diverge.

A power-law fit to the proton photoproduction data gives an analytic expression for the energy dependence of the proton photoproduction cross section. The fitting function is simple and only depends on the photon-proton center of mass energy,  $W$ . Eq. 2.18 gives the parameterization of the forward proton photoproduction cross section fit.

$$\left. \frac{d\sigma(\gamma p \rightarrow V p)}{dt} \right|_{t=0} = b_v (XW^\epsilon + YW^{-\eta}) \quad (2.18)$$

$W$  is the center of mass energy of the proton-photon system in Eq. 2.18. The remaining variables in Eq. 2.18 are simple power-law fit parameters. The  $XW^\epsilon$  term characterizes pomeron mediated interactions, and the  $YW^{-\eta}$  term characterizes meson mediated interactions[8].  $J/\psi$ 's high mass relative to the  $\pi$  and  $\rho$  renders the second term in Eq. 2.18 negligible as the term falls rapidly with increasing  $W$ . Eq. 2.18 allows for extrapolation and interpolation of the measured forward proton photoproduction cross section. The fit to the data provides estimates for energies that have not yet

been probed experimentally.

The proton-electron scattering data is used differently in the VMD method than in the other major methods. The VMD method for calculating UPC photoproduction cross sections relies more on electron-proton scattering data. The proton photoproduction cross sections from the electron-proton scattering data is a direct input to the VMD model. A power-law fit to the proton photoproduction data, as opposed to model dependent gluon densities of other approaches, combines with the Glauber model to provide the nuclear model in the VMD method. Because of the simplicity of the method, the VMD approach incorporates less modifications of the nuclear initial state relative to the proton initial state. As a result, the VMD method produces a higher UPC  $J/\psi$  photoproduction cross section relative to the other methods.

Vector meson dominance and the optical theorem allow for the calculation of the total proton-meson scattering cross section from the fit given by Eq. 2.18. The optical theorem relates a total cross section,  $\sigma$ , to a corresponding forward scattering cross section,  $d\sigma/dt|_{t=0}$ . Vector meson dominance asserts that the colored part of the photon wave function is dominated by vector mesons; therefore, the photon is represented as a quark-antiquark pair in photoproduction calculations. These two components combine to produce Eq. 2.19.

$$\begin{aligned} \frac{d\sigma(\gamma p \rightarrow Vp)}{dt} \Big|_{t=0} &= \frac{4\pi\alpha}{f_V^2(M_V, \Gamma_{l+l-})} \frac{d\sigma(Vp \rightarrow Vp)}{dt} \Big|_{t=0} \\ \sigma(Vp)_{tot}^2 &= 16\pi \frac{d\sigma(Vp \rightarrow Vp)}{dt} \Big|_{t=0} \end{aligned} \quad (2.19)$$

In Eq. 2.19, the photon-proton scattering is related to meson-proton scattering through the photon-meson coupling, which depends on the vector meson's mass,  $M_V$ , and leptonic decay width,  $\Gamma_{l+l-}$ . The result of combining vector meson dominance and the optical theorem in Eq. 2.19 provides the cross section for a meson to scatter off a proton. The total proton-meson scattering cross section, provides the input to the Glauber model calculation of the nuclear photoproduction cross section.

The nucleus-meson scattering cross section relates to Eq. 2.19 through the Glauber model. The Glauber model allows for Eq. 2.19, the proton-meson scattering cross section, to be used to

calculate a nucleus-meson scattering cross section. The Glauber model produces nuclear cross section calculations from nucleon (proton or neutron) interaction cross sections by use of  $T_{AA}$ . The combination of the mean number of nucleons in the overlapping region of a nucleus-nucleus collision,  $T_{AA}$ , the nucleon cross section,  $\sigma$ , and the Poisson distribution make-up the core of the Glauber model. For the total nucleus-meson scattering cross section, the equation has the following form:

$$\sigma_{tot}(VA) = \int d^2\vec{r} (1 - e^{-\sigma_{tot}(Vp)T_{AA}(\vec{r})}) \quad (2.20)$$

In Eq. 2.20, the term  $e^{\sigma_{tot}(Vp)T_{AA}}$  gives the probability of having no meson-nucleon scatterings from the Poisson distribution. The probability of having at least one scattering is given by subtracting one from the term  $e^{\sigma_{tot}(Vp)T_{AA}}$  in Eq. 2.20. As seen in Eq. 2.20, the Glauber model leverages scientific knowledge of the proton to understand of the nucleus. The Glauber model is the tool that combines the proton photoproduction data with nucleon distributions in the nucleus to produce a nuclear vector meson photoproduction cross section in the VMD approach.

Reversing the process used for the proton, Eq. 2.20, the meson nucleus scattering cross section, relates to forward nuclear photoproduction cross section through the optical theorem. The nuclear photoproduction cross section is the input to the calculation of the final result, the nuclear vector meson photoproduction cross section in UPC events. Eq. 2.21 uses the optical theorem to produce the nuclear photoproduction cross section from the nucleus-meson scattering cross section:

$$\sigma(\gamma A \rightarrow VA) = \frac{d\sigma(\gamma A \rightarrow VA)}{dt} \Big|_{t=0} \int_{t_{min}}^{\infty} dt |F(t)|^2 = \frac{\alpha \sigma_{tot}^2(VA)}{4\pi f_v^2} \quad (2.21)$$

$F$  in equation Eq. 2.21 is the Fourier transform of the nuclear density function,  $\rho_A$ . To produce the formula for calculating the UPC vector meson photoproduction cross section, Eq. 2.21 is combined with the photon flux incident on the nucleus, Eq. 2.17.

$$\sigma(AA \rightarrow AAV) = 2 \int dk \frac{dN_\gamma}{dk} \sigma(\gamma A \rightarrow VA) \quad (2.22)$$

The factor of 2 in Eq. 2.22 comes from the fact that both of the two colliding nuclei contribute. Combining the three elements of VMD, Eq. 2.22 is the final result of the VMD UPC photoproduction cross section calculation. Vector meson production rates in UPC collisions are predicted by Eq. 2.22, which can be confirmed or denied by experiment.

## 2.6 Leading Twist Approach Derivation

The LTA method for calculating UPC photoproduction cross sections combines elements of the Glauber model with direct use of gluon densities. The proton gluon density is modified by a nuclear modification function in the LTA method to produce the nuclear gluon density. The nuclear modification function converts the proton photoproduction cross section to a nuclear photoproduction cross section in the LTA method. The LTA method is different from the other methods in its direct use of the nuclear modification factor and how the nuclear modification factor calculation incorporates multiple scattering. The direct use of the nuclear modification factor produces the most gluon shadowing out of the three major methods, and results in the lowest cross sections. The LTA method is the easiest to constrain experimentally for this reason.

The LTA method uses the Weizsäcker-Williams approximation to calculate the photon flux created by the colliding nuclei. As in the VMD method, the probability of having no hadronic collisions modulates the flux. The photon flux for the LTA method has the following form [9]:

$$n_{\gamma/A}^i(\omega_\gamma) = \frac{2\alpha Z^2}{\pi} \int_{b_{min}}^{\infty} db \frac{x^2}{b} \left[ K_1^2(x) + \frac{K_0^2(x)}{\gamma_L^2} \right] P_0(b) P_C^i(b) \quad (2.23)$$

$$x = \frac{\omega b}{\gamma_L v}$$

The  $K_0^2(x)$  term contributes a photon flux in the transverse direction.  $P_C^i(b)$  is an additional modulation factor that requires various additional interactions. These interactions result in additional emissions of neutrons from the receding nuclei as the nuclei relax from excited states. The LTA flux reproduces the VMD result when the  $K_0$  term becomes negligible as  $\gamma_L$  approaches  $\infty$  and

$P_C^i = 1$  when all emissions are allowed. The terms  $P_C^i$  and  $K_0$  create additional ways to distinguish UPC events from nuclear collisions experimentally but leave the underlying interaction mechanism the same. For example, the additional terms in the LTA formulation of the photon flux produce calculations of asymmetric neutron emission, which separate UPC events from nuclear collisions.

The LTA method calculates the nucleon photoproduction cross section from the nucleon gluon density. Ref. [9] derives the nucleon cross section from derivations of the nucleon gluon densities from electron-proton scattering data and leading order perturbative quantum field theory calculations. The forward photoproduction cross section of the nucleon has the following form [9]:

$$\frac{d\sigma_{\gamma N \rightarrow J/\psi N}(t=0)}{dt} = \frac{16\Gamma_{l+l-}\pi^3}{3\alpha M_{J/\psi}^5} [\alpha_s \mu^2 x G_N(x, \mu^2)]^2 \quad (2.24)$$

Here  $G_N$  is the gluon density of the nucleon,  $x$  is the fraction of the nucleon's momentum the gluon carries, and  $\mu$  is related to momentum at which the nucleon is being probed, which is equal to  $M_{J/\psi}/2$  for  $J/\psi$  photoproduction. In Eq. 2.24 the nucleon cross section is explicitly connected to the gluon density. By connecting the gluon density to the cross section, Eq. 2.24 allows for the gluon density to be experimentally probed.

Ref. [9] exploits the optical theorem to relate the forward photoproduction cross section of the nucleon to the nuclear cross section. Eq. 2.25 gives the relation:

$$\sigma_{\gamma A \rightarrow J/\psi A}(\omega) = \frac{d\sigma_{\gamma N \rightarrow J/\psi N}}{dt}(\omega, t_{min}) R_g^2 \int_{t_{min}}^{\infty} dt |F(t)|^2 \quad (2.25)$$

$$R_g = \frac{G_A(x, \mu^2)}{AG_N(x, \mu^2)}$$

$R_g$ , the nuclear modification function, is the ratio between the gluon density of the nucleon,  $G_N$ , to the gluon density of the nucleus,  $G_A$ . As with the VMD method, the optical theorem relates the forward cross section,  $\frac{d\sigma_{\gamma N \rightarrow J/\psi N}}{dt}(\omega, t_{min})$ , to the total cross section,  $\sigma_{\gamma A \rightarrow J/\psi A}$ . The LTA method relates the measurable UPC photoproduction cross section to the gluon density of the nucleus. Eq. 2.25 further connects the gluon density of the nucleon to the relative reduction of the gluon

density in the nucleus through  $R_g$ .

From Eq. 2.25, the LTA method can predict the angular distribution of photoproduced  $J/\psi$  with respect to the beam axis. In Ref. [10] the angular distribution is expressed in the form of the rapidity dependency of the UPC photoproduction cross section.

$$\frac{d\sigma_{A_1 A_2 \rightarrow A_1 A_2 J/\psi}}{dy} = n_{\gamma/A_1}(y) \sigma_{\gamma A_2 \rightarrow J/\psi A_2}(y) + n_{\gamma/A_2}(-y) \sigma_{\gamma A_1 \rightarrow J/\psi A_1}(-y) \quad (2.26)$$

$$y = \ln\left(\frac{2\omega}{M_{J/\psi}}\right)$$

Eq. 2.26 is comprised of two terms, one for photons from the forward going nucleus interacting with the backward going nucleus, and a second for the reverse situation. The integration of Eq. 2.26 over  $y$  produces the factor of 2 that is present in Eq. 2.22. The rapidity distribution of the photoproduction cross section given in Eq. 2.26 provides a more detailed prediction and allows for more direct experimental comparison. Eq. 2.26 allows for comparison to rapidity regions that are covered by experiments.

The LTA method is distinct from the pQCD method and VMD method through the use  $R_g$ , the nuclear gluon modification factor. As opposed to using  $R_g$ , the pQCD method uses the nuclear gluon density, and VMD model uses proton photoproduction cross sections directly. In the LTA method,  $R_g$  is calculated through a combination of  $J/\psi$  photoproduction data from proton-electron scattering and DGLAP evolution equations, which incorporates nuclear multiple scattering effects [9]. The DGLAP evolution equations give the depends of nuclear gluon densities on the momentum scale at which the nucleus is probed,  $\mu$  in Eq. 2.24. The unique way the LTA method calculates  $R_g$  results in lower cross sections than the other major methods and allows for experimental sensitivity. Experimental measurements of the UPC  $J/\psi$  photoproduction cross section with CMS have the opportunity to distinguish whether  $R_g$  as calculated in the LTA method accurately predicts the gluon density of the nucleus.

## 2.7 Perturbative Quantum Chromo-dynamics

To calculate the UPC  $J/\psi$  photoproduction cross section, the pQCD method uses the nuclear gluon density to characterize the nucleus and the Weizsäcker-Williams approximation for the probing photon flux. The pQCD method combines these components such that the nuclear gluon density is a direct variable. The nuclear gluon density term in the pQCD formulation allows for the use of a variety of nuclear gluon density models. A range of nuclear gluon densities are present in the available models resulting in a wide range of cross section values. The UPC  $J/\psi$  photoproduction cross section is correlated with the gluon density of the nucleus rising with higher densities and shrinking with lower densities. In the pQCD approach, the calculation of the UPC  $J/\psi$  photoproduction cross section allows experiments to constrain many different nuclear gluon density models.

In the pQCD method, the photon interacts with the nucleus by fluctuating to a quark-antiquark pair. For  $J/\psi$ , the photon fluctuates to a  $c\bar{c}$  pair. The probability for the photon to fluctuate to a  $c\bar{c}$  pair depends on the  $M_{J/\psi}$ , the mass of  $J/\psi$ ,  $\Gamma_{l+l^-}$ , the  $J/\psi$  leptonic decay width, and  $\alpha$ , the electromagnetic coupling constant. These three variables connect the  $c$  quark to the electromagnetic force mediator, the photon. Recast as a  $c\bar{c}$  pair, the photon couples to the nuclear gluon density. Ref. [11] uses the fluctuation of the photon to a  $c\bar{c}$  pair as the foundation for calculating the forward  $J/\psi$  photoproduction cross section.

The  $c\bar{c}$  pair arising from the photon fluctuation scatters off the gluons of the nucleus. The density of gluons in the nucleus determines how likely and therefore how large the cross section is for the quarks to scatter and form a  $J/\psi$ . The forward scattering cross section is the portion of those scattering events which transfer the minimum amount of momentum between the photon and the nucleus. The forward cross section for  $J/\psi$  photoproduction in the nucleus has the following form [11]:

$$\left. \frac{d\sigma_{\gamma A \rightarrow J/\psi A}}{dt} \right|_{t=0} = \xi_{J/\psi} \left( \frac{16\pi^3 \alpha_s^2 \Gamma_{l+l^-}}{3\alpha M_{J/\psi}^5} \right) [xG_A(x, \mu^2)]^2 \quad (2.27)$$

In Eq. 2.27,  $\xi_{J/\psi}$  is an experimentally derived correction factor,  $\alpha_s$  is the strong coupling constant,

$x$  is the momentum fraction of the nucleus the scattering gluons carry, and  $G_A$  is the gluon density of the nucleus. Both the  $c$  and  $\bar{c}$  couple to the gluon density, and the double coupling results in the squared dependence of the cross section on the gluon density in Eq. 2.27. Fitting Eq. 2.27 to proton-electron scattering data sets  $\xi_{J/\psi}$  [11]. The forward scattering cross section given by Eq. 2.27 connects the photon flux to the gluon density and provides the input to calculate the total cross section by the optical theorem. Eq. 2.27 is the crux of how UPC measurements provide insight into the gluon content of the nucleus.

The optical theorem relates the forward cross section in Eq. 2.27 to the total photoproduction cross section. The total cross section calculated by use of the optical theorem gives the probability that a photon incident on the nucleus will produce a  $J/\psi$  regardless of the momentum transferred in the interaction. Ref. [11] gives the form of the total cross section equation:

$$\sigma_{\gamma A \rightarrow J/\psi A}(k) = \frac{d\sigma_{\gamma A \rightarrow J/\psi A}}{dt} \Big|_{t=0} \int_{t_{min}(k)}^{\infty} dt |F(t)|^2 \quad (2.28)$$

Here  $t_{min} = (M_{J/\psi}^2/4k\gamma_L)^2$ , which is the minimum amount of momentum transfer required to produce a  $J/\psi$  given the photon wave number  $k$ . The  $k$  dependence of  $t_{min}$  produces the rapidity,  $y$ , dependence of the total cross section. The total cross section for photoproduction, Eq. 2.28, provides the input to Eq. 2.26, which gives the rapidity dependence of the UPC photoproduction cross section. Eq. 2.28 as input to Eq. 2.26 allows for experimental comparison of the pQCD method to measurements of UPC photoproduction cross sections. With the pQCD method's direct use of the nuclear gluon density in Eq. 2.27, the pQCD method allows for experimental exploration of any gluon density model.



## 2.8 Incoherent Photoproduction

## 2.9 Photon Induced Nuclear Break-up

Two different approaches are discussed. The first is to measure the desired cross-section directly. This can be done by bombarding the target material with mono-energetic real photons, varying the energies of the photons over a range of frequencies, and extrapolating that data up to the photon energies that arise in the Weizäcker-Williams approximation [3]. The other approach is to create a theoretical model of how the target reacts to a photon flux [4]. In the theoretical model that will be discussed in this paper, the photonuclear cross-section, the cross-section governing the absorption of photons by a nucleus, is formulated as the sum of two other cross-sections that are known better. In both, the more detailed theoretical approach and the empirical approach to the problem, the interaction of the Weizäcker-Williams quasi-real photons is assumed to be identical to the interaction of real photons with the target.

To model the interaction of the photons with the target nuclei, as done in Ref. [4], the photonuclear cross-section is broken down into two parts.

(16) The Giant Dipole Resonance (GDR) cross-section dominates at lower photon frequencies and is the result of the collective motion of the protons relative to the neutrons. The Quasi-Deuteron (QD) cross-section dominates at higher photon energies and is the result of treating the nucleus as a collection of proton-neutron pairs, which is deuterium.

The giant dipole resonance has been studied for decades. In 1947, Baldwin and Klaiber first observed the giant dipole resonance [6]. At the General Electric Research Laboratory, Baldwin and Klaiber found that by bombarding a uranium target with photons in the range 10 – 100 MeV, a peak in the spectrum was found for photons at 20 MeV. A year later, Goldhaber and Teller theorized that this was the result of the protons moving back and forth with respect to the neutrons [6]. In this model, the protons and neutrons are treated as two separate liquid dots. Then in 1950, Steinwedel and Jensen modified this theory by modeling the protons and neutrons as fluids contained in a single sphere rather than two separate dots moving back and forth [6].

In order to understand the Goldhaber and Teller model, it is useful to consider a nucleus where the number of protons and neutrons are equal,  $Z=A/2$ . The collection of protons and the collection of neutrons move opposite each other and only in the  $z$  direction. In order to construct a Hamiltonian, first the kinetic energy should be considered.

(17) Eq. 17 is the familiar equation for kinetic energy simply summed over all the constituent nucleons of the nucleus. The protons and neutrons are modeled as separate liquid drops with densities  $\rho_p$  and  $\rho_n$ . These liquid dots will oscillate back and forth in opposite phase relative to the center of mass maintaining their individual density profiles.

The potential holding protons and neutrons together depends on the difference of the two densities squared. If the two exactly overlap, there is no difference in the densities and the potential energy is zero. If the two density distributions are separated, there will be regions where the neutron density is greater and regions where the proton density is greater. In the separated configuration, there will be potential energy. The potential energy can be shown to have the form of a harmonic oscillator with a spring constant that depends on the initial density distribution [6].

(18) If the nucleus has a shape cut off in density at its very edge, then the integral is dominated by the region at the surface, and the spring constant  $K$  becomes proportional to the mass number to the 2/3rds power,  $A^{2/3}$ . This is the consequence of the geometry of a sphere. The surface area of a sphere is proportional to its volume to the 2/3rds power. Recalling the angular frequency of a harmonic oscillator, (19) it is seen that the frequency of the giant dipole resonance in the Goldhaber and Teller model is proportional to the mass number to the negative 1/6th power,  $A^{-1/6}$ . This dependence describes light nuclei well, but it does not describe heavier nuclei [6].

In order to describe heavier nuclei, the Steinwedel and Jensen model must be used. In the Steinwedel and Jensen model, the proton and neutron fluids are confined to a single sphere where they are allowed to slosh back and forth creating the same effect as the Goldhaber and Teller model. In this model, there is no global separation of the proton and neutron fluids. The dipole is created by underdensities and overdensities of the proton and neutron fluids. It can be shown that this results in a frequency of oscillation which depends on one over the radius of the nucleus [6]: (20)

As before, the relationship in Eq. 20 arises from the geometry of a sphere. The dependence of the giant dipole resonance that is seen in the Steinwedel and Jensen describes medium and heavier mass nuclei well. Empirically, both models are stitched together to give the following mass number dependence of the peak dipole resonance [6].

(21) In order to compute the effect of an excitation in either model, the harmonic oscillator solutions found earlier can be driven by an interacting force. The resulting differential equation can then be solved using a Fourier transform to eliminate the time derivatives and reduce the equation to an algebraic equation. Following this procedure produces the shape of energy dependence of the giant dipole resonance, and this gives a cross-section for photon absorption by the giant dipole resonance with Lorentzian form [6]: (22) here  $\sigma_{\max}$  is the maximum cross-section, when  $E\gamma = E_{\text{GDR}}$ ,  $E_{\text{GDR}}$  is the peak resonance energy, and  $\Gamma_{\text{GDR}}$  is the width of the resonance. The width,  $\Gamma_{\text{GDR}}$ , of this distribution lies in a range from 4-8 MeV and depends on the orbital arrangement to the neutrons and protons in the given nucleus [6].

For higher energy photons, the quasi-deuterium cross-section is needed. The quasi-deuterium approach amounts to treating the nucleus as a bunch of proton-neutron pairs, which are screened by the rest of the nucleus. Eq. 23 models this behavior [4].

(23) Here  $\sigma_d$  is the deuterium disintegration cross-section for  $\gamma + d \rightarrow p + n$ .  $F$  is a function that arising from Pauli blocking of fermions, and  $L$  is an empirical parameter set by data that is equal to 6.5. Certain energy levels are not available to the products of the deuterium disintegration process because of the presence of the rest of the nucleus. The result is a reduction of the cross-section.

$F$  can be modeled with an exponential cutoff below 20 MeV, a polynomial in the intermediate range with nearly linear dependence on  $E\gamma$ , and above 140 MeV an inverted exponential pushing  $F$  to one at higher values of  $E\gamma$  [4]. Essentially, the model at low photon energies disallows deuterium disintegration because the products have no available state to occupy, and at high energies the rest of the nucleus becomes transparent and looks more and more like a collection of deuterium. The deuterium disintegration cross-section is found empirically and is fit to the following function [4]: (24) In order to produce a final state for the target nucleus, a branching ratio is

needed. The branching ratio gives the probability that the photo-excited nucleus will end up in a particular state. This determines the sort of emission that will result from the de-excitation process. There are two phases of deexcitation, the nonequilibrium phase and the equilibrium phase. In the time before reaching equilibrium, fast nucleons are emitted. Subsequently, in the equilibrium phase, slow nucleons evaporate. These two phases are simulated in complex computer codes that calculate branching ratios (see discussion in Ref. [4]).

All the tools are now assembled to calculate the cross-section for any particular electromagnetic dissociation process. The first step in the calculation is to assume that the number of photons absorbed by either nucleus in the collision obeys the Poisson distribution [3,4]. An average number of absorptions is calculated and used in the construction of the distribution.

(25) When using the model of Ref. [4], the cross-section involved in Eq. 25 will be the photonuclear cross-section, and the calculation will produce the average number of photons absorbed by the target. If instead the empirically measured photoneutron cross-section is used as in Ref. [3], the mean calculated in Eq. 25 will be the number of photons absorbed that result in neutron emission from the target. This restricts the calculation to only de-excitation modes that produce neutrons. Both averages are for a given impact parameter  $b$ .

Following Ref. [3] and using the experimentally measured photoneutron cross-section, the probability  $P_n$  for the target to produce a number of neutrons,  $k$ , due to the photon flux of the projectile can be calculated using Eq. 26.

(26) This is just the Poisson distribution. In the collider situation, where both nuclei can be treated as the target and the projectile, the probability of mutual emission, one nucleus emitting  $x$  neutrons and the other emitting  $y$  neutrons, can be calculated from Eq 27.

(27) It is also interesting to consider the situation where at least one neutron is emitted. This can be calculated by subtracting the probability of no neutrons being emitted from one.

When using the model of Ref. [4], a branching ratio is needed to calculate the probability of de-exciting into a given state. The probability of photon absorption is calculated as in Eq. 26, only using the model of Ref. [4]. This is the probability of the target absorbing  $k$  photons rather than

then the nucleus absorbing a photon and emitting a neutron. In Ref. [4], the probability of any final state  $i$  due to the absorption of a single photon can be calculated using Eq. 28.

(28) Here  $P_a$  is the probability that the target absorbs a single photon as calculated by Eq. 26,  $q$  is the probability that the photon will have the frequency  $\omega$ , and  $f_i$  is the branching ratio. The following equation describes  $q$  [5].

(29) By multiplying Eq. 26 and 29 in Eq. 28, the  $m(b)$  terms cancel and produce a simplified equation. The forms for probability functions, like Eq. 28, that involve absorption of multiple photons have additional terms. But they follow that same scheme of multiplying the probability of absorption times the probability that the absorbed photon has a particular frequency times the branching ratio.

The probability functions Eq. 26 and Eq. 28 can then be used to produce cross-sections. For any given process, using Eq. 28 can be used by inserting the appropriate branching ratio. For emission of neutrons, Eq. 26 can be used. This is done by integrating over the impact parameter to get an area that is weighted by the probability functions [3,4].

(30) If the branching ratio for neutron emission is selected in Eq. 28, then Eq. 28 and Eq. 26 can be used to compute the same cross-section through the use of Eq. 30.

Three parameters arise when calculating the cross-section in Eq. 30, the minimum impact parameter  $b_0$ , the minimum emitted photon frequency  $\omega_{\min}$ , and the maximum emitted photon frequency  $\omega_{\max}$ . The need for a minimum impact parameter is necessitated by the Bessel function in the photon flux in Eq. 14. At zero, the modified Bessel function does not converge. Physically, a minimum impact parameter is selected in order to separate the domains between electromagnetic interactions and the strong interactions that happen inside the nucleus. To serve this end, the minimum impact parameter is set to the radius of the nuclei [3,4]. This excludes collisions where the nuclei overlap in the calculation, and assures only electromagnetic interactions are involved.

Model	$\sigma_{AA \rightarrow AAJ/\psi}(mb)$
VMD/STARlight MC	23
LTA	9
pQCD-MSTW08	34
pQCD-EPS08	7
pQCD-EPS09	14
pQCD-HKN07	23

Table 2.1:  $\sigma_{AA \rightarrow AAJ/\psi}(mb)$  the LTA, VMD, pQCD methods. Four different gluon density models are used in the pQCD method. STARlight is a simulation software package that utilizes the VMD model.

## 2.10 Theoretical Results

The UPC photoproduction cross section calculations depend significantly on how the nucleus is represented in the calculation. The results from the VMD, LTA, and pQCD methods vary from a relatively large cross section in the VMD model, ranging through a variety of values in the pQCD method, to a relatively small cross section in the LTA method. Each of these methods utilizes the same probe of the nucleus, the equivalent photon flux that is calculated using the Weizsäcker-Williams approximation. The three methods deviate in how they calculate the forward photoproduction scattering cross section. The differences in the UPC photoproduction cross sections predicted by the different models demonstrates the amount of experimental sensitivity there is to distinguishing between the models. The dependence of the cross section on rapidity shows where in phase space a measurement of the cross section is most sensitive.

The predicted value for the UPC  $J/\psi$  photoproduction cross section in PbPb collisions at the LHC differ widely depending on which of the three main methods is used. The cross section value calculated by Eq. 2.22 in the VMD, LTA, and the various gluon density models in pQCD method vary significantly. Table 2.1 gives the predicted values for the three main methods taken from Ref [12], Ref [9], and Ref [8]. The cross sections in Table 2.1 differ by a factor of  $\approx 4$  from the smallest to largest and create an experimental opportunity. The clear discrepancy between the models in Table 2.1 demonstrates the high amount of experimental sensitivity there is for distinguishing between the models.

The rapidity dependence of the cross sections determine which values of rapidity will be most sensitive to differences in the models. The rapidity dependence calculated by Eq. 2.26 overlap between the models at certain values of  $y$  leaving the models indistinguishable at that rapidity. Fig. 2.4 [13] shows the rapidity dependency of the UPC  $J/\psi$  photoproduction cross section for the three main models including several different gluon density models using the pQCD method. In

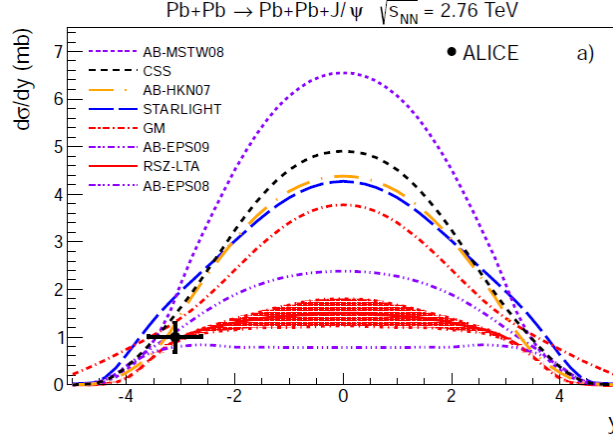


Figure 2.4: AB is the pQCD method, RSZ-LTA is the LTA method, and STARlight is the VMD model.

Fig. 2.4 at higher rapidities, in particular  $|y| > 3$ , the various models give similar values for  $d\sigma/dy$ . At  $y = 0$  the models vary the most. Fig. 2.4 shows that experiments that can measure  $J/\psi$  at  $y = 0$  have the best opportunity to distinguish between the models. The high sensitivity at  $y = 0$  creates an advantage for experiments that can measure particles with small rapidity and low momentum.

The UPC photoproduction models each have different shapes to their rapidity dependence. The slope of  $d\sigma/dy$  in Fig. 2.4 depends on the model. Through the rapidity region  $1 < |y| < 3$ , each of the models has a progressively steeper slope. The LTA method and the pQCD method utilizing the EPS08 gluon density model are relatively flat where as the VMD and other gluon density models using the pQCD method have a noticeable slope. The differing slopes provide an additional experimental observable. The shape of the rapidity distributions provide experimental sensitivity at rapidities away from  $y = 0$  and creates an opportunity for experiments that can not measure  $J/\psi$  at  $y = 0$ .

The nuclear suppression factor,  $S$ , demonstrates the difference between how the models represent the nucleus.  $S$ , which is a ratio between the nuclear photoproduction cross section and the free nucleon photoproduction cross section, is a measure of how the nuclear gluon densities evolve in each of the models. Fig. 2.5 from Ref.[14] shows the nuclear suppression, which is equivalent to  $R_g$  in Eq. 2.25, for the LTA and pQCD method. Fig. 2.6 shows the nuclear suppression for

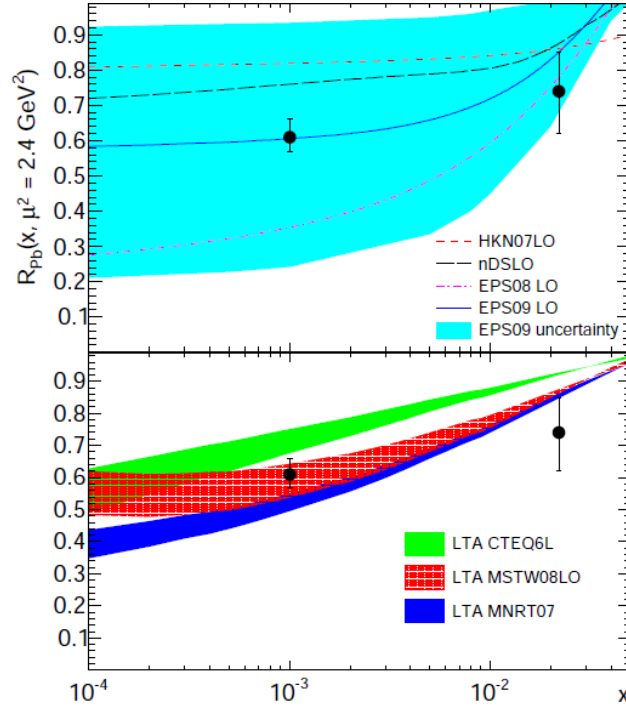


Figure 2.5: Nuclear suppression factor,  $S$ , in the pQCD and LTA methods.

the VMD method [14]. Fig. 2.6 and Fig. 2.5 show that as the momentum of the probing photon goes up, increasing  $W_{\gamma p}$ , and momentum of the probed gluon goes down, decreasing  $x$ , the nuclear gluon density decreases relative to the free nucleon. The nuclear suppression factor,  $S$ , allows for the different models' representations of the gluon content of the nucleus to be directly compared to each other and to data.  $S$  can be measured from data by assuming a Weizsäcker-Williams photon flux and provides insight into nuclear gluon densities.



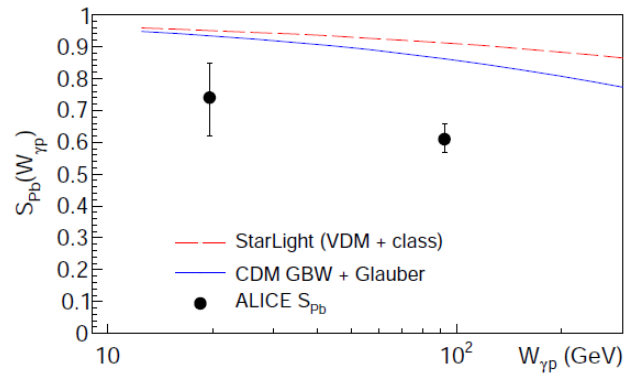


Figure 2.6: Nuclear suppression factor,  $S$ , in VMD method.

# Chapter 3

## The CMS Detector

CMS is housed at interaction point 5 of the LHC. The LHC is designed to pursue physics at the TeV scale. This is the scale where electroweak symmetry breaking is believed to occur [?]. While this means that the search for the standard model Higgs is the central driving design consideration, the wide range of possibilities for finding new physics signals requires a general purpose detector. The expedient discovery of new physics through low cross section interactions requires high luminosity. This consideration leads inevitably to pile up, where multiple collisions occurs at a single bunch crossing. At peak luminosity the LHC is expected to produce on average 20 hard proton-proton (pp) collisions per bunch crossing [2]. These particle physics considerations of high multiplicity due to pileup and the need for a general purpose detector make CMS serendipitously well suited for heavy ion physics.

The general purpose design of CMS is dominated by the massive 4T superconducting solenoid at its core. The magnets is 13m long with a 6m diameter, and pushes the limits of power and compactness [2]. These two conflicting limits are achieved through the novel design of interweaving structural and conducting elements together in the coil of the solenoid.

Within the solenoid resides three different sub detectors. The inner most is the world's largest silicon tracker [2]. The tracker is surrounded by a highly effective lead tungstate crystal electromagnetic calorimeter (ECAL). ECAL is encapsulated in a brass scintillating hadronic calorimeter

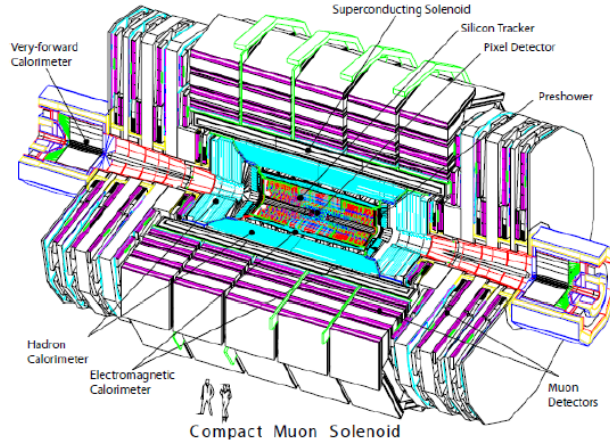


Figure 3.1: The Compact Muon Solenoid from Reference [2].

(HCAL). Outside the magnet, muon chambers are used to aid in the measurement and triggering of muon events. Altogether CMS weighs 12,500 metric tons, has a diameter of 14.6m, and a length of 21.6m [2].

### 3.1 Tracker

The Silicon Tracker is the innermost sub-detector of CMS, and has active elements as close as 4.4cm to the interaction point [2]. The tracker has a length 5.8m, a diameter of 2.6m and covers a range in pseudorapidity of  $|\eta| < 2.5$ . Pseudorapidity is defined as  $\eta \equiv -\ln(\tan(\theta/2))$ , where  $\theta$  is the polar angle, and  $\phi$  is the azimuthal angle with respect to the beam axis. At the center of the tracker are three rings of silicon pixels around the beam with two disks of silicon pixels to cap the rings. The pixel portion of the silicon tracker is comprised of  $66 \times 10^6$  pixels. The silicon pixels are surrounded by silicon strips. The silicon strips are separated into 4 different sections: the Tracker Inner Barrel, the Tracker Inner Disk, the Tracker Outer Barrel, and the Tracker End Caps. The silicon strip detectors as a whole are comprised of  $9.3 \times 10^6$  silicon strips. The high number of pixels and strips allow for the ability to distinguish and collect enough distinct points to reconstruct the path of the 1000 or so charge particles per bunch crossing expected at peak luminosity [2].

## 3.2 ECAL

The next detector beyond the tracker is ECAL. ECAL is made of 61,200 lead tungstate ( $\text{PbWO}_4$ ) crystals in the central barrel and 7,324 on each of the two endcaps [2]. The barrel (EB) covers a pseudorapidity range  $|\eta| < 1.479$  and has an approximate  $\eta - \phi$  segmentation of  $0.0174 \times 0.0174$ . Lead tungstate is very dense, which is reflected in the high number of interaction lengths the short depth of one crystal provides. The crystals of the barrel have a depth of 230 mm corresponding to 25.8 radiation lengths ( $X_0$ ). The radiation length is the mean distance a high energy particle travels before giving up one e-fold of kinetic energy through electromagnetic interactions. For example, after one radiation length  $E \rightarrow E/e$ , where  $e = 2.71828183$ . The endcaps (EE) cover the pseudorapidity region  $1.479 < |\eta| < 3$ . In the endcap the crystals have an exposed area of  $28.62 \times 28.62 \text{ mm}^2$ , and a depth of 220 mm corresponding to  $24.7 X_0$ . The energy resolution of the ECAL as measured by test beam data can be seen in Figure 3.2.

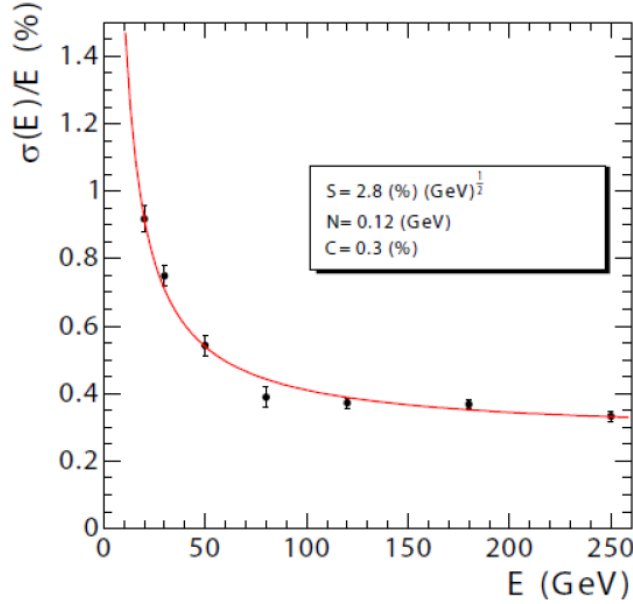


Figure 3.2: The energy resolution of ECAL as a function of energy from Reference [2].

### 3.3 HCAL

The HCAL like the ECAL has both a barrel (HB) and endcaps (HE). The pseudorapidity region  $|\eta| < 1.3$  is covered by HB [2]. HB has an  $\eta - \phi$  segmentation of  $0.0897 \times 0.0897$ , and is 25 times more sparsely granulated than EB. HE covers the pseudorapidity region  $1.3 < |\eta| < 3$ . HE, like EE and the tracker endcaps, is aligned perpendicular to the beam axis resulting in granularity that changes with  $\eta$ . In the region  $1.3 < |\eta| < 1.6$  HE has an  $\eta - \phi$  segmentation of  $0.0897 \times 0.0897$ . The  $\eta - \phi$  segmentation roughly doubles to  $0.17 \times 0.17$  in the region  $1.6 < |\eta| < 3$ . The energy resolution of the barrel and endcaps can be seen in Figure 3.3. The thickness of the hadronic calorimeter is best described in interaction lengths, the mean distance for a particle to give up an e-fold of energy through nuclear interactions. At  $\eta = 0$  the barrel has a thickness 5.82 interaction lengths ( $\lambda_I$ ), and increases as the path length through the material increases to  $10.6 \lambda_I$  at  $|\eta| = 1.3$ .

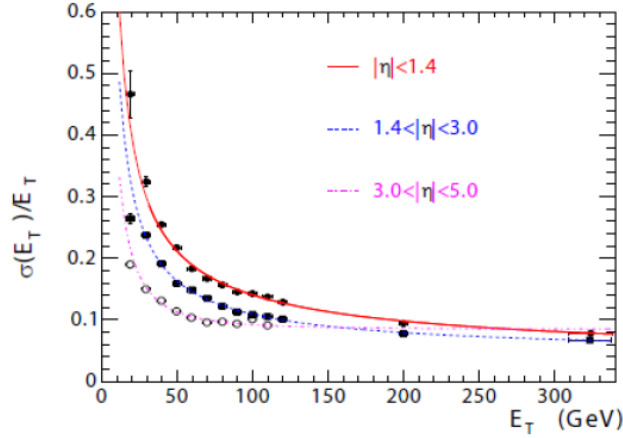


Figure 3.3: The  $E_T$  resolution of HCAL as a function of  $|\eta|$  and  $E_T$  from Reference [2].

In addition to HB and HE, HCAL has two additional calorimeters. Because the space between ECAL and the magnet is restricted to 1.18 m, an outer hadronic calorimeter section (HO) is placed beyond the magnet in the region  $|\eta| < 1.3$  [2]. The main function of HO is to collect energy from the highest energy hadrons before they reach the muon system. HO is not used in this analysis, but does contribute to the material budget. To increase the total calorimetric coverage, HCAL also has a quartz fiber calorimeter (HF) in the forward region,  $3 < |\eta| < 5$ . For the majority of HF's

13  $\eta$  rings the  $\eta - \phi$  segmentation is  $0.175 \times 0.175$ . In the lowest  $|\eta|$  ring the segmentation is  $0.111 \times 0.175$  in  $\eta - \phi$ . In the highest two  $|\eta|$  rings the segmentation in  $\phi$  is 0.349, with an  $\eta$  segmentation of 0.175 in the outer and 0.300 in the innermost ring. The longitudinal direction is effectively segmented by using short fibers and long fibers. The measure energy deposited deeper than 22 cm is measured in both the short and long fibers, where as the long fibers are present throughout. This allows electromagnetic showers to be distinguished from purely hadronic showers [2]. The energy resolution for HF can be seen in Figure 3.3.

### 3.4 ZDC

Beyond HF, the Zero Degree Calorimeters(ZDC) covers the very forward rapidity region. ZDC sit between the beam pipes on either side of the interaction point covering the area around  $\theta = 0$ ,  $|\eta| > 8.3$ . In heavy ion collisions the ZDC has the ability to measure neutral particles that do not participate in the collision [2].

The ZDC has a total of 18 channels. Half of these 18 channels are on either side of the interaction point. The 9 channels on the side of CMS that correspond to positive  $\eta$  are denoted  $ZDC^+$ , where as the 9 channels on the negative side are denoted  $ZDC^-$ . The 9 channels on each side are further sub-divided into an electro-magnetic (EM) section and a hadronic (HAD) section. The EM section is positioned in front of the HAD section with respect to the interaction point and is segmented transverse to the beam direction. The 5 EM sections are positioned in front to absorb the energy from electro-magnetically induced showers, which develop over a shorter distance than hadronically induced showers. The transverse segmentation allows for a measurement of the transverse shower width and the size of the beam spot at the ZDC. The HAD section is segmented in the direction of the beam and consists of 4 channels. The longitudinal segmentation allows for absorption of the full extended hadronic shower and the ability to measure the longitudinal shower shape.

Each the 18 channels contains a tungsten target and quartz fibers. The dense tungsten target

is used to initiate the shower. The quartz fibers shine Cerenkov light as the high momentum charged particles from the shower pass through it. The light from the quartz fibers is channeled to photo-multiplier tubes, one for each ZDC channel. Through a cascade of photon induced electrical discharges, the photo-multiplier converts the Cerenkov light to an electrical pulse.

This electrical pulse travels  $\sim 200$  m down a coaxial cable from the LHC tunnel to the counting house in the CMS service cavern. There the electrical pulse is digitized by the Charge Integrator and Encoder (QIE). The QIE integrates the current each 25 nano seconds. The charge is then mapped logarithmically to the 128 bits. This bit is sent across a small fiber optic cable to the HTR firmware card. Here each 25 ns signal is stored in a 250 ns buffer, and the timing is sync with the rest of the detector to insure the ZDC signal arrives at the central data acquisition system at the same time as the other sub detectors from the same collision.

### 3.5 Muons

The muon system resides just outside of the superconducting magnet. It consists of three complementary systems: drift tube (DT) chambers in the barrel, cathode strip chambers (CSC) in the endcaps, and resistive plate chambers (RPC) in both the barrel and endcap regions [2]. Ultimately the muon system is most useful for triggering on muons and identifying tracks as muons [2].

As seen in Fig. 3.4, the DTs reside only in the barrel, covering the region  $|\eta| < 1.2$ . Consisting of a total of 172,000 cells, the DT cells are collected into 250 chambers. The DT chambers are interwoven into the magnet field return yoke and are labeled by 5 segmentations in  $z$ , YB-2 to YB+2. Each  $z$  segment is divided into 12  $\phi$  segments labeled 1 at  $\phi = 0$  and going to 12 rotating in positive  $\phi$  with segments 4 and 10 contain 2 chambers. The segmentation in  $r$  is divided into four parts, MB1-MB4. Fig. 3.5 shows how each chamber is made of three super layers. Super layers  $SL \Phi_1$  and  $SL \Phi_2$  measure  $(r - \phi)$ , whereas  $SL \Theta$  measures  $z$ .

The RPC complement the DTs in the barrel and the CSCs in the endcap primarily for the purpose of triggering. Six layers of RPC chambers are embedded in the barrel iron yoke, two

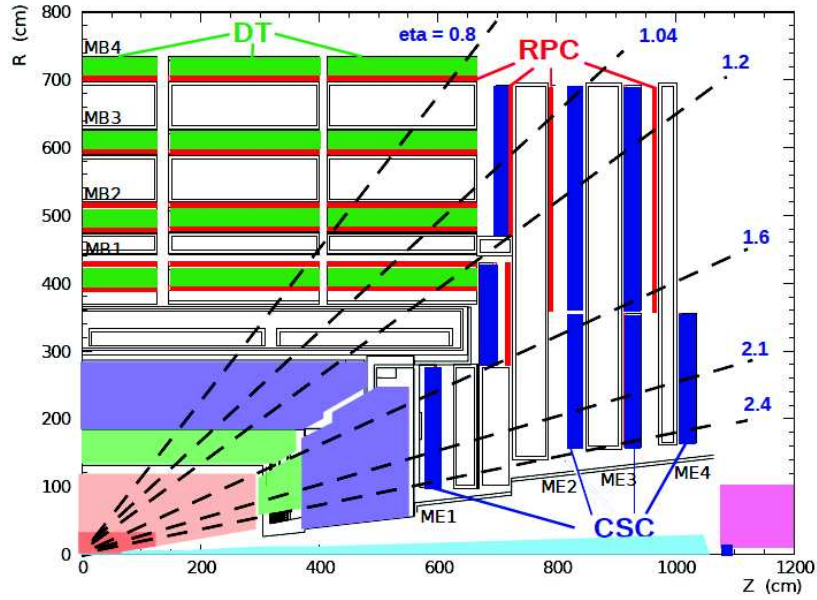


Figure 3.4: The CMS muon system showing the four DT stations in the barrel (MB1-MB4), the four CSC stations in the endcap (ME1-ME4), and the RPC stations.

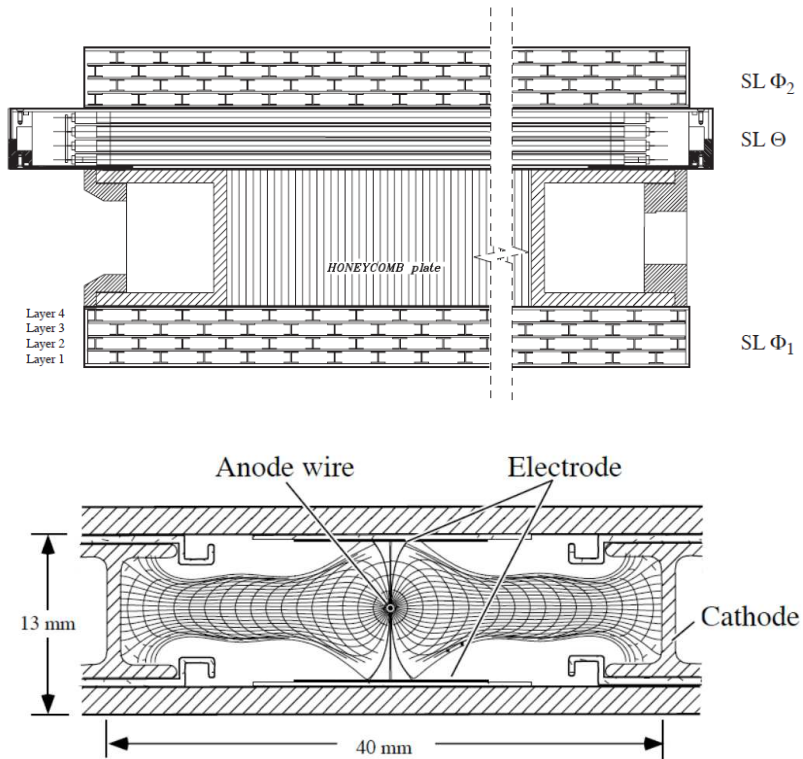


Figure 3.5: Schematic of the DT chambers and an individual DT cell.



located in each of the first and second muon stations (RB1, RB2) and one in each of the two last stations (RB3, RB4), where RB1 corresponds to  $r$  segment in the DTs MB1 and RB2 with MB2 etc. The redundancy in the first two stations allows the trigger algorithm to perform the reconstruction always on the basis of 4 layers, even for low  $p_T$  particles, which may stop inside the iron yoke. In total there are 480 rectangular chambers, each one 2455 mm long in the beam direction. The strips run along the beam direction providing position measurements in the  $(r - \phi)$  plane. In the endcap region, 3 layers of RPCs to cover the region up to  $|\eta| = 1.6$ . They are mounted on both faces of the disks. The double-gaps in every station have a trapezoidal shape and are arranged in 3 concentric rings in the  $(r - \phi)$  plane. They overlap in  $\phi$  to avoid dead space at chamber edges.

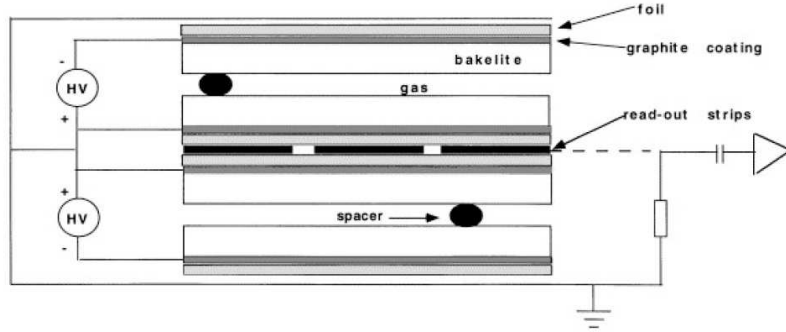


Figure 3.6: Schematic of a RPC cell.

The CMS Endcap Muon system will consist of 468 CSC arranged in groups as follows: 72 ME1/1, 72 ME1/2, 72 ME1/3, 36 ME2/1, 72 ME2/2, 36 ME3/1, 72 ME3/2, and 36 ME4/1. The chambers are trapezoidal and cover either  $10^\circ$  or  $20^\circ$  in  $\phi$ ; all chambers, except for the ME1/3, overlap and provide contiguous-coverage. A muon in the pseudorapidity range  $1.2 < |\eta| < 2.4$  crosses 3 or 4 CSCs. The CSCs are multiwire proportional chambers comprised of 6 anode wire planes interleaved among 7 cathode panels. Wires run azimuthally and define a tracks radial coordinate. Strips are on cathode panels and run lengthwise at constant  $\Delta\phi$  width. The largest chambers, ME2/2 and ME3/2, are about  $3.4 \times 1.5 \text{ m}^2$  in size. The overall area covered by the sensitive planes of all chambers is about  $5000 \text{ m}^2$ , for a gas volume more than  $50 \text{ m}^3$ , and a number of wires of about 2 million. There are about 9000 high-voltage channels in the system, about 220,000 cathode strip read-out channels with 12-bit signal digitization, and about 180,000 anode wire read-

out channels. This system will ensure at least 99% efficiency per chamber for finding track stubs by the L1 trigger and at least 92% probability per chamber of identifying correct bunch crossings by the L1 trigger. This efficiency per chamber and 3-4 CSCs on a muon track path, ensure that the reconstructed muons will be assigned the correct bunch crossing number in more than 99% of cases. The CSC system guarantees a  $(r - \phi)$  resolution at the L1 trigger of about 2 mm, that improves up to 75  $\mu\text{m}$  in off-line reconstruction for ME1/1 and ME1/2 chambers and about 150  $\mu\text{m}$  for all others.

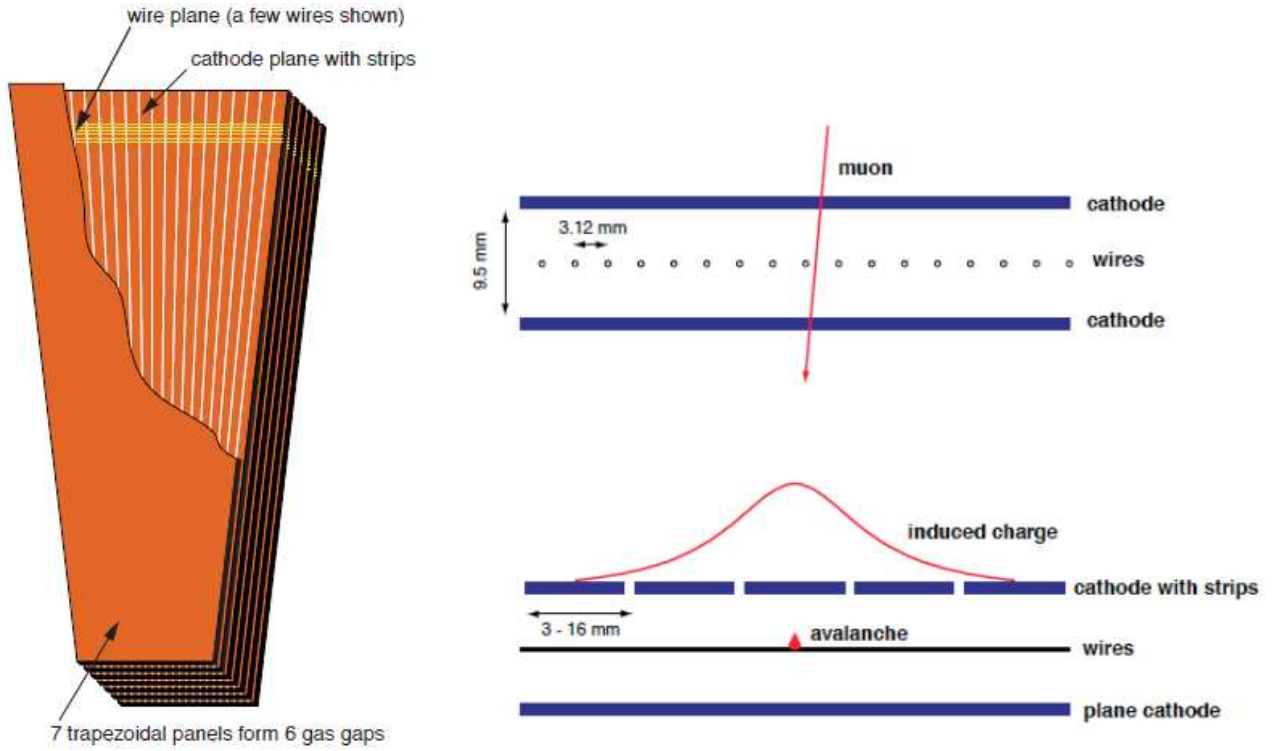


Figure 3.7: Schematic of the CSC chambers and an individual CSC cell.

The heavy ion community is making use of the capabilities of CMS in a myriad of ways. The muon trigger has been used in the search for suppression of quarkonium states. This is an important probe of the correlation length within the hot dense state known as the quark gluon plasma (QGP). The tracker has been utilized for to study charged particle multiplicities, and and elliptical flow, two probes of the thermal expansion of the QGP. HCAL has aided in measuring jet suppression, which probes the strength with which the QGP interacts with strong interacting objects. Through

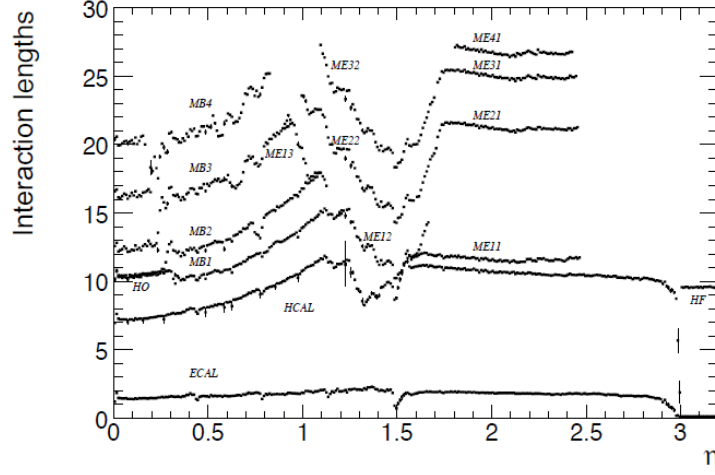


Figure 3.8: The amount of material in CMS as a function of  $\eta$  in number of interaction lengths.

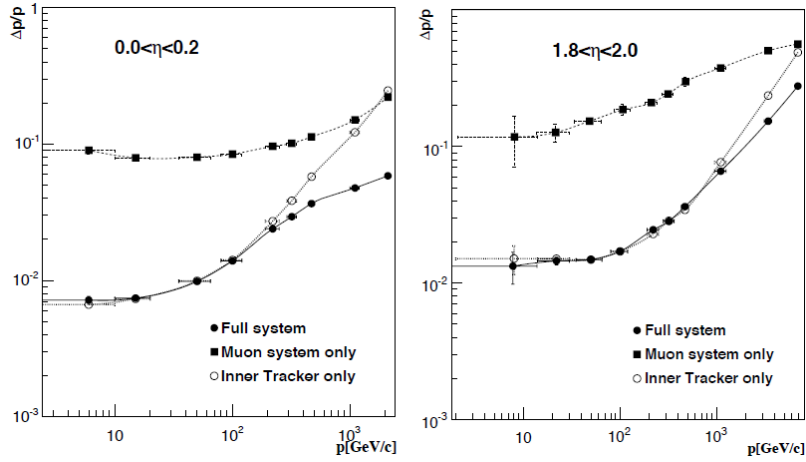


Figure 3.9: The momentum resolution of the muon system using only the tracker and the whole muon system in the barrel (left) and end cap (right).

its general purpose design and its ability to handle the high multiplicities produce by the LHC, CMS proves to be an excellent detector for investigating strongly interacting matter through heavy ion collisions.

### 3.6 Trigger

The CMS trigger is two tiered. The L1 trigger is the lower level hardware based system. The High Level Trigger (HLT) is software base and runs on a computer farm at point 5 where CMS is

housed.

The purpose of the L1 trigger is to make quick decisions about which events will be kept temporarily for further processing. The L1 trigger is used to identify events where the tracker should be read out. Only the calorimeters and the muon system are used in the L1 trigger. Each of the sub-detectors has its triggering hardware. The output from the sub-detectors is synchronized to ensure that the signal from each of the sub-detectors comes from the same collision. The global trigger hardware then makes the final decision to initiate the HLT and to read out the tracker.

If an event passes the L1 trigger, the data from all the sub-detectors including the Tracker are sent to the HLT computing farm. At this level the raw data from all the sub-detectors is unpacked and combined. The information from the calorimeters, muon system, and tracker can all be used to reconstruct basic physics objects in the HLT farm. For example, tracks can be combined with either ECAL energy clusters to form electron candidates, tracks can be combined with hits in the muon system to create muon candidates. At the HLT the whole detector is used together to select events. The raw data from the events that survive the HLT are recorded permanently, those that do not are lost forever.

The HLT farm must always be ready to accept events from the L1 trigger. For this reason, the amount of computing time each HLT trigger path uses must be balanced. For more rare L1 triggers, which will occur at a lower rate, more complex reconstruction software can be used. Conversely, simpler, faster, methods must be used for more common high rate triggers. Because of this time constraint in the HLT farm, the reconstruction algorithms used for triggering tended to differ from the final reconstruction algorithms. In the HLT these algorithms are optimized for quickness, whereas the final reconstruction is optimized for precision and accuracy. By having the ability to spend different amounts of computing time on different L1 triggered events, the complexity of the event selection offered by the HLT is heightened.

The two tiered triggering system creates very low dead times while maintaining purity and selectivity. During data taking the L1 trigger is continuously monitoring, and the HLT allows for sophisticated event selection. The wide gamete of physics topics that are pursued by the CMS

collaboration are a testament to the effectiveness and versatility of the CMS two tiered triggering system.

# Chapter 4

## Analysis

In this chapter the various parts of the measurements done for this thesis are explained. The following chapter contains seven sections explain each of these parts: Monte Carlo simulation, trigger development, data sets and event selection, break-up determination, signal extraction, efficiency determination, and systematic checks. In Section 4.1, the simulations used to estimate the detectors ability to measure UPC processes are discussed. Section 4.2 explains the considerations that went into the triggers which were developed for the analyses discussed in this thesis. How the final events were selected and how triggers were used to separate the data in to data sets is detailed in Section 4.3. Extraction of the number of events from each of the three physics processes discussed in this thesis, coherent, incoherent, and photon-photon process from the final selected events is discussed in Section 4.5. The determination of the detectors efficiency for measuring UPC events is explained in Section 4.6. Section 4.7 lays out how the systematic uncertainties are estimated.

### 4.1 MC simulation

Every physical measurement is the product of the underlying physics folded with the response of the detector used to do the measurement. In order to understand the underlying physical process, the detector's effect on the measurement must be understood and accounted for. As instruments become more and more complicated, the interplay between all of the many parts of the detector

makes an analytic approach to the problem untenable. For this reason, the numerical technique of Monte Carlo (MC) simulation is the most useful approach.

MC simulations use random number generation to solve the problem numerically by brute force. First, particles are generated according to the theoretical distributions. These particles are then propagated through a simulation of the detector. As the particles pass through the detector, random numbers are again used to determine how these particles interact with the materials of the detector based on the known properties of the material. In this way, the theoretical distributions are merged with the realistic response of the detector. The collective combination of the many sub detector responses with the theoretical distributions emerges from the successive creation of random events. The result is the convolved response of the detector with the underlying physical process that is to be studied.

In this thesis, two main classes of MC simulation samples were used. The first class uses STARlight to generate events. This class of MC samples corresponds to the theoretical calculations described in Section 2.5. There are three different physical processes described. Coherent  $J/\psi$  production, where the photon couples to the nucleus as a whole, incoherent  $J/\psi$  production, where the photon couples to a nucleon within the nucleus, and the photon-photon process, where the photons from the two nuclei interact with each other to produce a lepton pair directly. All three STARlight samples produce a  $\mu^+$  and  $\mu^-$  in the final state that interacts with the detector. The second class uses PYTHIA6 to decay  $J/\psi$ s with a given input  $p_T$  and rapidity distribution. Two samples of this class of particle gun data were produced each with different  $p_T$  distributions (See Fig.).

Because STARlight is not integrated into the standard CMS software framework (CMSSW), a simulation software chain using STARlight was developed for the analysis described in this thesis. The software chain used for producing the STARlight samples has five steps. First, STARlight is run in the specified mode, and a single file is created for each physics process, for this thesis, one file for the coherent process, the incoherent process, and the photon-photon process for a total of three files. The output from the STARlight generator is in a format specific to STARlight, therefore,

the output from the original generation step is then converted to the Les Houches (LHE) format. In this conversion to LHE format, either the parent  $J/\psi$  for the  $J/\psi$  production samples, or the initial photon-photon pair are added to the LHE output file. The standard STARlight output only includes the final state particles. Additionally, the initial output from STARlight is split into a collection of smaller LHE files so that each of the smaller samples can be processed in parallel. Each of the LHE files is used as input to CMSSW. The three remaining steps take place within the framework. First the generated particles are propagated through the GEANT4 detector simulation. This accounts for all the interactions with the detector and produces as output a format identical to the raw data that is recorded during data taking. The next two steps are identical to data taking. The reconstruction software used during data taking is run on the output of the detector simulation, and last, the output of the reconstruction is reduced to the information that is needed for the final analysis.

The particle gun samples were created entirely within CMSSW. An interface to PYTHIA6 is included within CMSSW, which takes  $J/\psi$   $p_T$  and rapidity distributions as input. The  $J/\psi$  are created according to the input distributions, and then uses PYTHIA6 to decay the  $J/\psi$ s to  $\mu^+$  and  $\mu^-$ . As with the STARlight samples, these muons are propagated through the GEANT4 simulation of the detector, and the raw data is produced. The remaining steps of running the reconstruction code and reducing the data to the final data needed for the analysis are identical to the STARlight production.

The five MC samples, three STARlight samples, and two particle gun samples, differ primarily in the  $p_T$  distribution of the  $J/\psi$ s produced and the polarization of the  $J/\psi$ s, which effects angle at which the muon daughters are emitted relative to the direction in which the  $J/\psi$  is traveling. In Fig. 4.1 the  $p_T$  of  $J/\psi$ s from the coherent and photon-photon samples are peaked steeply a low  $p_T$ , and neither sample extends much beyond 0.15 GeV in  $p_T$ . The incoherent sample is peaked near 0.5 GeV and extends beyond 1 GeV. The two particle gun samples resemble the incoherent and coherent samples. The first sample has a Gaussian  $p_T$  distribution extending to approximately 0.15 GeV, whereas the second is flat in  $p_T$  up to 2 GeV. The particle gun samples are unpolarized, whereas the STARlight samples have transverse polarization. Therefore, the particle gun samples



there is no preferred direction for the emission of the daughter muons. In the STARlight samples however the daughters tend to be emitted in line with the direction of the  $J/\psi$ 's momentum. This is particularly pronounced for the photon-photon process.

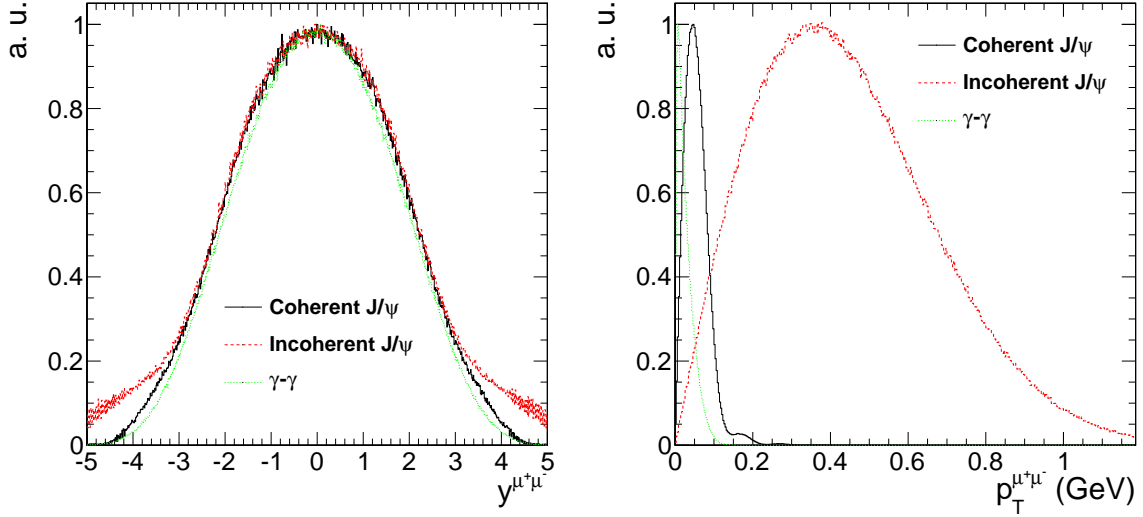


Figure 4.1: Generator level rapidity (left) and  $p_T$  (right) distributions for the coherent (black), incoherent (red), and photon-photon process (green).

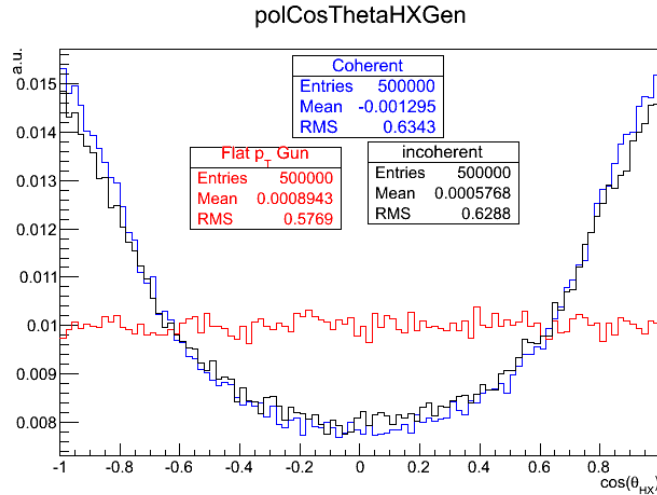


Figure 4.2: The  $J/\psi$  polarization of the particle gun (red), coherent (blue), and incoherent samples are plotted as the cosine of the helicity angle.

The momentum of the final state muons is the main drivers of whether the candidate can be measured. The polarization and the  $p_T$  distribution of dimuons from the generator determine

the momentum of the daughters. The polarization effects how the momentum is shared between the daughters. In the rest frame of the parent particle from which the daughters decay, equal momentum is given to each daughter. However in the lab frame of the detector, the muon daughters which are emitted from transversely polarized  $J/\psi$  will tend to be emitted in the direction of  $J/\psi$  and will have unequal momentum in the lab frame. The daughter traveling in the direction of the  $J/\psi$  will have increased momentum, whereas the daughter traveling opposite to the  $J/\psi$  direction will have decreased momentum. The combination of these two effects create a muon with very low momentum compared to the typical momenta of muons measured by CMS. The momentum of the lower momentum muon daughters is the main restriction on whether or not the  $J/\psi$  can be measured.

## 4.2 Trigger development

CMS collected dedicated UPC triggers for the first time during the 2011 PbPb run. Design of the UPC triggers required studies of the 2010 data to estimate rates and ensure that the bandwidth used by these trigger would be sufficiently low. All the different physics analyses must share the limited readout rate of the detector. For this reason, conservation of bandwidth was a major design consideration.

The 2010 rates were used to extrapolate to the interaction rate of the 2011 i run. The unique UPC triggers were estimated by combining existing triggers from the 2010 run. By calculating the ratio between the UPC trigger rates and the minimum bias trigger rate, the UPC trigger rates were scaled up to the 2011 interaction rates using the 2010 data. The extrapolated rates allowed for a package triggers to be created that fit within the bandwidth requirement of CMS Heavy Ions group.

The trigger package for 2011 contained ZDC based efficiency monitoring triggers, muon and electron based triggers for measuring  $J/\psi$ , and backup triggers in case there was a problem with the original muon and electron triggers. In order to record the trigger efficiency monitoring data,

the ZDC triggers had to be prescaled to a lower rate. The scaling down of the monitoring triggers were setup to insure overlap with the signal triggers. By balancing the competing objectives of rate reduction and increasing the overlap between the monitoring and signal triggers, the prescales for the trigger were as seen in Table 4.1.

### 4.2.1 L1 trigger

The goal of the L1 triggers was to record enough data to measure dimuons and dielectrons in UPC events. To achieve this, the loosest muon trigger and lowest threshold ECAL triggers were paired with a trigger on energy in the ZDC and a veto on energy in the BSC. Additional triggers that vetoed on energy in HF were commissioned in case radiation damage during the run reduced the sensitivity of BSCs. The L1 package that was constructed for the analysis of UPC  $J/\psi$  is presented in Table 4.1.

L1 Trigger Seed	Type
MuonOpen and (ZDC <sup>+</sup> or ZDC <sup>-</sup> ) and BSC veto	Physics
ECAL2 and (ZDC <sup>+</sup> or ZDC <sup>-</sup> ) and BSC veto	Physics
ECAL5 and (ZDC <sup>+</sup> or ZDC <sup>-</sup> ) and BSC veto	Physics
(ZDC <sup>+</sup> or ZDC <sup>-</sup> )	Monitor
MuonOpen and (ZDC <sup>+</sup> or ZDC <sup>-</sup> ) and HF veto	Backup
ECAL2 and (ZDC <sup>+</sup> or ZDC <sup>-</sup> ) and HF veto	Backup
ECAL5 and (ZDC <sup>+</sup> or ZDC <sup>-</sup> ) and HF veto	Backup

Table 4.1: List of 2011 L1 seeds.

The cumulative L1 trigger rate for all the UPC L1 trigger seeds was required to be 200 Hz. This requirement stemmed from the need to keep the tracker read-out rate low. The trackers baseline voltage can fluctuate due to the high tracker hit multiplicities in PbPb collisions. In order to monitor the zero suppression of the tracker, the zero suppression algorithm was executed using the HLT computing farm rather than in the tracker firmware. The rate at which the tracker could be readout without zero suppression set the limit for the L1 bandwidth.

### 4.2.2 HLT trigger

As opposed to the L1 trigger, which reads out the tracker, the HLT has access to the tracker information. Reconstruction of a track in the pixel detector is used by the UPC paths. The use of the pixel detector only, as opposed to using the whole tracker including the silicon strip detector, allows for quick track reconstruction saving computing cycles. The requirement of at least one reconstructed pixel track for the HLT triggers was designed to reject backgrounds where no particles are reconstructed by the tracker.

HLT Trigger	
HLT_HIUPCNeuMuPixel_SingleTrack	Physics
HLT_HIUPCNeuEG2Pixel_SingleTrack	Physics
HLT_HIUPCNeuEG5Pixel_SingleTrack	Physics
HLT_HIMinBiasZDC_Calo_PlusOrMinus_v1	Monitor
HLT_HIMinBiasZDC_PlusOrMinusPixel_SingleTrack_v1	Monitor
HLT_HIUPCNeuHcalHfMuPixel_SingleTrack	Backup
HLT_HIUPCNeuHcalHfEG2Pixel_SingleTrack	Backup
HLT_HIUPCNeuHcalHfEG5Pixel_SingleTrack	Backup

Table 4.2: List of 2011 HLT trigger.

The total HLT output for the UPC trigger package was 20 Hz. The limiting factor for the HLT rate was the amount of disk space available to store the data. To meet the bandwidth the requirements and collect a significant sample of data for estimating efficiencies, the prescales for the triggers were set. The ZDC trigger that was passed through from the L1 was given a larger prescale to account for the higher rate relative to the more selective ZDC path, which also required a pixel track on the HLT.

## 4.3 Event selection

In order to investigate novel physics processes like UPC  $J/\psi$  production, the LHC has delivered unprecedented amounts of data. The data for this analysis was recorded during the 2011 LHC PbPb run. During this period,  $150 \mu b^{-1}$  were recorded by the CMS detector, corresponding to

over a billion PbPb collisions. Of this,  $143 \mu b^{-1}$  are used in this analysis.

### 4.3.1 Data sets

Three specially selected samples were used for the present analysis (see Table 4.3). These samples were recorded using subsets of the triggers found in Section 4.2. The  $J/\psi$  events discussed in this thesis were obtained analyzing the sample labeled in Table 4.3 as physics. A ZDC triggered sample was recorded for the sake of estimating efficiencies. Last, a zero bias sample was recorded for investigating the ZDC and the noise distributions of HF. By recording this hierarchy of samples, interesting events are selected with a much higher purity in the physics sample, while the zero bias and ZDC triggered samples allow for the investigation of the selection criteria.

To record the physics sample containing the  $J/\psi$  signal, a muon trigger was paired with a veto on energy in the BSC and a requirement that there be energy in at least one of two sides of the ZDC. This trigger utilizes the unlikely chance of having overlapping noise in in the ZDC and muon detector. Because of the characteristically low momentum of UPC  $J/\psi$  as compared to  $J/\psi$  created by any other physics process, the loosest muon trigger was used. By pairing the muon trigger with the ZDC on the L1, the noise contribution was reduced from the noise contribution from either of the two sub-detectors to the noise coincidence between the two sub-detectors. Contributions from hadronic interactions are reduced by the veto on the BSC. In this way the balance between reducing the rate and maximizing the efficiency was struck, allowing for the data to be recorded without producing high rates resulting in dead time for the detector.

In order to investigate the muon trigger and the other parts of the event selection, a minimum bias sample was recorded using the ZDC. For ZDC triggered sample, any event which had energy consistent with at least one neutron in either of the two sides of the ZDC was recorded. This process is much more common than the UPC  $J/\psi$  production. For this reason, the rates of this trigger are much higher than the physics trigger, and only a small sub set of these events are recorded. From this trigger the pixel track portion of the HLT trigger efficiency was estimated.

In addition to the minimum bias and physics sample, a zero bias sample was recorded to ex-

Sample	Events	$\mathcal{L}_{int}$
Physics	300K	143.3 $\mu b$
Minimum Bias	100K	X
Zero Bias	5M	580 b

Table 4.3: Integrated luminosities and number of events for the three samples used in this analysis.

amine the ZDC trigger and the HF noise distributions. The zero bias trigger fired every time both beams passed through CMS. Only 4 events out of every million triggered were recorded for this sample. This sample allowed for an unbiased measurement of the ZDC trigger efficiency as discussed in Section 4.6. Because the zero bias trigger does not require any activity in any of the CMS sub detectors, the sample contains very few hadronic collisions. This allowed for a measurement of the electronic noise distributions in the HF, which will be discussed below.

The integrated luminosity for each of the three samples is calculated by recording activity in HF [15]. The cross section for HF activity is measured from a van der Meer scan, and the cross section was found to be X. In this way the amount of integrated luminosity for any running period is related to the activity in HF.

### 4.3.2 Event selection cuts

The analysis described in this thesis focuses on UPC  $J/\psi$ s decaying to muons. The trigger used for this analysis recored 346841 events. A set of off-line cuts were applied to increase the relative contribution of UPC events to background processes. Two sets of event selection cuts were applied to reject background events. The first set rejects background from the beam. The second rejects events where hadronic collisions have occurred. The cuts in Table 4.4 were applied.

To reject beam induced background the following cuts were applied:

- The reconstructed vertex must be within X cm in the transverse direction and X cm in the longitudinal direction. This cut insures that reconstructed particles come from interactions between the two beams rather than event where one of the two beams interact with gas particles near the interaction point.

cut	cut type	events
all triggered	–	346841
good vertex requirement	beam background rejection	340997
beam halo muon rejection	beam background rejection	302777
cluster shape compatibility requirement	beam background rejection	233590
single-sided neutron requirement	hadronic interaction rejection	149992
two track requirement	hadronic interaction rejection	32732
HF signal rejection	hadronic interaction rejection	5392
muon quality requirement	fake muon rejection	1956
$J/\psi$ mass requirement	kinematic cut	662
muon detectability cuts	kinematic cut	541

Table 4.4: Effects of event selection cuts.

- Beam halo muons were rejected using the timing of the muon hits. The beam halo cut rejects events where muons surrounding the beam stream through the detector.
- Pixel cluster shape should be compatible with the vertex. This cut requires that energy deposits in the silicon tracker point back to the reconstructed primary vertex.

These beam background cuts do not reject any UPC  $J/\psi$  candidates.

The second set of background rejection cuts were designed to reduce contamination from hadronic interactions.

- No more than 2 reconstructed tracks in the event. The track requirement rejects events that produce many charged particles.
- Maximum reconstructed hit energy in HF was required to be below the threshold for electronic noise. Nearly all hadronic interactions (about 98%) produce particles in the range  $3 < |\eta| < 5$  covered by the HF detector. By requiring that the energy deposits in HF resemble noise, nearly all elastic hadronic collisions are expected to be rejected.
- Energy in the ZDCs consistent with neutrons on only one side of the interaction point. In hadronic interactions both nuclei break-up. By requiring that ZDC only reconstruct neutrons on one side of the interaction point, hadronic interactions that produce neutrons on both sides were rejected.

Each of these cuts were designed to reject topologies produced by hadronic interactions. The effect of these cuts can be seen in Table 4.4 and are denoted hadronic interaction rejection.

To establish the HF noise thresholds, the noise distributions were measured in zero bias events. Only presences of both beams was required for these events to be recorded. An offline selection of events with no reconstructed tracks was used to ensure that no collision had taken place. The HF noise threshold was defined as the cut that keeps 99% of the zero bias events. The noise distribution from this zero bias sample is compared to the physics sample and MC in Fig. 4.3.

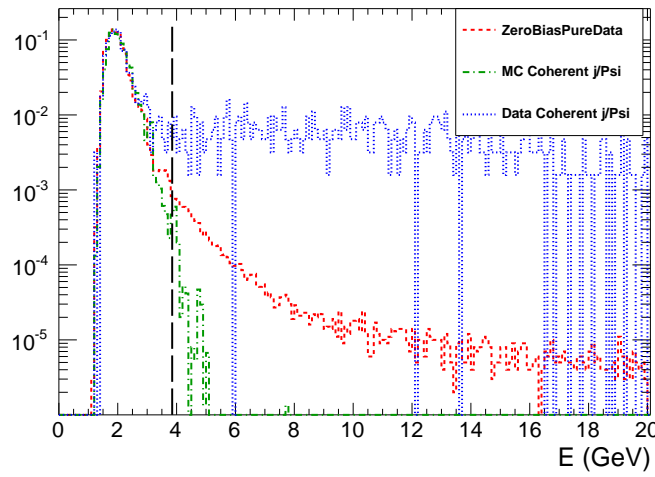


Figure 4.3: Comparison of HF noise distributions in zero bias data, physics triggered data, and MC.

The following standard muon quality cuts are applied:

- Tracker track matched with at least one muon segment (in any station) in both X and Y coordinates ( $< 3 \sigma$ ).
- Cut on number of tracker layers with hits  $> 5$ .
- Number of pixel layers  $> 0$ .
- The  $\chi^2$  per degrees of freedom of the track fit  $< 3$ .
- Loose transverse and longitudinal impact parameter cuts, with in 3 cm in the transverse direction and withing 30 cm in the longitudinal direction with respect to the primary vertex.



These cuts are applied to reduce the number of fake muons and have been validated for standard muon analyses.

## 4.4 Break up determination

As described in Section 2.6, UPC  $J/\psi$  photoproduction can be accompanied by the emission of neutrons from either of the two colliding nuclei. The various neutron emission scenarios, or break-up modes, can be distinguished by the ZDC. By separating events where the ZDC signal is consistent with 1 neutron versus several neutrons, the different break-up modes can be separated and compared to theory. For this reason, reconstruction of the ZDC signal plays an important role in this thesis. In order to maximize the ability to explore the one neutron peak, which sits at the bottom of the ZDCs dynamic range, a new ZDC reconstruction method was devised. This new reconstruction method was then used to establish a one neutron and many neutron threshold. In this section the ZDC signal reconstruction is described and how the neutron thresholds on this signal were set.

### 4.4.1 ZDC signal reconstruction

The ZDC signal is built up from the pulse shapes for each of the 18 individual ZDC channels. The pulse shape is recorded in 250 ns second chunks and is divided into 10 time slices of 25 ns (See Fig 4.4). Counting from 0, the 4th time slice is synced with the timing of the rest of the detector and corresponds to when the products of the recorded collision reached the ZDC. For this reason the channel signal is taken from the 4th time slice.

The ZDC signal sits on top of a low frequency noise pedestal. Over the time scale of 250 ns, this low frequency noise signal appears as a constant that shifts randomly from event to event. The contribution from this noise is therefore measured event by event in order to subtract it. Time slice 5 is used for this purpose.

Time slices 1 and 2 could also be used to estimate the low frequency noise. However because the noise fluctuates to negative values of charge that cannot be measured, these time slices can only

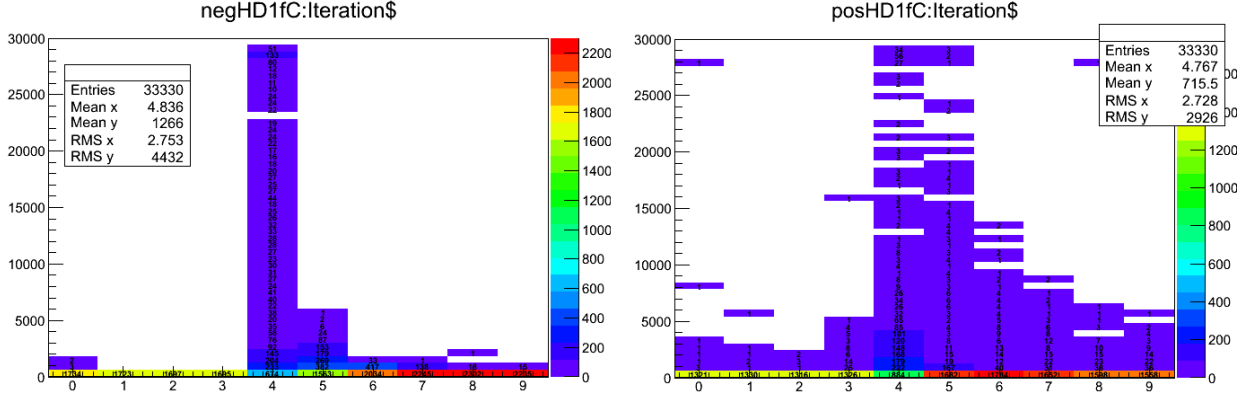


Figure 4.4: Average ZDC pluse shape is plotted as the charge as a function of time slice for the first hadronic from  $ZDC^-$  (left) and  $ZDC^+$  (right).

provide a measurement of the noise half the time. By using time slice 5 which contains the falling tail of the signal, the noise can be measured any time the signal raises significantly above the noise. If the fraction of signal in time slice 4 and 5 are constant and the noise contributes the same value to both time slices, the following formula is applicable:

$$Ts4 \propto (Ts4 + C) - (Ts5 + C) = Ts4 - R_{Ts5/Ts4} Ts4 = Ts4(1 - R_{Ts5/Ts4}), \quad (4.1)$$

where  $Ts4$  is the signal contribution in time slice 4,  $Ts5$  is the signal contribution to time slice 5,  $C$  is a random noise constant from the low frequency noise, and  $R_{Ts5/Ts4}$  is the ratio between the signal contribution from time slice 5 over time slice 4. Fig. 4.5 demonstrates the consistence of the fraction and validates the unconventional method of using the falling tail of the signal to estimate the low frequency noise. By using time slice 5, the chances of measuring the noise are maximized. Separating the signal from the noise is especially important because the ZDC signal for the one neutron peak sits near the noise at the bottom of the ZDC dynamic range.

To measure one signal value for  $ZDC^+$  and one for  $ZDC^-$ , the signals from each of the channels are combined. Channels from the EM section and HD section are combined first. Only channels with signal above zero in time slice 5 and time slice 4 are included. The EM section of the calorimeter is more densely packed with optical fibers and therefore has a higher gain relative

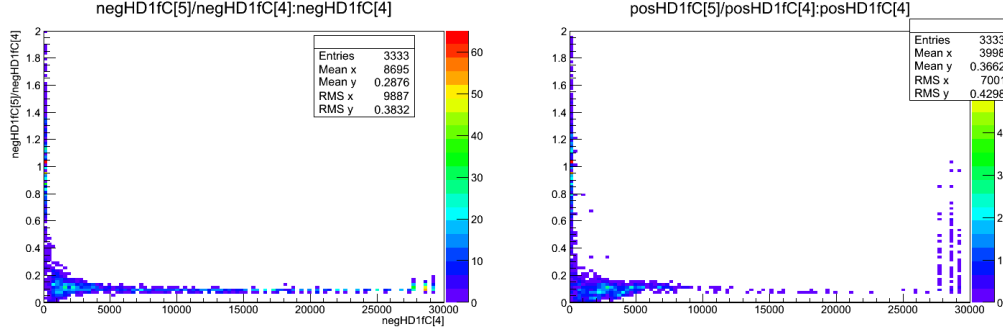


Figure 4.5: The fraction of signal in time slice 5 over time slice 4 as a function of the signal in time slice 5 in  $ZDC^-$  (left) and  $ZDC^+$  (right).

to the HAD section. To account for this, the combination of EM channels is weighted with a factor of 0.1 to match the HAD channel gains. The value for each side of the ZDC's signal is given by the sum of the HAD channel combination and weighted EM channel combination. It is this signal, one for  $ZDC^+$  and one for  $ZDC^-$ , which is plotted in Fig. 4.6 to measure the neutron thresholds.

#### 4.4.2 Determination of the one neutron thresholds

The ZDC thresholds used to establish the various break-up modes were measured from zero bias data. By using this dataset, the neutron spectrum does not contain a trigger bias. Zero bias trigger required that both beams were present in CMS. This does, however, include a significant electronic noise contribution due to events where no neutrons are emitted in the direction of the ZDC.

To determine the thresholds for one and multiple neutrons, the  $ZDC^+$  and  $ZDC^-$  spectra were fit. Four Gaussian functions were combined to fit the spectra. The electronic noise was fit to a Gaussian around zero. The one, two, and three neutron peaks are fit to Gaussians that are successively broader. The mean of each peak was initially set to multiples of the mean of the one neutron peak. The threshold for a neutron in the ZDC was taken from the fits in Fig. 4.6. Any signal greater  $2\sigma$  below the mean of the one neutron peak was considered signal. Any signal greater than  $2\sigma$  above was considered multiple neutrons. In this way the single neutron break up modes could be separated from the multiple neutron modes.

Several of the break-up mode calculations that have been done involve single sided configura-

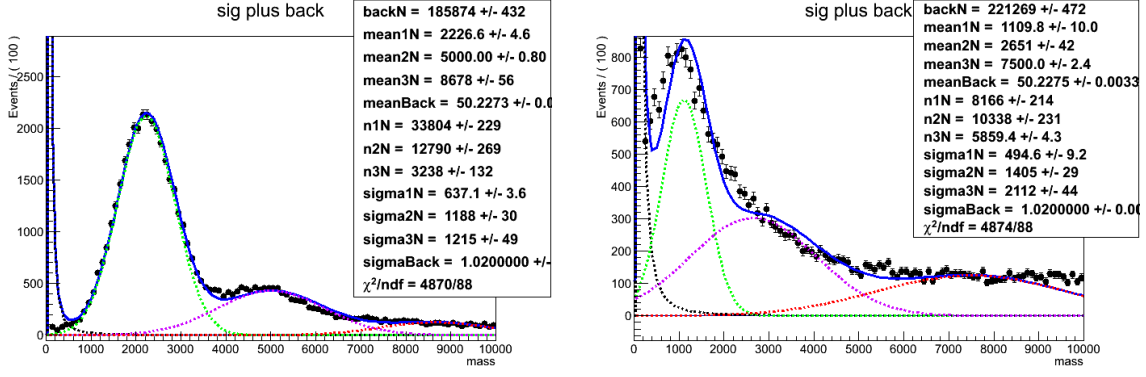


Figure 4.6: Fit to the signal spectra for ZDC<sup>-</sup> (left) and ZDC<sup>+</sup> (right)

tions where neutrons are present on one side of the interaction point and not the other. To identify signal consistent with noise, noise distributions for the combined EM sections and the combined HAD sections were measured. The beams are only made to collide every 200 ns. In Fig. 4.4 higher than average signal can be seen in the 0th time slice, which precedes the main signal time slice time slice 4 by 200 ns. This is due to events where activity was present in the ZDC for two consecutive collisions. Time slices 1 and 2, however, occurred between collisions. These time slices were used to estimate the noise spectrum.

Fig 4.7 shows the noise spectrum for each of the EM and HAD sections for the two sides of the ZDC. As with the signal measurements, the low frequency noise pedestal is subtracted event by event by subtracting time slice 2 from time slice one before the channel signals are combined for each section. A side is considered consistent with noise if both HAD section and EM section signal measurements from the signal method involving time slice 4 and time slice 5 are lower than 2 sigma below the mean in Fig. 4.7. With the single neutron, multi-neutron, and noise thresholds established, the contributions to the various break-up modes were estimated and compared to theory.

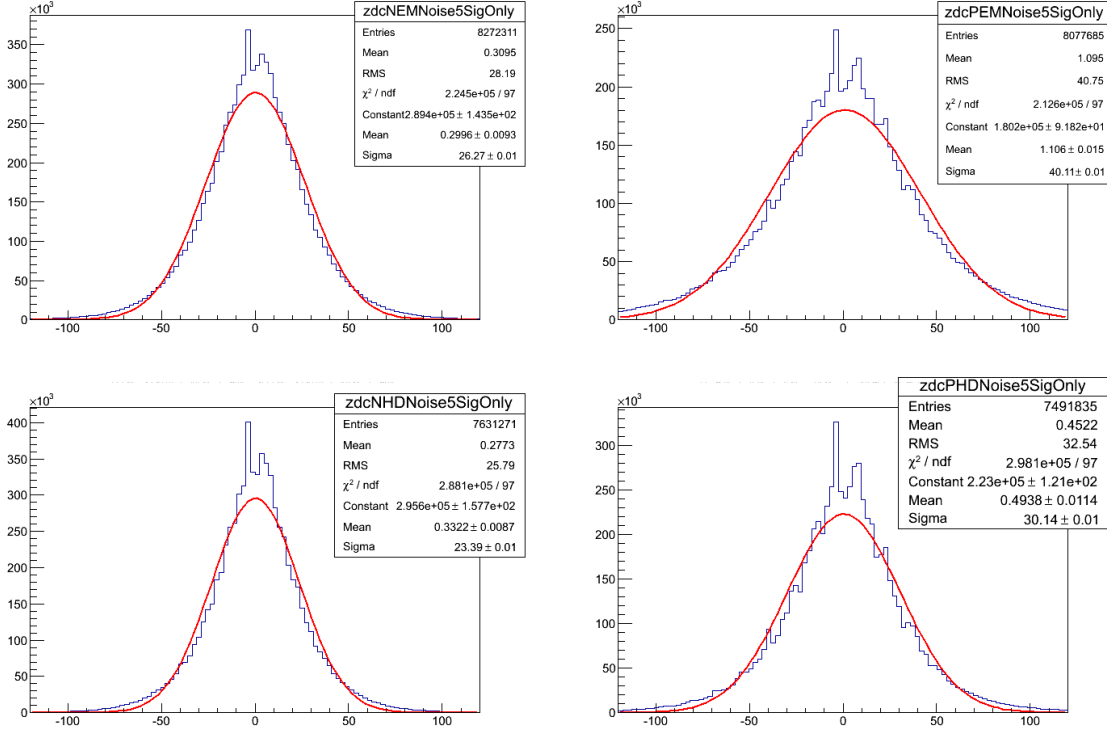


Figure 4.7: ZDC noise spectra from  $ZDC^-$  EM section (upper left),  $ZDC^+$  EM section (upper right),  $ZDC^-$  HAD section (lower left), and  $ZDC^+$  HAD section (lower right).

## 4.5 Signal extraction

After all event selection cuts, the coherent  $J/\psi$ , incoherent  $J/\psi$ , and photon-photon process all contribute to the remaining events. Each process must be separated from the final mix. To achieve this, the invariant mass and  $p_T$  distributions are used to distinguish between the three processes. The photon-photon process is extended in invariant mass whereas the  $J/\psi$  is peak strongly near 3.1 GeV. In  $p_T$  the photon-photon and coherent process have similar distributions, both peaked shapely below 0.1 GeV, whereas the incoherent process is more broadly distributed across an interval extending to nearly 1 GeV. The mass distribution was fit to separate the photon-photon process from the  $J/\psi$  process. The  $p_T$  distribution was used to separate the incoherent process from the photon-photon process, and the coherent process. In this way, a separate yield was extracted for all three processes.

The invariant mass distribution for opposite sign dimuons is shown in Fig. 4.8. A  $J/\psi$  signal

is clearly visible together with tails at higher and lower mass due to the photon-photon process. A fit to the invariant mass distribution was done using a Gaussian to account for the  $J/\psi$  signal and a first order polynomial function for the photon-photon process. The extracted number of  $J/\psi$  candidates from this fit includes all  $J/\psi$ s in the mass window that passed the analysis cuts, i.e. both coherent and incoherent process contribute to yield from the mass fit. The  $p_T$  distribution is needed to separate the two different contributions to the  $J/\psi$  peak.

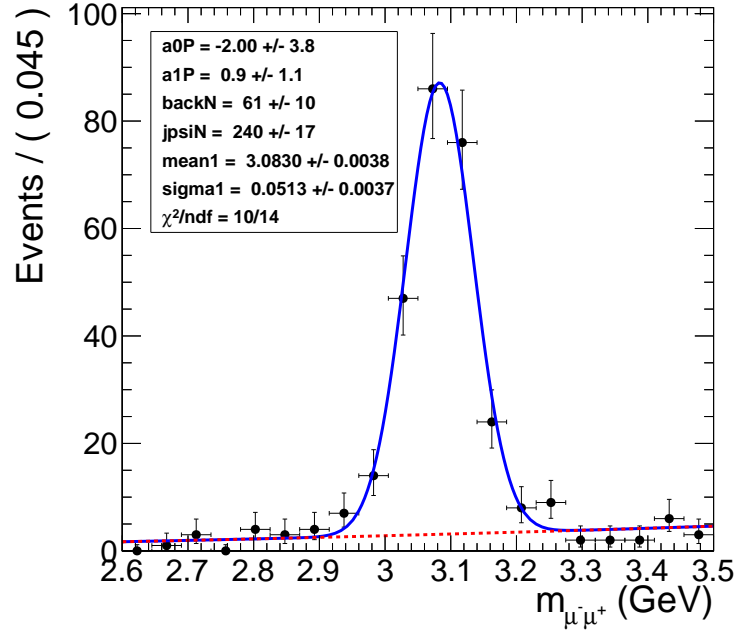


Figure 4.8: Mass fit to  $J/\psi$  using Gaussian for the signal and a first order polynomial for the photon-photon continuum

The same candidates from Fig. 4.8 were plotted as a function of  $p_T$  in Fig. 4.9. The clear overlap of the coherent and photon-photon process, and the clear separation of these two lower  $p_T$  processes from the incoherent process is apparent. The shape of the  $p_T$  distribution for the coherent, incoherent, and photon-photon process are taken from the final output of MC after applying all analysis cuts. To obtain the yields for each of the three process, the  $p_T$  distribution was fit to the three templates. In Fig.4.9, the yield parameters that were fit were left unconstrained for all three process.

The shape of the photon-photon and coherent  $J/\psi$  process are very similar in  $p_T$ . Accordingly,

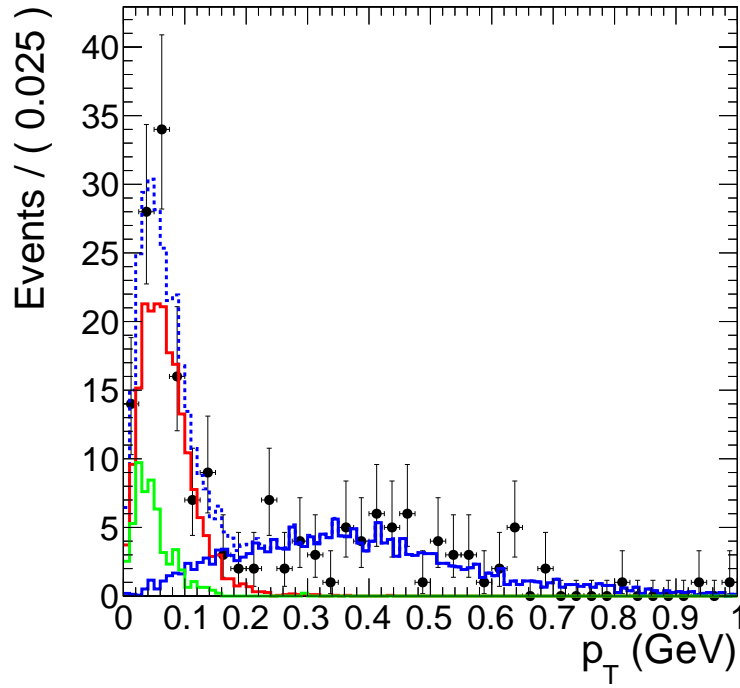


Figure 4.9: Fit to MC  $p_T$  templates.

the contribution from the photon-photon process and the coherent process are difficult to separate from the  $p_T$  distribution. The confidence contours in Fig. 4.10 from the template fit in Fig. 4.9 demonstrate the strong anti-correlation between the coherent yield parameter,  $nCo$ , and the yield parameter for the photon-photon process,  $nGamma$ . Because of the anti-correlation, the statistical uncertainty on  $nCo$  and  $nGamma$  from the fit are larger than  $\sqrt{nCo}$  and  $\sqrt{nGamma}$  expected from Poisson statistics. The information from the invariant mass and  $p_T$  distributions were combined to break this correlation. Through this combination, the contribution to the final yield from the three process was measured.

To utilize the mass fits ability to distinguish the photon-photon process from the coherent and incoherent process all while utilizing the  $p_T$  fits ability to separate the coherent and photon-photon processes from the incoherent, a simultaneous fit to the mass spectrum and  $p_T$  spectrum was performed. Fig. 4.11 shows the result of the simultaneous fit. The simultaneous fit forces the parameter  $nGamma$  to both describe the photon-photon continuum present in the side bands of the  $J/\psi$  mass peak as well the photon-photon contribution to the low- $p_T$  part of the  $p_T$  spectrum. In

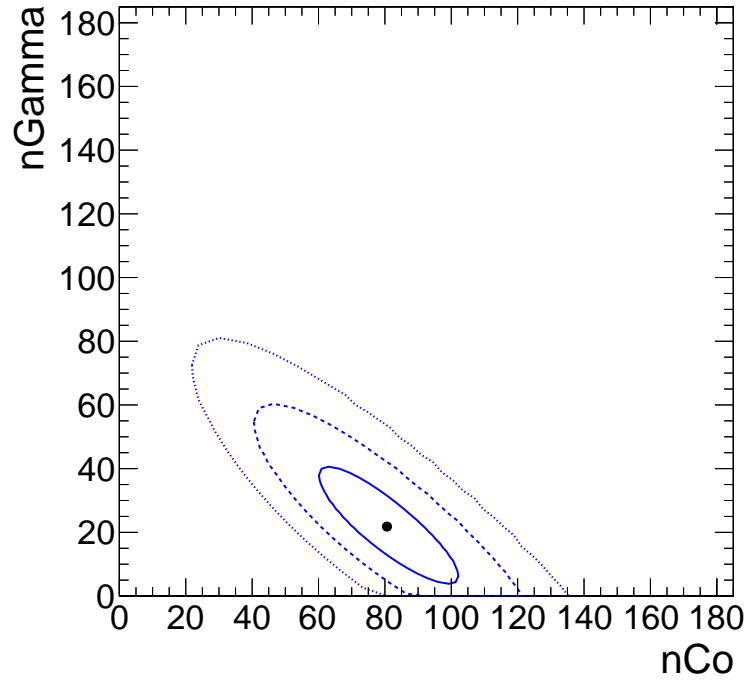


Figure 4.10: 68%, 95%, and 99% confidence contours from the  $p_T$  template fit.

addition, the  $J/\psi$  yield from the mass fit is forced to equal the contribution from the incoherent and coherent process in the fit to the  $p_T$  distribution. In this way, the correlation between the yield parameters was broken, and the contribution from the three process were made independent of each other.

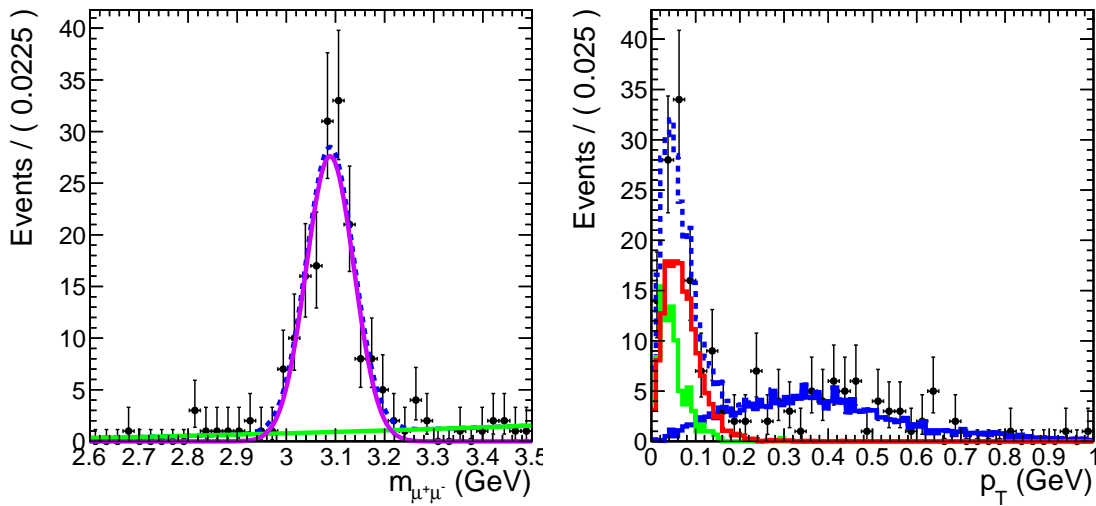


Figure 4.11: Simultaneous fit to the mass and  $p_T$  spectra.



The ambiguity between the coherent and incoherent processes in the mass fit and the ambiguity between the coherent and the photon-photon process was over come through used of the simultaneous fit. Fig. 4.12 shows the confidence contours for  $nCo$  and  $nGamma$  from the simultaneous fit in Fig. 4.11. The slope of the confidence contours in Fig. 4.12 is noticeably closer to 0 than the apparent negative slope in Fig. 4.10. The contours for the simultaneous fit are also reduced compared to Fig. 4.10 with widths in  $nCo$  and  $nGamma$  similar to those expected from Poisson statistics. From the simultaneous fit, reasonable statistical errors were obtained along with the yields for the three processes.

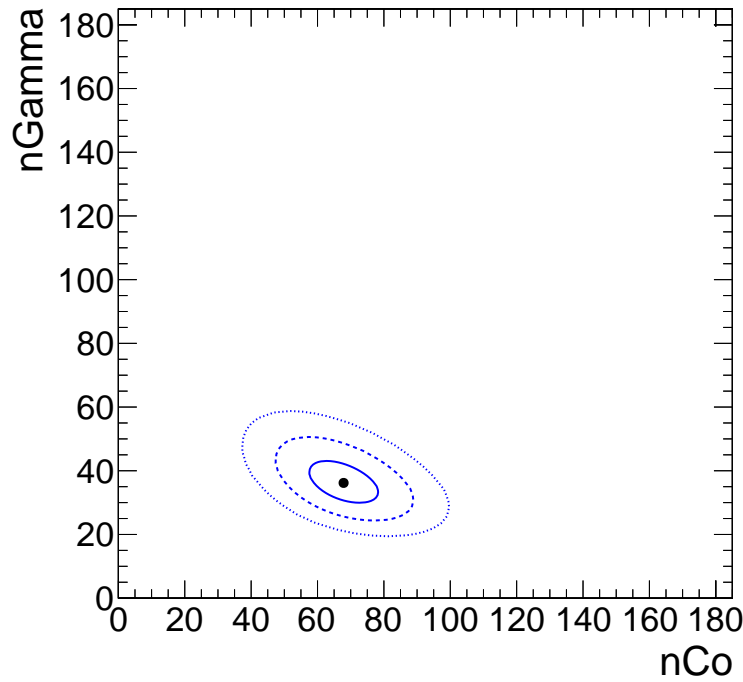


Figure 4.12: 68%, 95%, and 99% confidence contours from the simultaneous fit.

## 4.6 Efficiency determination

### 4.6.1 Muon efficiencies

The muon efficiencies are measured from MC and data. The MC based measurement accounts for the detector acceptance and the efficiency of the muon quality discussed in Section 4.3. The trigger

efficiencies were measured in data using the tag and probe method [16], which is discussed below.

CMS has a limited acceptance for  $J/\psi$ s, particularly in the case of  $J/\psi$ s with low momentum like those produced in UPC events. To measure the acceptance of CMS for  $J/\psi$ s, reconstructed dimuon candidates were considered detectable if both reconstructed daughters fell into a detectability region. This region was defined using the coherent  $J/\psi$  events obtained from STARlight. The efficiency for reconstructing single muons  $\epsilon_{reco}^\mu$  is defined by  $\epsilon_{reco}^\mu = \frac{N_{reco}^\mu}{N_{gen}^\mu}$ , where  $N_{reco}^\mu$  is the number reconstructed muons obtained after the full CMS detector simulation and that passed the standard muon quality cuts, and  $N_{gen}^\mu$  is the number of generated muons from STARlight. Fig. 4.13

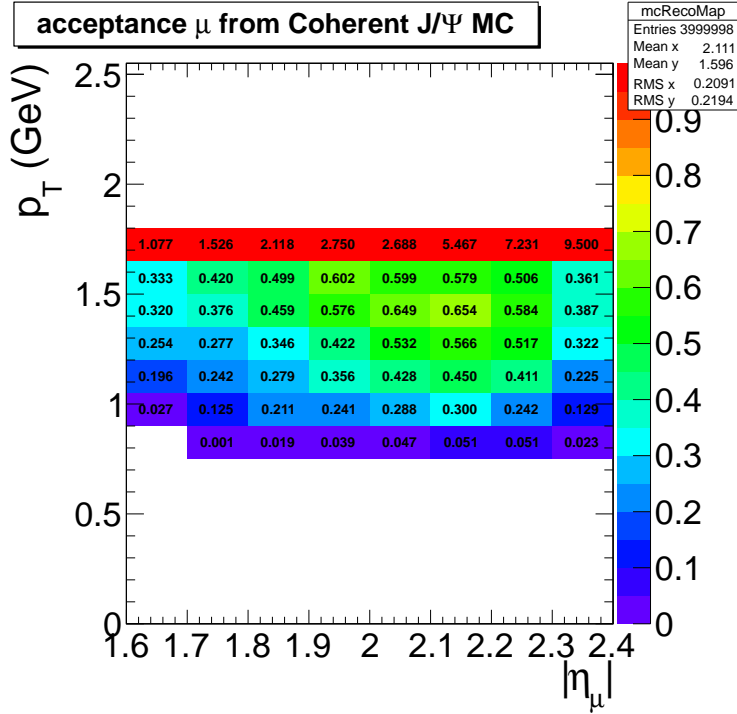


Figure 4.13: Muon daughter detectability from coherent  $J/\psi$

shows the efficiency for reconstructing single muons from coherent  $J/\psi$  events. To avoid the edges of the detectors acceptance, all reconstructed muons that fall into a  $(p_T, |\eta|)$  bin that has an efficiency less than 20% were rejected thus defining the detectability region. The acceptance for reconstructing dimuons was calculated from MC using the following formula:

$$A = \frac{N_{det}(|y|, p_T)}{N_{gen}(|y|, p_T)}, \quad (4.2)$$

where  $N_{det}$  is the number of reconstructed dimuons where both daughters fall into the detectability region, and  $N_{gen}$  is the number of generated dimuons. From Eq. 4.2, the acceptance for  $J/\psi$  was calculated as a function of  $|y|$ , and  $p_T$  (see Fig. 4.14).

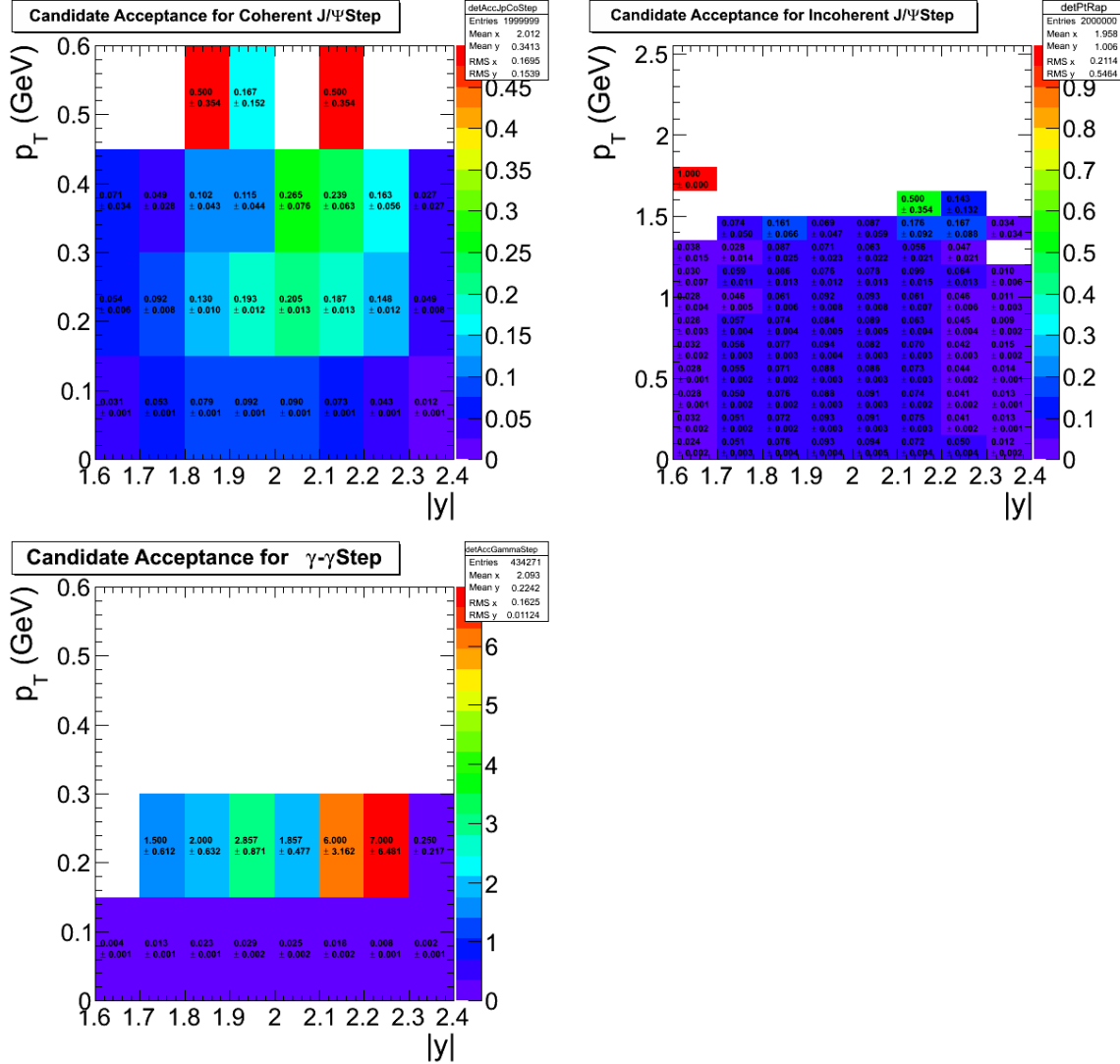


Figure 4.14: Dimuon acceptance from coherent  $J/\psi$  (top left), incoherent  $J/\psi$  (top right), and photon-photon interactions (lower).

The tag and probe method is used to measure the trigger efficiency of the muon daughters, which is a data driven approach. In this method there are three categories of daughter muons. *Tag muons* are high quality muons. *Passing probes* are reconstructed muons that match the muon trigger, while *failing probes* do not. Each dimuon will have one daughter classified as a tag and

the other as a probe. From here three invariant mass histograms are studied. One histogram is created from all pairs. The second comes from pairs where the probe is a passing probe. The last histogram comes from pairs where the probe fails to fulfill the trigger, *i.e.* the probe is a failing probe. Because this depends on the  $p_T$  and  $|\eta|$  of the probe, one set of three histograms for each  $(p_T, |\eta|)$  bin of the probe is created.

To extract the single muon trigger efficiency  $\epsilon_{trig}^\mu$ , each set of invariant mass histograms was simultaneously fitted. The signal was fitted using a Crystal Ball function, and the background was fitted to an exponential. The Crystal Ball parameters were simultaneously fitted to all three histograms. The exponential function was fitted to the failing and passing probe histograms separately. Because the background shapes are in principle different for the two samples, the efficiency is driven by this difference.

To measure the trigger efficiency a tag is required to pass all muon quality cuts and matched to the trigger. The probe is required to pass all quality cuts. A passing probe is a probe that is also matched to the trigger. In this way, the tag leaves the probe unbiased by the trigger and the efficiency can be measured by fitting the mass distribution.

Fig. 4.15 shows the fit of the three sets of pairs. This fit is done for each bin of the probes  $p_T$

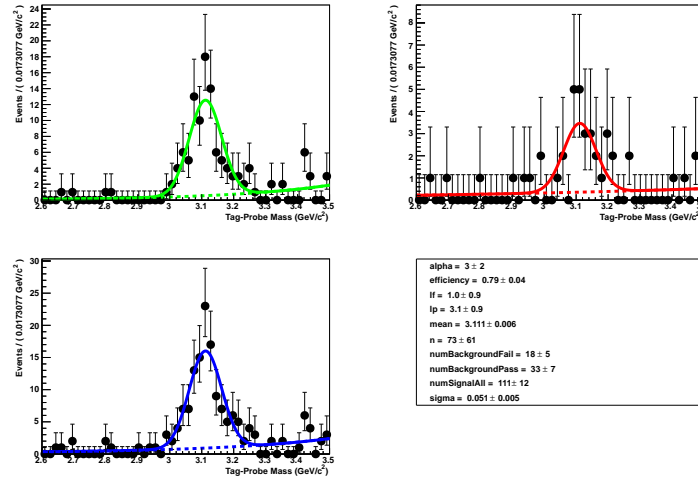


Figure 4.15: Fits to tag and probe pairs in the  $J/\psi$  mass region.

and  $\eta$ . The resulting fit is in Fig. 4.16.

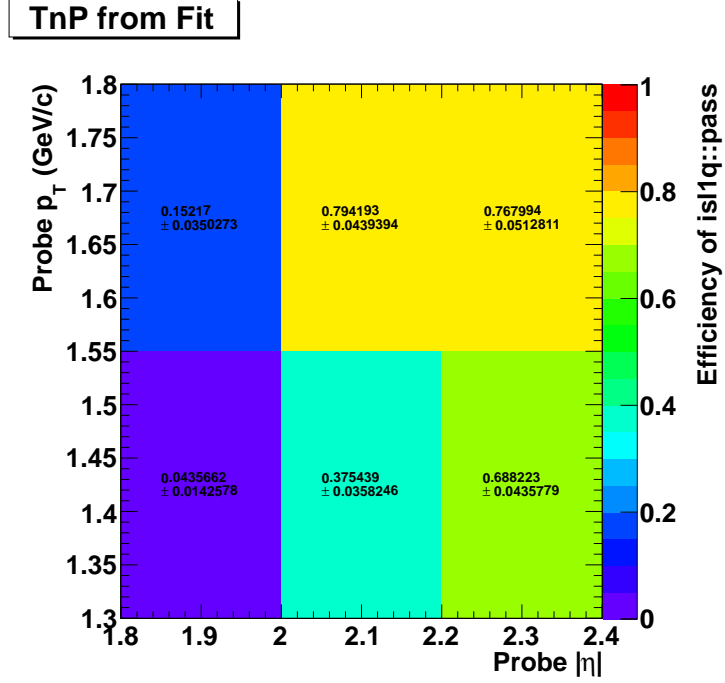


Figure 4.16: Muon trigger efficiencies in  $p_T$  and  $\eta$  bins from the tag and probe method.

The dimuon trigger efficiency  $\epsilon_{trigger}^{dimuon}$  was measured from the single muon efficiencies. The efficiency of each candidate was calculated using the following equation:

$$\epsilon_{trigger}^{dimuon} = 1 - (1 - \epsilon_{trigger}^{\mu_1})(1 - \epsilon_{trigger}^{\mu_2}), \quad (4.3)$$

where  $\epsilon_{trigger}^{\mu_1}$  is the tag and probe efficiency of the first dimuon daughter, and  $\epsilon_{trigger}^{\mu_2}$  is the efficiency of the second muon daughter. In Eq. 4.3 the probability of at least one daughter firing the trigger is calculated by subtracting one from the probability that neither daughter fires the trigger, thus giving the dimuon trigger efficiency.

The average dimuon trigger efficiency for each dimuon ( $p_T, |y|$ ) bin was calculated by averaging the individual dimuon candidates in each bin. The average trigger efficiency was multiplied by the acceptance from the MC to produce a total factor for both efficiency and acceptance.

The total combined efficiency and acceptance factor coherent  $J/\psi$  between  $2.0 < |y| < 2.2$  was found to be around 5%. The roughly 7% acceptance factor from the MC is the main contributor

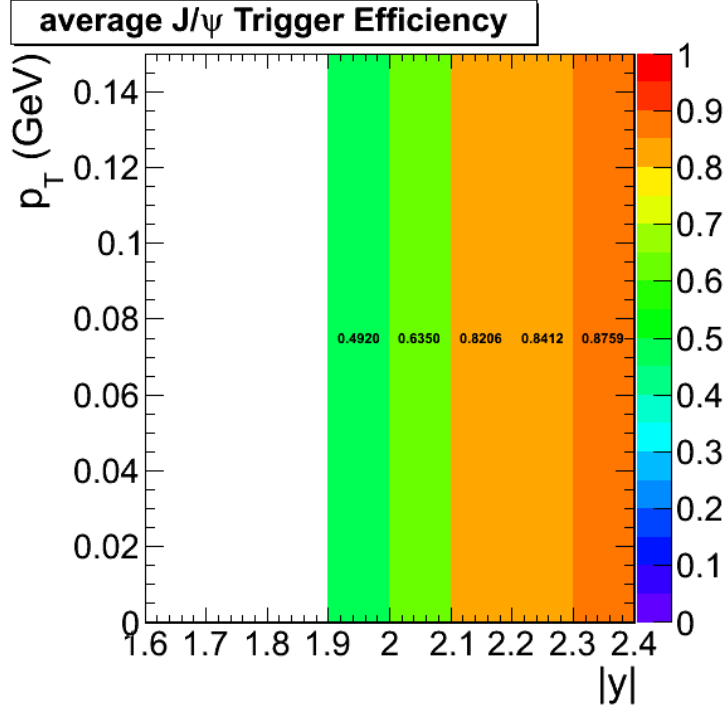


Figure 4.17: The trigger efficiency from tag and probe averaged over candidates in each  $(p_T, |y|)$  bin.

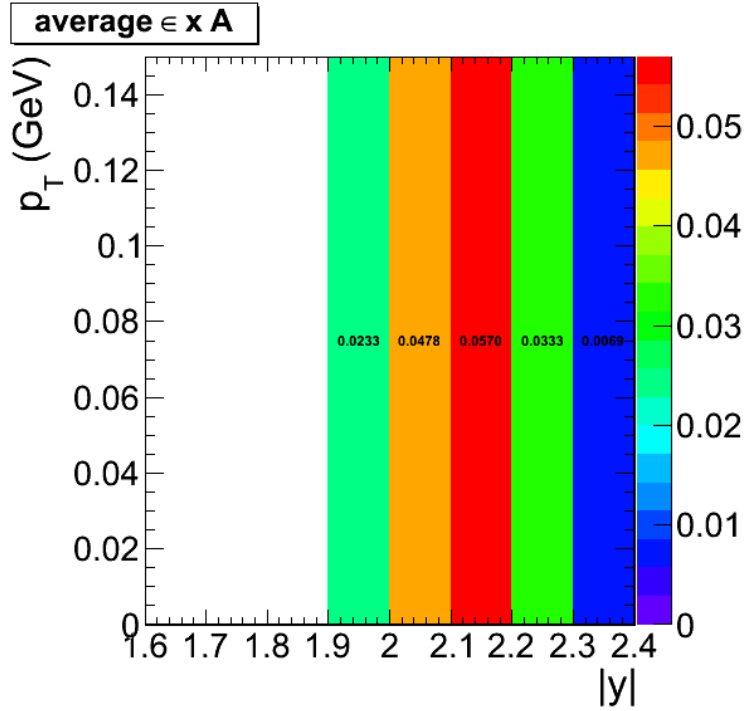


Figure 4.18: The acceptance times averaged trigger efficiency from tag and probe.

to the total efficiency. Primarily, the interplay of the polarization of the  $J/\psi$  and the material in detector drive down the efficiency by creating an effective momentum threshold for detection (see Section 4.1). The reconstruction efficiency of the daughters range between 20%-60% for muons in the defined detectability range. The trigger efficiency for the detectable muons ranges from 30%-80% depending on  $p_T$ . The typical trigger efficiency for the dimuons ranges from 60% to 80%.

#### 4.6.2 ZDC trigger efficiency

As discussed in Section 4.4, a special trigger was prepared to monitor the ZDC trigger efficiency. This trigger required either a  $ZDC^+$  or  $ZDC^-$  trigger, together with at least one pixel track. Events were accepted offline if there was no activity in the BSCs or activity on a single side.

This sample suffers from a trigger bias. For example, a sample triggered by  $ZDC^+$  would always produce a  $ZDC^+$  trigger efficiency of one. To avoid this, the special trigger sample was divided into two subsamples in the following way. A first sample triggered by the  $ZDC^+$  input and second one triggered by the  $ZDC^-$ . The  $ZDC^+$  trigger efficiency is measured from the  $ZDC^-$  sample, and vice versa.

The trigger efficiency for reconstructed ZDC energies above the single neutron threshold were estimated (see for Sec. 4.4). The  $ZDC^+$  efficiency was calculated using the  $ZDC^-$  triggered sample. To estimate the efficiency, the number of events with energy in  $ZDC^+$  greater than the single neutron threshold,  $N_{events}$ , were measured. From this set of events, the number of events that also fire the  $ZDC^+$  was measured. The ratio between the number of single neutron events that fired the trigger and all single neutron events was taken as the estimate of trigger efficiency. The same procedure was applied for each side of the ZDC. The trigger efficiency of the ZDC was found to be 98% for  $ZDC^-$  and 94% for  $ZDC^+$ .

ZDC Side	Reco Method	$N_{events}$	$N_{trig}$	$\epsilon_{ZDC}$
ZDC <sup>+</sup>	1	72946	71688	$0.982 \pm 0.005$
ZDC <sup>+</sup>	2	73028	71706	$0.9819 \pm 0.005$
ZDC <sup>-</sup>	1	76137	71786	$0.9429 \pm 0.005$
ZDC <sup>-</sup>	2	76132	71859	$0.9439 \pm 0.005$

Table 4.5: ZDC trigger efficiencies for ZDC reconstruction method 1 and 2

## 4.7 Systematic checks

Table 4.6 shows the systematic errors that were estimated. The method used to separate the coherent from the photon-photon process is the most dominant error. The ZDC reconstruction method used to estimate the neutron thresholds is the next most dominant, followed by the method used to estimate the HF noise threshold.

systematic	uncertainty in %
Template fit normalized	+9.5% -12%
ZDC reconstruction	2.9%
ZDC trigger efficiency	2.2%
HF noise threshold	+1.3% -3.4%
MC acceptance	1.1%
Total systematic	8.1%

Table 4.6: Summary of systematic uncertainties

### 4.7.1 HF noise threshold

The way in which the HF noise distribution is measured effects the event selection and therefore the final candidate yeild. This cut plays a significant role in rejecting hadronic events. In Table 4.4 the importance of cutting on HF noise is evident. The HF noise cut rejects a little less than 1/5 of the remaining events. The systematic uncertainties on the HF noise requirement is important for this reason. The result must not depend significantly on the method used to apply the cut on the noise because of the large reduction of events that result from it.

Four different approaches were employed to estimate the systematic effect arising from picking



a particular method for setting the HF noise threshold. By looking at the variation of the number of events that remain after applying the thresholds derived from these four methods, the systematic uncertainty for the HF noise cut was estimated. The four methods are derived from combinations of two variations. The type of object was varied from a low-level detector object called a RecHit to a higher level physics object called a CaloTower. The RecHit is the energy deposited in a single calorimeter detector element, whereas the CaloTower is a collection of RecHits with various thresholds, which represent a full energy deposit that would come from a particle or a collection of particles from a jet passing through the detector. The second variation is on the separation of the two sides. In one case the threshold is derived for the two sides combined. In another case the thresholds are calculated separately for the two sides of HF. By combining these two variations, a total of four estimates of the effect of the HF noise cut were made. Table 4.7 below shows the thresholds that are measured for each of the four methods. The resulting yields from the four different methods are displayed in Table 4.8.

Object type	HF (GeV)	HF <sup>-</sup> (GeV)	HF <sup>+</sup> (GeV)
RecHits	3.85	3.25	3.45
CaloTowers	4.25	3.25	3.75

Table 4.7: HF noise thresholds for various noise measurement methods.

Object type	Combined HF threshold	Two-sided thresholds
RecHits	298	290
CaloTowers	302	288

Table 4.8: Candidate yields below 1.05 GeV  $p_T$  for various HF noise cuts.

The threshold was adjusted to estimate the effect of tightening the requirement on the zero bias data. By successively lowering the percentage of the zero bias sample that was included, the HF noise cut was made more restrictive including first 98%, then 97% of all zero bias events. This was done for both object types, RecHits and CaloTowers. This allows for an estimate of the systematic uncertainty on selecting a 99% cut. Table 4.9 shows the effect on the thresholds themselves for both RecHits and CaloTowers, whereas Table 4.10 shows the effect on the candidate yields.

Table 4.9: Values of the energy cuts for the HF calorimeter for RecHit and CaloTower in GeV.

%	$E_{RecHit}$ GeV	$E_{CaloTower}$ GeV
99	3.85	4.25
98	3.25	3.75
97	2.95	3.25

Table 4.10: Number of dimuon candidates with  $p_T < 1.05$  when changing HF calorimeter cuts for RecHit and CaloTower.

%	RecHit cut	CaloTower cut
99	298	302
98	287	294
97	284	280

The systematic uncertainty in the HF noise threshold measurement was calculated taking the difference from the 99% combined RecHit method with the upper and lower extrema. The systematic uncertainty from this method is calculated to be +1.3% -3.4%.

## 4.7.2 Template fit normalization

The  $p_T$  template fit depends on the functions chosen for the fit to the mass distribution. As described in Section 4.5, the similarity of the of the  $p_T$  distribution for the coherent and photon-photon process make the contributions from the two process difficult to separate from the  $p_T$  distribution alone. The mass distribution was used to distinguish between these two processes. In turn, the  $p_T$  becomes dependent on the mass fit.

The systematic uncertainty due to the choose of functions used to fit the mass distribution was estimated by varying the signal and background functions. The contribution to the background from the mass fit was used to fix the contribution from the photon-photon process in the  $p_T$  template fit. Two functions were used to describe the signal, a Gaussian, and a Crystal ball function. The background was fit to a linear function, a 2nd order polynomial, and a 2nd order Cheby-Chev polynomial. The resulting variation on the coherent contribution was used to as an estimate of this systematic effect.

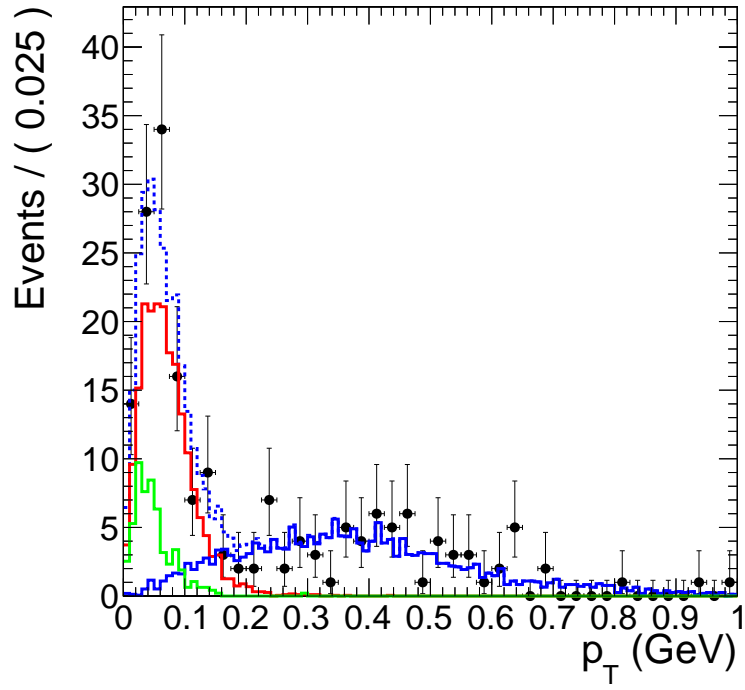


Figure 4.19: Coherent, incoherent, and photon-photon process  $p_T$  template fit to data.

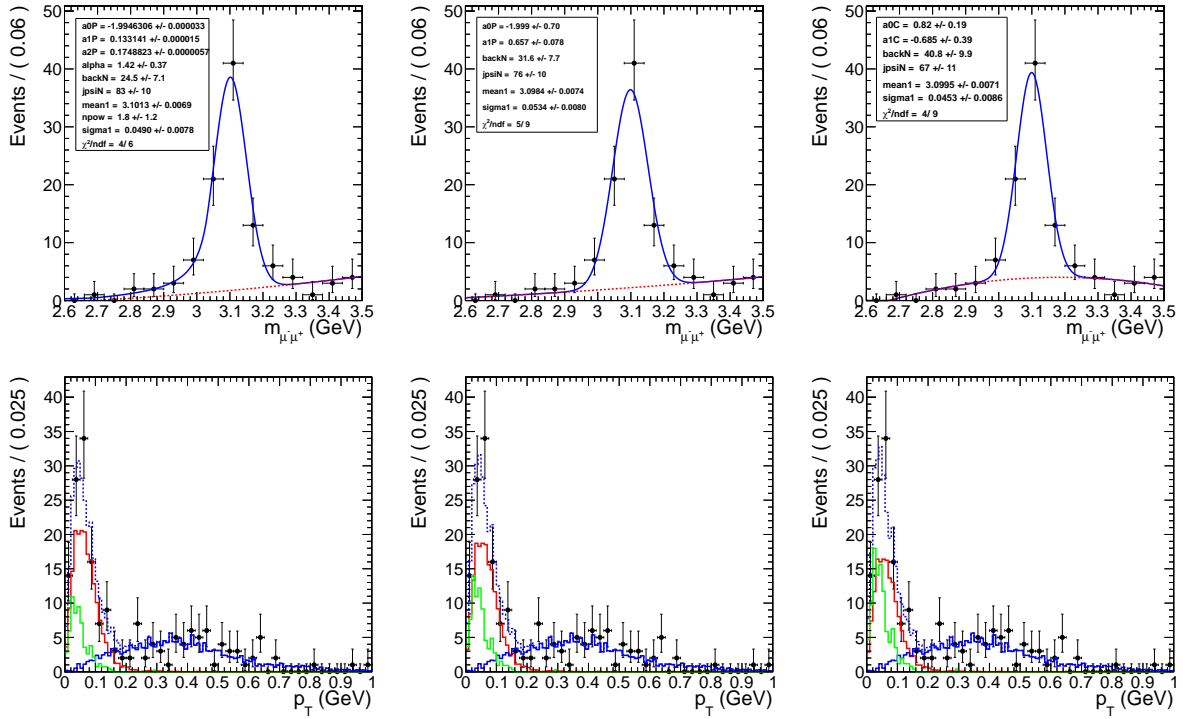


Figure 4.20: Various mass distribution fits and the corresponding  $p_T$  template fit.

Moving from left to right in Fig 4.20, the contribution from the photon process increases. The  $\chi^2$  pre degree of freedom is similar between the three fits indicating a similar goodness of fit. On this basis, neither fit is preferred. The left most fit uses a Crystal Ball function to account for the radiative decay of the final state daughters of the  $J/\psi$ . The low mass exponential portion however picks up background events and overestimates the  $J/\psi$  contribution. The right most plot fits the background to a 2nd order Cheby-Chev polynomial. Because the Cheby-Chev peaks just below the  $J/\psi$  peak, this fit overestimates the background and in turn underestimates the signal contribution. The Gaussian fit with a linear background however does a reasonable job of fitting both the background and the signal.

From these three fits an upper and lower bound of the systematics due the choice of fit functions was estimated. The difference between the Gaussian-Linear fit and the Crystal Ball-polynomial fit was taken as an upper bound. The difference between the Gaussian-Linear fit and the Gaussian-Cheby-Chev fit was taken as a lower bound. The overall systematic uncertainty due to the choose of mass fit functions is found to be +9.5% -12%.

### 4.7.3 Mass fit

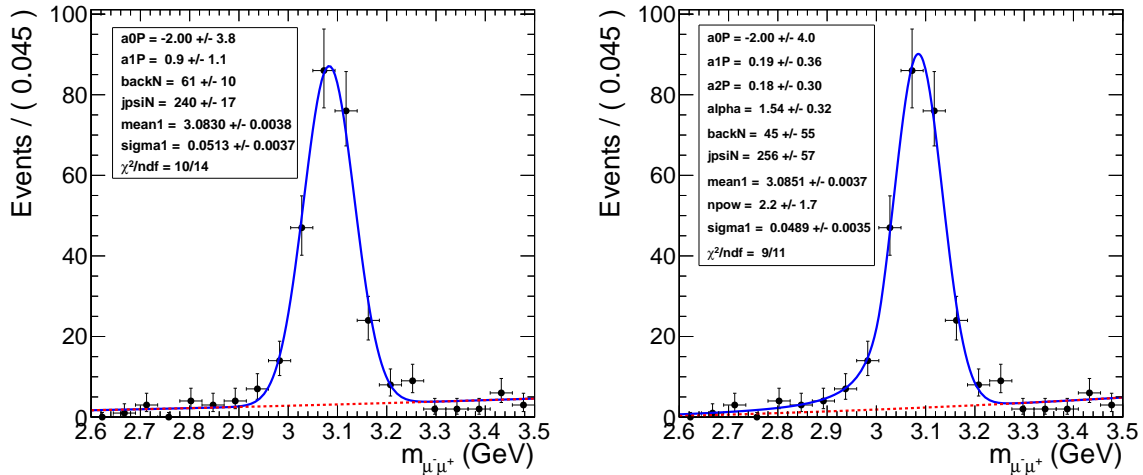


Figure 4.21: Mass fit to  $J/\psi$  using Gaussian (Left) and Crystal Ball (Right) for the signal and a polynomial for the background

Fig. 4.21 demonstrates the small dependence the raw  $J/\psi$  yield has on the fitting function.

Both fit functions agree well, with reduced  $\chi^2$  values below one. The Crystal ball fit give an upper estimate for the  $J/\psi$  yield. The Gaussian fit gives an lower estimate. The main difference comes from the lower mass tails. In the Crystal ball fit the lower tail is considered to be signal due to shifting of the mass spectrum to lower mass due to radiation from the final state muons. In the Gaussian fit the lower mass tail is considered to be background and the signal is sharper.

As check on the simultaneous  $p_T$  and mass fit, the mass fit is done using mass templates from STARlight.

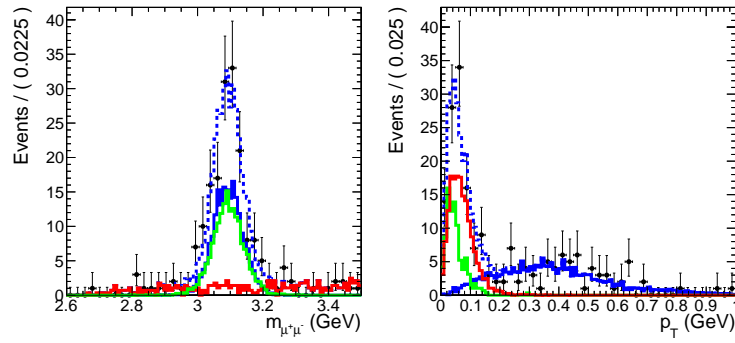


Figure 4.22: Simultaneous fit to the mass and  $p_T$  using mass templates for the mass fit.

#### 4.7.4 MC acceptance

The MC derived acceptance correction factors depend on the input physics generator. The underlying  $p_T$  distribution was assumed to be correctly described by STARlight for the coherent cross section measurement. To estimate the effect of changing the underlying  $p_T$  distribution on the acceptance measured from the MC, the incoherent sample was used to correct the coherent yield. By using the broader  $p_T$  distribution of the incoherent process, an estimate of acceptance measurements dependence on the assumed shape of the  $p_T$  distribution was obtained. The systematic uncertainty due to the dependence of the acceptance correction on the  $p_T$  distribution of the input physics generator was estimated by the difference between the correction factors from the coherent and incoherent MC samples. Half the difference was used as the estimate and was found to be 1.1%.

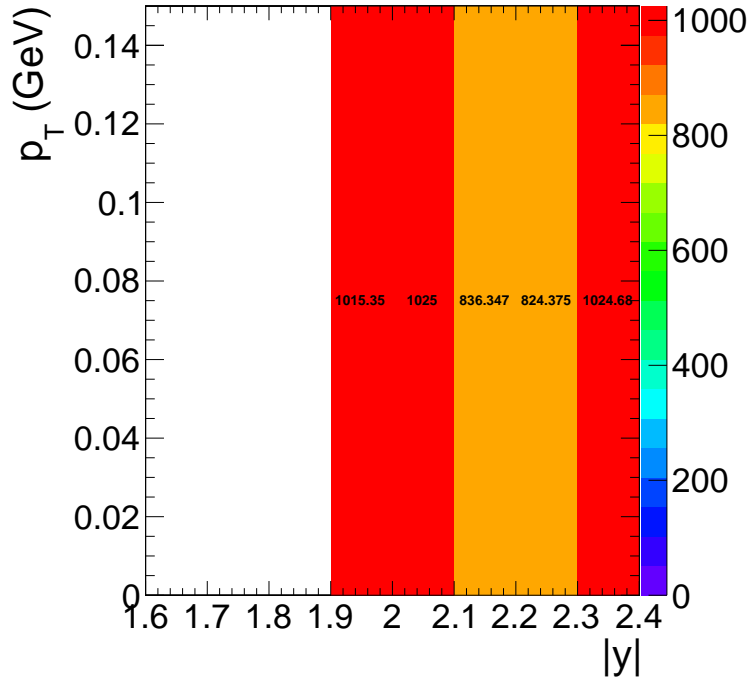


Figure 4.23: Yields corrected by the MC incoherent acceptance map.

The effect of polarization was estimated by correcting by the acceptance for an unpolarized  $J/\psi$  sample.

#### 4.7.5 ZDC reconstruction

An additional method for estimating the ZDC neutron thresholds was used to estimate the systematic errors on the threshold measurements. This additional method, used in previous ZDC measurements, differs in the way the signal time slices are used to calculate the signal from each channel. In the standard method, the signal is taken from the sum of time slices 4, 5, and 6. To estimate the event by event noise pedestal the sum of time slice 1 and 2 are used. The signal for an individual ZDC channel is then calculated as the sum of the signal time slices minus the sum of the noise time slices weighted by a factor of 3/2 to account for the differing number of noise versus signal time slices. The advantage of the standard method is that by using multiple signal and noise time slices the signal and noise are effectively averaged reducing time slice to time slice fluctuations. However, by using time slices 1 and 2 for measuring the noise, the noise can only be

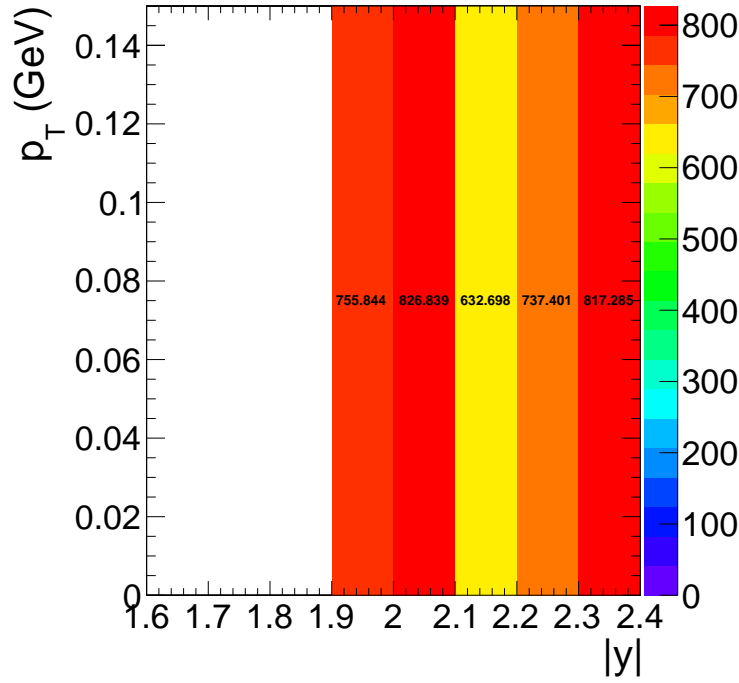


Figure 4.24: Yields corrected by an unpolarized  $J/\psi$  sample.

measured half the time due to unmeasurable negative fluctuations of the dominant low frequency component of the noise.

As in the new method described in Section 4.4, the standard method combines the channels to create a signal measurement from the whole of each side of the ZDC, one measurement for  $ZDC^+$ , and one for  $ZDC^-$ . The noise subtracted signal from each of the HAD channels are added together. Then the EM section channels are summed. The EM section is weighted by a factor of 0.1 as in the new method. After the weighting the EM and HAD channels are added to each to create one measurement for  $ZDC^+$  and another measurement for  $ZDC^-$ .

Fig. 4.25 shows the spectra for  $ZDC^+$  and  $ZDC^-$  using the standard method. The same fit used for the new method is applied to standard method. As in the new method, the single neutron threshold is set to  $2\sigma$  below the mean from the fit to the one neutron peak. The multi-neutron threshold was set to  $2\sigma$  above the one neutron peak.

The systematic uncertainty due to the ZDC reconstruction method are estimated from the difference between the UPC  $J/\psi$  candidate yields. Both the reconstruction method and thresholds

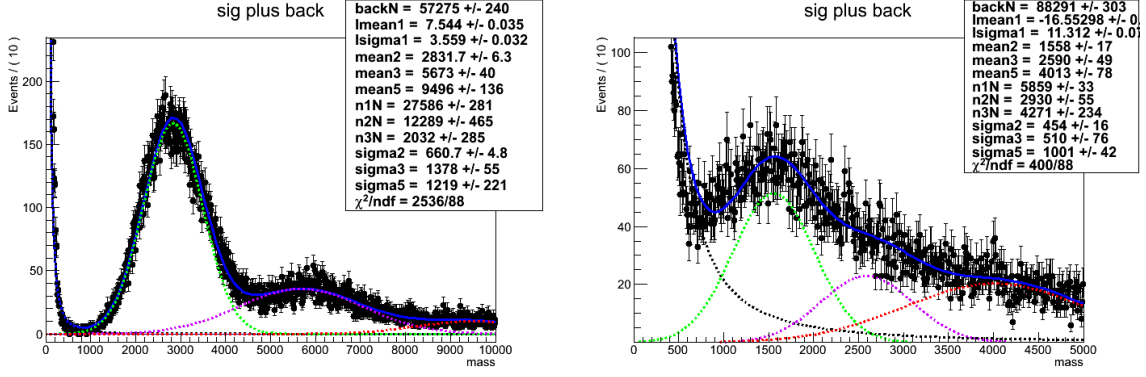


Figure 4.25: Fit to charge spectrum from ZDC<sup>-</sup> (left) and ZDC<sup>+</sup> (right) using the standard reconstruction method

were changed to calculate the effect of the reconstruction method. The yields for the new and standard ZDC reconstruction method in the Xn0n break up were found to be 298 and 315 respectively. Half the difference between the two methods was used as an estimated of the systematic uncertainty. The systematic uncertainty due to the ZDC reconstruction method was found to be 2.9%.

#### 4.7.6 ZDC trigger efficiency

The ZDC trigger efficiency measurement is sensitive to the underlying neutron distribution. The more neutrons that high the ZDC the higher the trigger efficiency will be. To estimate the effect the input sample has on the efficiency, the ZDC trigger efficiency was measured from five different samples. The Table 4.11 shows the results from the five samples. Both the new and standard ZDC reconstruction methods are shown for comparison.

The amount of electronic noise in the sample also effects the measurement. The more noise sits below the one neutron peak, the worse the efficiency is. In Table 4.11, the Zero Bias sample compared the Zero Bias sample with the timing cuts the described in the previous section shows a significant increase in efficiency in the sample with reduced noise. The same increase is seen when comparing the ZDC triggered sample with the ZDC triggered sample that also requires a pixel track. The effect of the electronic noise is also present in the difference seen in using the



ZDC Side	Reco Method	$N_{events}$	$N_{trig}$	$\epsilon_{ZDC}$
(ZDC <sup>+</sup> or ZDC <sup>-</sup> ) and 1 pixel track				
ZDC <sup>-</sup>	1	72946	71688	$0.982 \pm 0.005$
ZDC <sup>-</sup>	2	73028	71706	$0.9819 \pm 0.005$
ZDC <sup>+</sup>	1	76137	71786	$0.9429 \pm 0.005$
ZDC <sup>+</sup>	2	76132	71859	$0.9439 \pm 0.005$
(ZDC <sup>-</sup> or ZDC <sup>+</sup> ), 1 pixel track, and L1 EG trigger				
ZDC <sup>-</sup>	1	613758	602123	$0.9810 \pm 0.0018$
ZDC <sup>-</sup>	2	614014	601863	$0.9802 \pm 0.0018$
ZDC <sup>+</sup>	1	643905	602671	$0.9360 \pm 0.0017$
ZDC <sup>+</sup>	2	647888	603089	$0.9309 \pm 0.0017$
(ZDC <sup>-</sup> or ZDC <sup>+</sup> ), 1 pixel track, and L1 Muon trigger				
ZDC <sup>-</sup>	1	65466	63376	$0.9681 \pm 0.0054$
ZDC <sup>-</sup>	2	65543	63358	$0.9667 \pm 0.0054$
ZDC <sup>+</sup>	1	71929	63512	$0.8830 \pm 0.0048$
ZDC <sup>+</sup>	2	72932	63582	$0.8718 \pm 0.0047$
Zero Bias with ZDC timing cuts				
ZDC <sup>-</sup>	1	88676	84429	$0.9521 \pm 0.0046$
ZDC <sup>-</sup>	2	88480	84202	$0.9517 \pm 0.0046$
ZDC <sup>+</sup>	1	59878	54728	$0.9140 \pm 0.0054$
ZDC <sup>+</sup>	2	60467	54733	$0.9052 \pm 0.0053$
(ZDC <sup>-</sup> or ZDC <sup>+</sup> )				
ZDC <sup>-</sup>	1	30986	30333	$0.9789 \pm 0.0079$
ZDC <sup>-</sup>	2	31029	30339	$0.9778 \pm 0.0079$
ZDC <sup>+</sup>	1	39178	30164	$0.7699 \pm 0.0059$
ZDC <sup>+</sup>	2	35703	30443	$0.8527 \pm 0.0067$
Zero Bias				
ZDC <sup>-</sup>	1	109967	101598	$0.9239 \pm 0.0040$
ZDC <sup>-</sup>	2	110230	101561	$0.9214 \pm 0.0040$
ZDC <sup>+</sup>	1	253241	86660	$0.3422 \pm 0.0013$
ZDC <sup>+</sup>	2	156336	87401	$0.5591 \pm 0.0024$

Table 4.11: ZDC trigger efficiencies for ZDC reconstruction method 1 and 2 for different trigger samples

two methods. As seen in Fig. 4.26, the new reconstruction method shows better separation of the one neutron peak from the electronic noise, in particular in  $ZDC^+$  where the signal gain is lower. For this reason, the Zero Bias data, which contains that largest contribution from electronic noise, shows the most separation between the two methods and give the lowest estimate for the ZDC trigger efficiency.

The systematic uncertainty due to the uncertainty in the underlying distribution was estimated by calculating the standard deviation of the least extreme values from Table 4.11. Any value greater than three standard deviations from the mean was thrown out.

#### 4.7.7 ZDC reconstruction method comparison

The new method relative to the standard method separates low signal from the noise more effectively for both sides of the ZDC. This is particularly important for  $ZDC^+$  where the 1st HAD section had a lower gain than the other sections. The  $ZDC^+$  and  $ZDC^-$  signals near the one neutron peak using the standard and new reconstruction methods were plotted for comparison in Fig. 4.26. In Fig. 4.26, the shrinking of width of the noise peak around zero in the new method versus the old

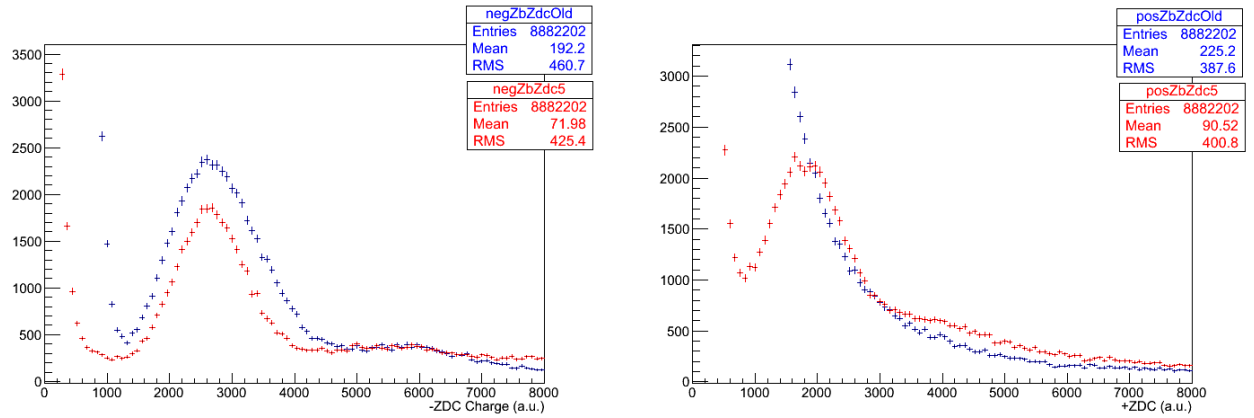


Figure 4.26: Comparison of the **new** ZDC reconstruction method and the **standard** method for  $ZDC^-$  (left) and  $ZDC^+$  (right).

method is apparent for both  $ZDC^+$  and  $ZDC^-$ . For the standard method no single neutron peak is resolved in  $ZDC^+$ , whereas the single neutron peak is resolved using the new method.

Timing cuts were applied to enhance the signal relative to the background in order to resolve

the one neutron peak in  $ZDC^+$  using the standard method. Because the products of the collision are synced with time slice 4, noise can be rejected by selecting channels where the maximum signal falls into time slice 4. The noise will have no preferred time slice (see Fig. 4.4). Using this fact, signal can be preferably selected by requiring that the hadronic channels of the ZDC have a peak signal in the fourth time slice. Through these timing cuts the single neutron peak was recovered using the standard reconstruction for  $ZDC^+$ .

To examine the effectiveness of the timing cuts, event by event noise subtraction was removed from the standard reconstruction. The signal from each channel was taken from time slices 4,5, and 6 with out subtracting 1 and 2. The signal spectrum from  $ZDC^-$  was then plotted with the result shown in Fig. 4.27. As each additional hadronic channel is required to have a maximum

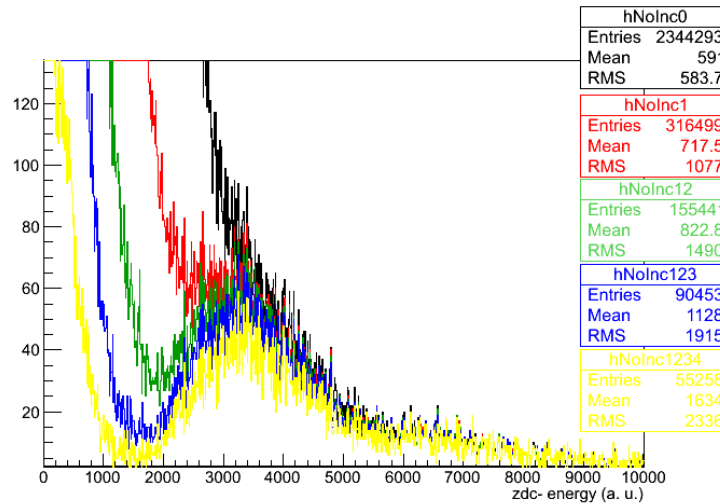


Figure 4.27: Effects of requiring in-time signal in successively more ZDC hadronic channels, no timing, at least **one**, at least **two**, at least **three**, and all **four** HAD channels have a maximum signal in the fourth time slice.

signal in the fourth time slice, the single neutron peak emerges. Fig. 4.27 demonstrates that the single neutron peak can be recovered from the noise using timing cuts alone.

Using the standard noise subtraction method, the same signal that emerges from the timing cuts alone appear without timing cuts. Fig. 4.28 confirms that both noise subtraction and the timing requirement produce the same signal. This gives confidence that the signal is not an artifact of either cut, but the true neutron signal.

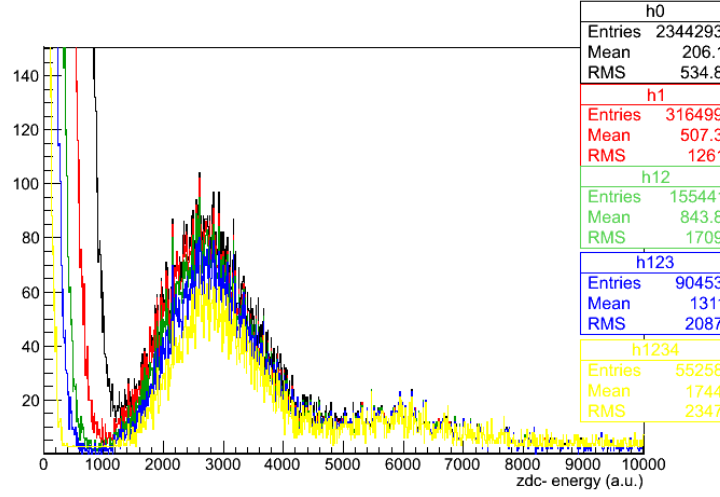


Figure 4.28: Effect of ZDC signal timing requirements after noise subtraction.

Fig. 4.28 and Fig. 4.26 demonstrate the consistence of the using timing cuts and noise subtraction to enhance the signal neutron peak. Fig. 4.28 confirms the legitimacy of the timing requirement method in  $ZDC^-$  by showing the that the same signal emerges from the noise subtraction method as the timing method. Fig. 4.26 demonstrates the corresponds between the new noise subtraction method and the standard method on in  $ZDC^-$  where signal is better separated from the electronic noise. This allows for confidence that the signal seen in  $ZDC^+$  using the new method is the one neutron peak.

#### 4.7.8 Tag and probe

The main purpose for fitting the mass spectra to estimate the efficiency is to separate the background from true signal. The background may not have the same efficiency as the signal, so separating the two is important if this is the case. In the tag and probe fit the signal peak from the  $J/\psi$  resonance is fit to the probes, passing probes, and failing probes alike (see Fig. 4.15). The signal shape, if from the same physical signal, will be identical in each of the three distributions. The background is for the passing and failing probes is fit using different parameters for the background because the background may come from different physical processes than the signal or non-physical sources like combinatorial backgrounds or misidentified fake particles. When

the background comes from sources other than the physical signal, the background may give an efficiency estimate that is lower than the signal.

The trigger efficiency measured by the tag and probe method depend on the fitting functions use to estimate the background and signal contributions. Depending on what functions is used to fit the spectra, the amount of amount of background can be over or underestimated and effect the efficiency measurement. To estimate this effect, the tag and probe efficiencies were additionally measured by counting probes in the  $J/\psi$  mass window. The whole mass window is used to estimate the efficiency including all the events from the mass side bands. In this way, a worst case scenario estimate is given where all background events are included as signal.

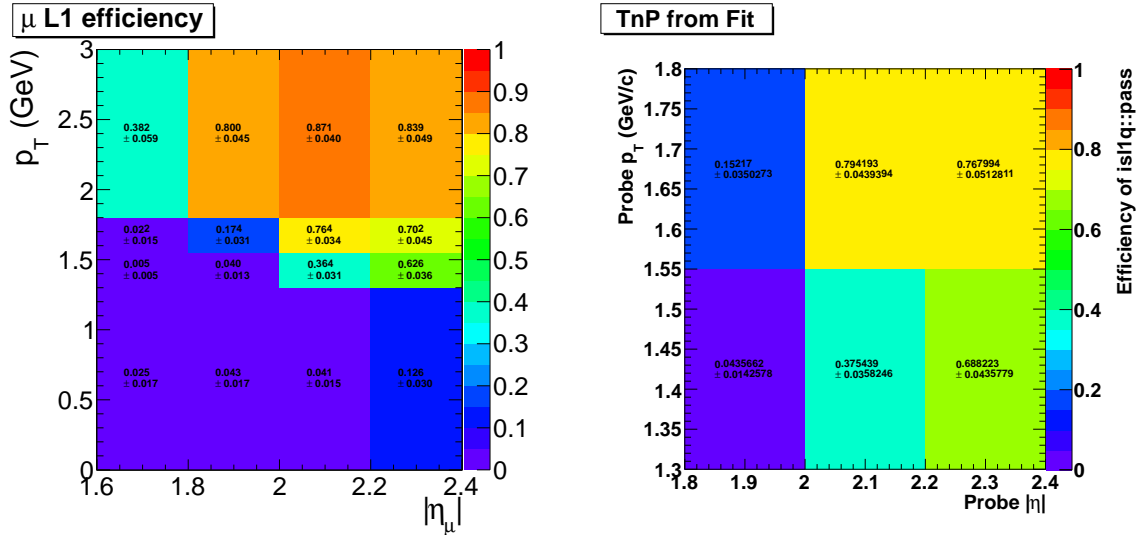


Figure 4.29: Tag and probe trigger efficiencies from counting (left) compared to fitting (right)

From Fig. 4.29 it is apparent that the choice of fit function and therefore the amount of background from the mass side bands is included in the signal measurement has very little effect on the tag and probe efficiency measurement. The small effect of including the side bands is due to the side bands being comprised mostly of photon-photon events. Because this background is neither decays from other particles like pions nor is it non-physical background like combinatorics, the efficiency for muons from the sidebands are nearly identical to  $J/\psi$  signal. The photon-photon process directly produces two muons just like the  $J/\psi$ , therefore efficiency estimated from the side bands has little effect on the measurement because of this similarity. The counting and fitting trig-

ger efficiency measurements agree within statistical uncertainties, so this uncertainty was taken to be negligible.

#### 4.7.9 MC vs Data compairson

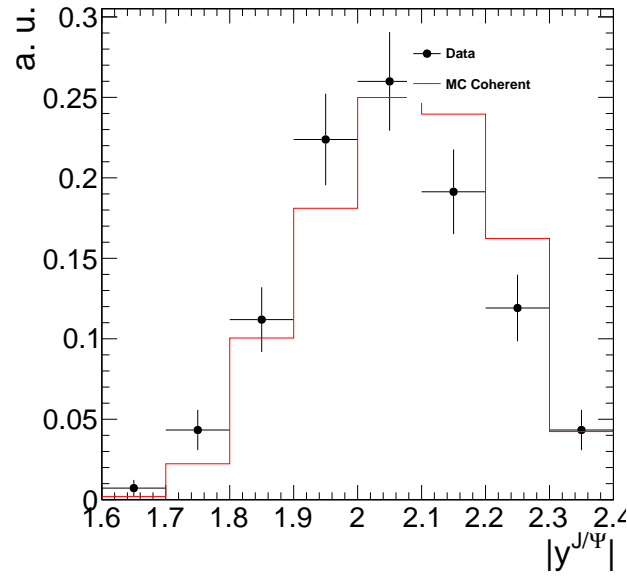


Figure 4.30: Comparison of the of the dimuon rapidity distributions between coherent MC sample and Data.

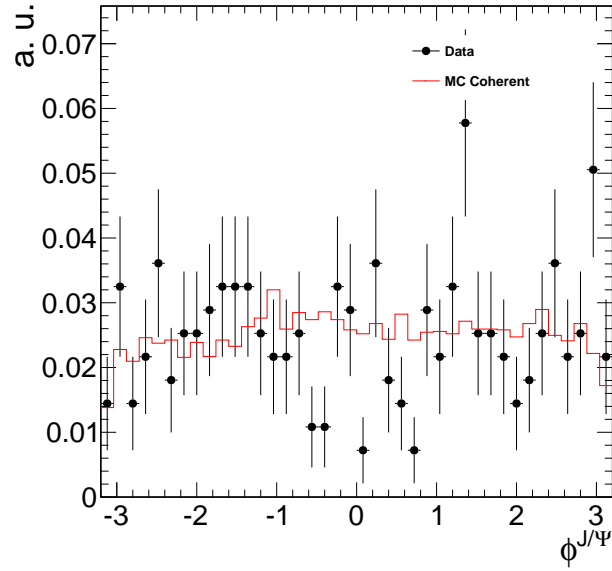


Figure 4.31: Comparison of the of the dimuon  $\phi$  distributions between coherent MC sample and Data.

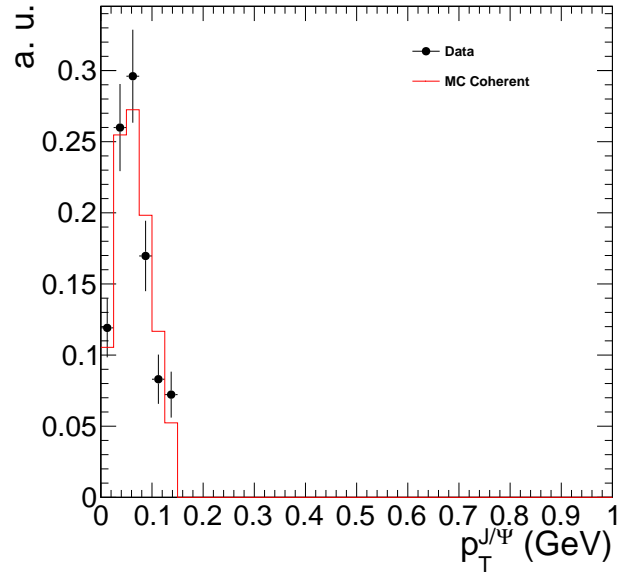


Figure 4.32: Comparison of the of the dimuon  $p_T$  distributions between coherent MC sample and Data.

# Chapter 5

## Results

The main results of this thesis are give here: the cross section for coherent  $J/\psi$  production, the incoherent  $J/\psi$  cross section, the cross section for muon pairs from photon-photon interactions, the ratio between break up mode yields, and the rapidity correlations between dimuon candidates and neutrons in the ZDC.

### 5.1 Coherent cross section

The coherent cross section in calculated from the following equation:

$$\frac{d\sigma_{co}^{J/\psi}}{dy} = \frac{N_{cor} f_{co}}{\Delta y \mathcal{L}_{int} \epsilon_{ZDC} \epsilon_{p_T} BR_{\mu^+\mu^-}} \quad (5.1)$$

where  $N_{cor}$  is corrected dimuon yield,  $f_{co}$  is the fraction of events that come from the coherent process,  $BR_{\mu^+\mu^-}$  is the branching ratio for  $J/\psi$  to  $\mu^+\mu^-$ ,  $\epsilon_{ZDC}$  is the efficiency for triggering the ZDC,  $\epsilon_{p_T}$  is the efficiency for the 0.15 GeV cut in  $p_T$ ,  $\mathcal{L}_{int}$  is the integrated luminosity, and  $\Delta y$  is the width the rapidity interval.

The raw yield of dimuon candidates was measured after applying the cuts described in Section 4.3.  $N_{cor}$  was calculated by dividing the raw yields from Fig. 5.1 by the acceptance and efficiency factor from Fig. 4.18, which combines  $A$  and  $\epsilon_{trigger}^{dimuon}$  as described in Section. 4.6. The



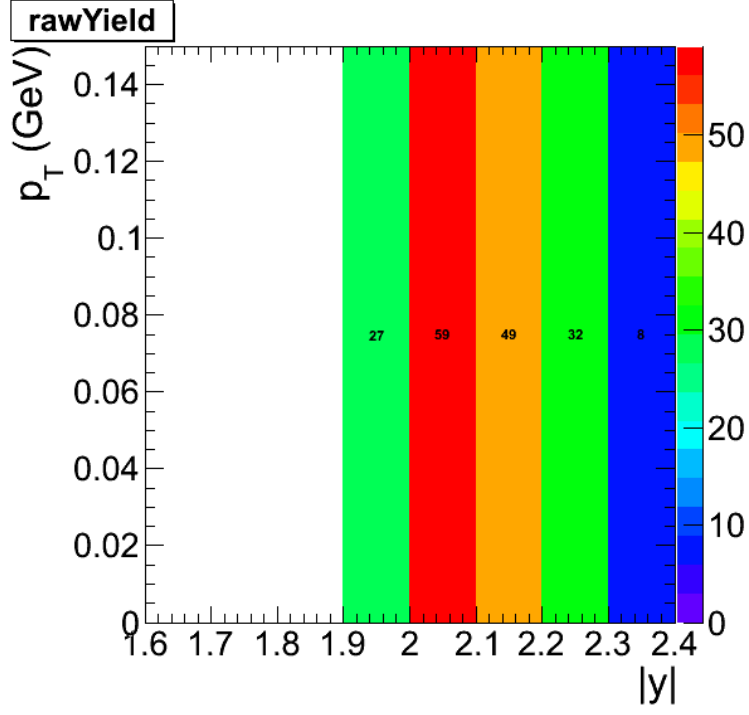


Figure 5.1: Raw yield for the Coherent cross section measurement.

corrected yields,  $N_{cor}$ , are shown in Fig. 5.2. For the coherent cross section measurement,  $N_{cor}$

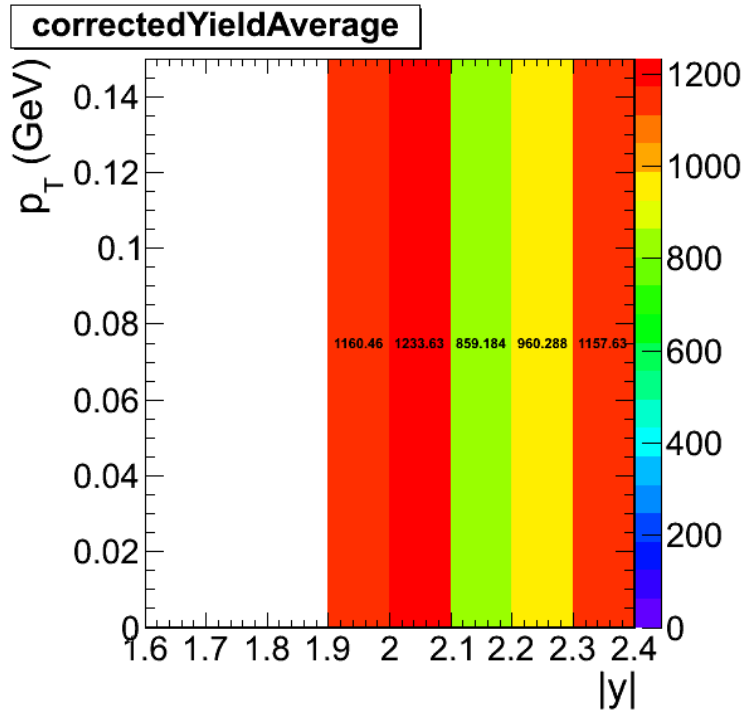


Figure 5.2: Corrected yields for the coherent  $p_T$  region.

is taken from the region  $2.0 < |y| < 2.2$  and  $p_T < 0.15$  GeV to avoid the edges of the detectors acceptance, bin migration in the calculation of  $A$ , and overlap between the coherent and incoherent process. From this procedure, the  $N_{cor}$  was measured to be 1903.

To measure  $f_{co}$ , the simultaneous fit shown in Fig. 4.11 was used. The normalizations for each of the three components to the signal are fixed by the fit as described in Section 4.5. The normalized coherent template is integrated up to 0.15 GeV in  $p_T$  and divided by the integral of the data  $p_T$  spectrum up to 0.15 GeV. The statistical error taken from the fit,  $f_{co} = 0.60 \pm 0.11$ .

The two efficiency terms,  $\epsilon_{ZDC}$  and  $\epsilon_{p_T}$ , were measured from data and MC respectively. As described in Section 4.4,  $\epsilon_{ZDC}$  was measured in the from the ZDC triggered data set by dividing the number of events both fire the ZDC trigger and pass the one neutron threshold.  $\epsilon_{ZDC}$  was measured to be 0.96 with a negligible statistical error. The efficiency of the 0.15 GeV  $p_T$  cut was estimated from MC by dividing the number of events that are lost by applying the  $p_T$  cut after all other cuts are applied. From this method  $\epsilon_{p_T} = 0.95$ .

The remaining two terms,  $\mathcal{L}_{int}$  and  $BR_{\mu^+\mu^-}$ , depend on Ref. [15] and Ref. [17]. Ref. [15] describes the method of using activity in HF to measure the luminosity. From this method,  $\mathcal{L}_{int}$  was measured to be  $143.3\mu b^{-1} \pm 7.2$ .  $BR_{\mu^+\mu^-}$  from Ref. [17] is  $0.0593 \pm 0.0006$ . From Equation 5.1,  $\frac{d\sigma_{co}^{J/\psi}}{dy} = 368$  mb.

## 5.2 Incoherent cross section

The same basic procedure for measuring the coherent cross section was used to calculate the incoherent cross section.

## 5.3 Break up ratios

In Table 5.2 the ratio between raw yields for different break up modes are shown.

Fig. 5.3 and Fig. 5.4 compare the raw break up ratios two STARlight and LTA predictions.

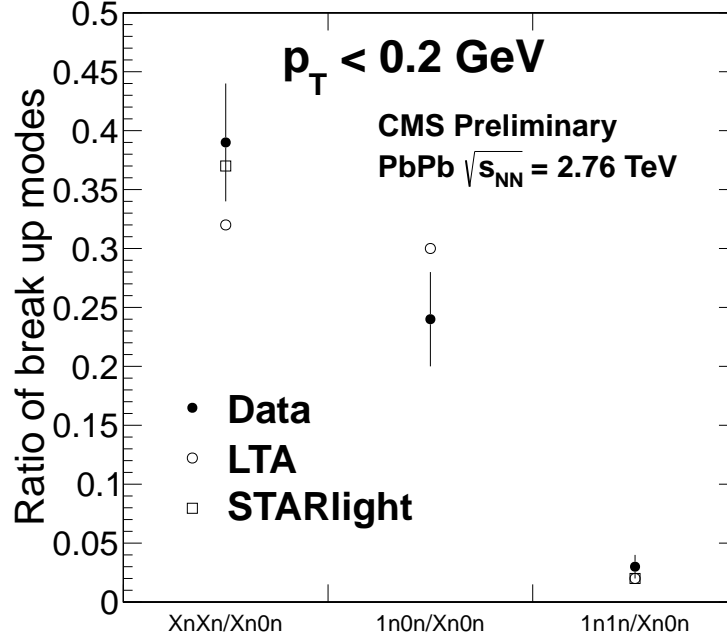


Figure 5.3: Ratio between  $J/\psi$  yeilds  $X_n X_n$  and  $1_n 0_n$  break-up modes compared the  $X_n 0_n$  break-up mode for  $J/\psi$  with  $p_T$  below 150 MeV.

The number of the coherent and incoherent  $J/\psi$  for each break-up mode are given in the Tab. 5.1. The ratios between the modes  $X_n X_n$ ,  $1_n 0_n$ ,  $1_n 1_n$  and the mode  $X_n 0_n$  are given in the table Tab. 5.2. Some of the ratios can be obtained from STARLIGHT and from the Zhalov and thus are given in Tab. 5.3.

	$X_n 0_n$	$X_n X_n$	$1_n 0_n$	$1_n 1_n$
coherent $J/\psi$	$242 \pm 16$	$94 \pm 10$	$58 \pm 8$	$8 \pm 3$
incoherent $J/\psi$	$291 \pm 17$	$57 \pm 8$	$19 \pm 4$	$2 \pm 1$

Table 5.1: Number of coherent  $J/\psi$  integrated over  $p_T$  and  $y$  with statistical uncertainty.

In Table 5.3 the ratio between break up modes are shown for different theories and processes.

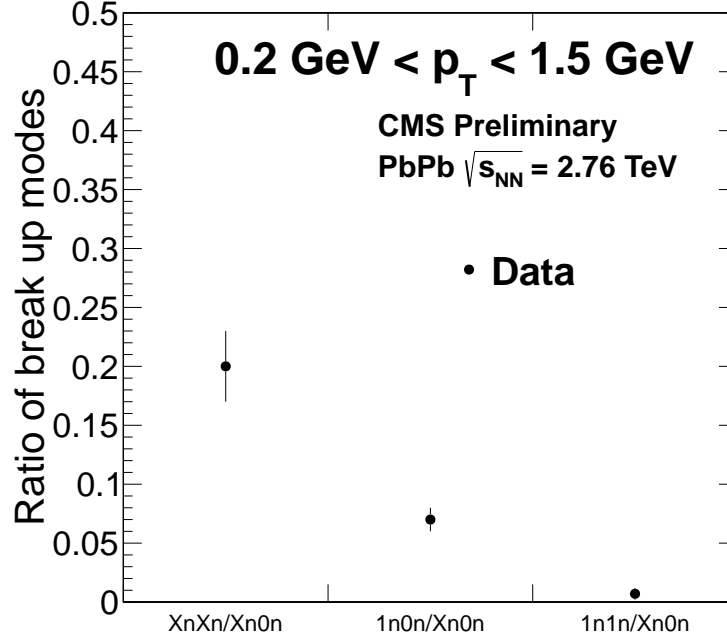


Figure 5.4: Ratio between  $J/\psi$  yeilds  $X_n X_n$  and  $1_n 0_n$  break-up modes compared the  $X_n 0_n$  break-up mode for  $J/\psi$  with  $0.2 < p_T < 1.5$  GeV.

	$X_n X_n / X_n 0_n$	$1_n 0_n / X_n 0_n$	$1_n 1_n / X_n 0_n$
coherent $J/\psi$	$0.39 \pm 0.05$	$0.24 \pm 0.04$	$0.03 \pm 0.01$
incoherent $J/\psi$	$0.20 \pm 0.03$	$0.07 \pm 0.02$	$0.007 \pm 0.005$

Table 5.2: Number of coherent  $J/\psi$  integrated over  $p_T$  and  $y$  with statistical uncertainty.

## 5.4 diMuon-neutron correlations

In this section the correlation between the rapidity of the  $\mu^+ \mu^-$  and of the neutron is studied. The following samples are studied:

- $\gamma + A$  collisions in which two cases are considered
  - elastic coherent interaction: here photon interacts with entier nucleus coherently and produce  $J/\psi$ . Another photon is needed to cause the breakup and neutron emission. Those two photons are uncorrelated and thus we don't expect to observe the correlation between the rapidity of the neutron and the rapidity of the  $J/\psi$ . In the data sample this

	$X_n X_n / X_n 0_n$	$1_n 0_n / X_n 0_n$	$1_n 1_n / X_n 0_n$
STARlight coherent	0.37	-	0.02
Zhalov coherent	0.32	0.30	0.02
STARlight incoherent	0.37	-	$0.007 \pm 0.02$

Table 5.3: Number of  $J/\psi$  integrated over  $p_T$  and  $y$  with statistical uncertainty.

corresponds to the low- $p_T J/\psi$  ( $p_T < 0.15$  GeV).

- inelastic incoherent interaction: here a single high  $p_T$  photon interacting with nucleus produce the  $J/\psi$  and neutron. The correlation between the rapidity of the neutron and the rapidity of the  $J/\psi$  is expected. In the data sample this corresponds to the high- $p_T J/\psi$  ( $0.15 < p_T < 1.05$ ).
- $\gamma\gamma$  collisions: two photons collide and produce the  $\mu^+ \mu^-$  and the third photon is needed to excite one of the nucleons and produce neutron. Thus we don't expect to see the correlation between the rapidity of the neutron and the rapidity of the  $\mu^+ \mu^-$ . In the data sample this corresponds to the  $\mu^+ \mu^-$  with the invariant mass between 4 and 8 GeV.

In order to study the correlation in rapidity between the neutron and dimuon direction we below four quantities and give they values in Table 5.4.

- $y_{\mu\mu}^- \wedge y_n^-$ : number of  $\mu^+ \mu^-$  having  $y < 0$  and the neutron in  $ZDC^-$  ( $y < 0$ )
- $y_{\mu\mu}^- \wedge y_n^+$ : number of  $\mu^+ \mu^-$  having  $y < 0$  and the neutron in  $ZDC^+$  ( $y > 0$ )
- $y_{\mu\mu}^+ \wedge y_n^+$ : number of  $\mu^+ \mu^-$  having  $y > 0$  and the neutron in  $ZDC^+$  ( $y > 0$ )
- $y_{\mu\mu}^+ \wedge y_n^-$ : number of  $\mu^+ \mu^-$  having  $y > 0$  and the neutron in  $ZDC^-$  ( $y < 0$ )

The ratio  $R_{opp/same}$  is defined as:

$$R_{opp/same} = \frac{y_{\mu\mu}^- \wedge y_n^+ + y_{\mu\mu}^+ \wedge y_n^-}{y_{\mu\mu}^- \wedge y_n^- + y_{\mu\mu}^+ \wedge y_n^+} \quad (5.2)$$

Ratios studied in this section are only sensitive to the difference between the  $ZDC^-$  and  $ZDC^+$ . It is seen that the efficiency of both ZDCs is not exactly the same i.e. the efficiencies of  $ZDC^-$  and  $ZDC^+$  are respectively  $\epsilon_{ZDC^-}=0.98$  and  $\epsilon_{ZDC^+}=0.94$  and this is taken into account in the estimations. The  $R_{opp/same}$  ratio corrected by the ZDCs efficiencies is also included in Table 5.4 and called  $R_{opp/same}^{\epsilon_{ZDC}}$ . It is seen that the difference between corrected and uncorrected results is very small. Other uncertainties cancel. In this case cuts related to the acceptance and efficiencies corrections are not necessary and thus they are released.

Figure 5.5 gives  $p_T$  distributions of the  $J/\psi$  when  $J/\psi$  and neutron have the opposite rapidity direction or when they have the same rapidity direction for low- $p_T$  and high- $p_T$   $J/\psi$ . Also the Fig 5.5 gives the  $R_{opp/same}$  for low- $p_T$  and high- $p_T$   $J/\psi$ . It is seen from this plot that in the case of the low- $p_T$   $J/\psi$  this  $R_{opp/same}$  ratio is close to 1 and is decreasing when the  $p_T$  of  $J/\psi$  increases.

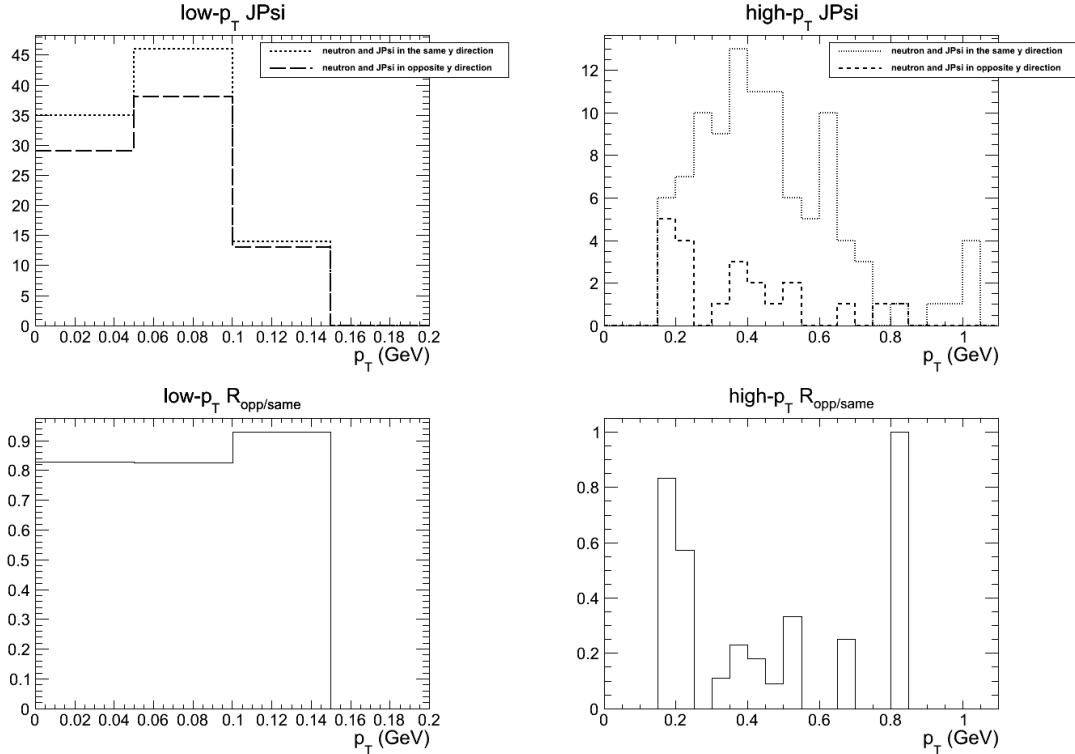


Figure 5.5: Transverse momentum distribution of the  $J/\psi$  when  $J/\psi$  and neutron have the opposite rapidity direction and the transverse momentum distribution of the  $J/\psi$  when  $J/\psi$  and neutron have the same rapidity direction for low- $p_T$  (top left) and high- $p_T$  (top right)  $J/\psi$ . Bottom: Ratios  $R_{opp/same}$  for low- $p_T$  (left) and high- $p_T$  (right)  $J/\psi$ .

Compiled for  $p_T < 1.05$  GeV  $R_{opp/same}$  ratio between the  $p_T$  distribution of the  $J/\psi$  having neutron emitted in the opposite direction and the  $J/\psi$  having the neutron emitted in the same direction is shown on Fig. 5.6. The same distributions as 5.5 but now as a function of rapidity of the  $J/\psi$  are

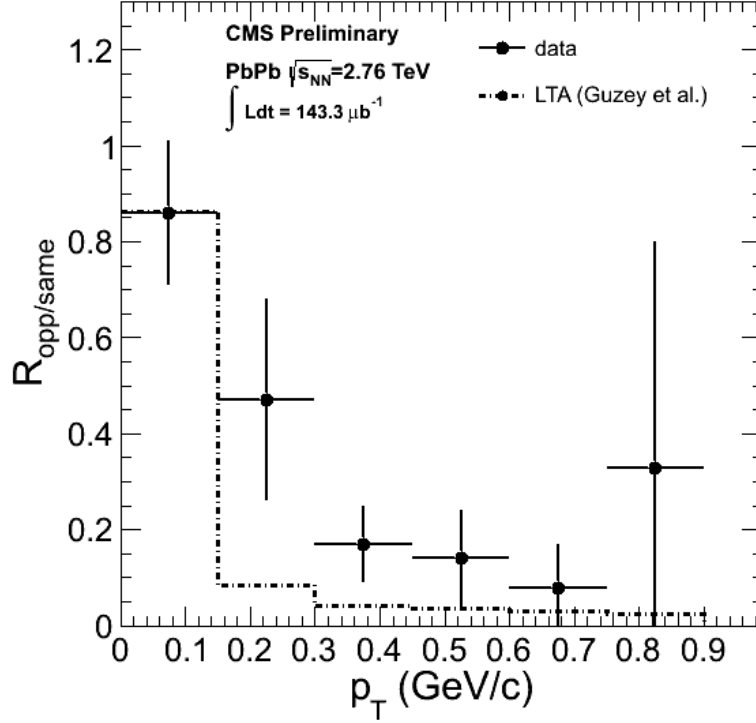


Figure 5.6: Ratio between the transverse momentum distribution of the  $J/\psi$  when  $J/\psi$  and neutron have the opposite direction and the transverse momentum distribution of the  $J/\psi$  when  $J/\psi$  and neutron have the same direction.

presented in the Fig 5.7 and compiled in Fig. 5.8.

Figure 5.9 shows the rapidity of the dimuon for the events that are tagged by the  $ZDC^+$  and  $ZDC^-$  means having the neutron emitted in the  $y > 0$  and  $y < 0$ .

Another, interesting correlation between the  $J/\psi$  rapidity direction and the neutron rapidity can be also studied with quantities defined in Eq. 5.3 that are calculated in the Table 5.4. Table 5.5 gives the same quantities as Table. 5.4 but here it is corrected for the difference between the efficiency of the  $ZDC^+$  and  $ZDC^-$ .

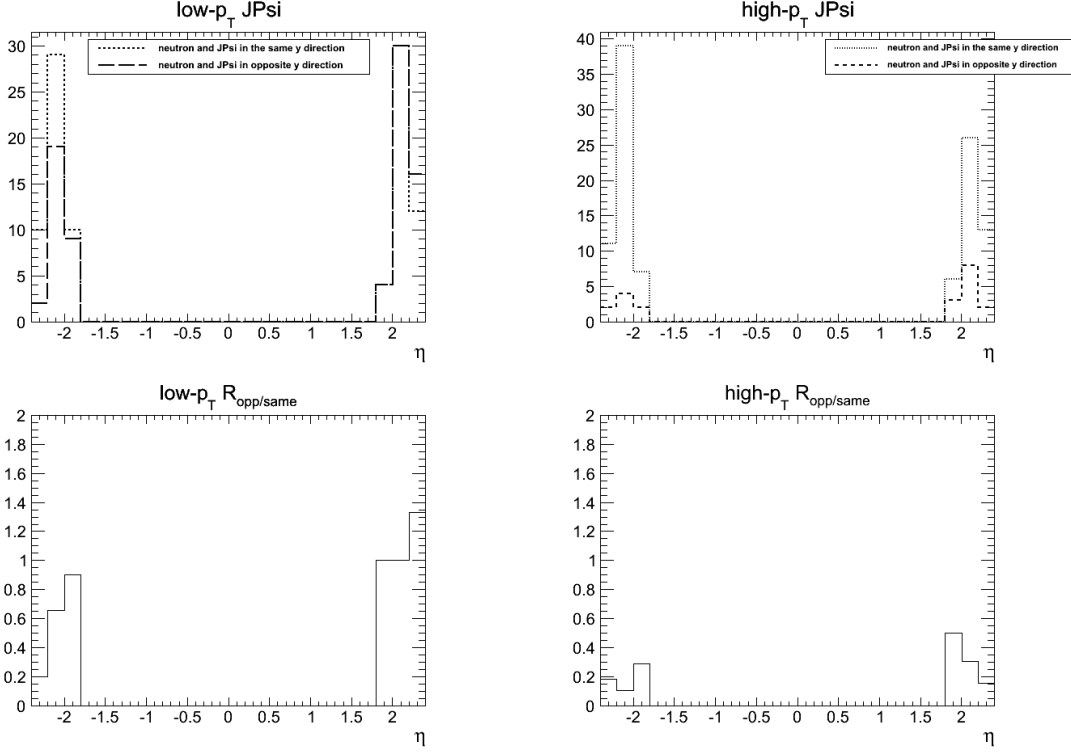


Figure 5.7: Rapidity distribution of the  $J/\psi$  when  $J/\psi$  and neutron have the opposite rapidity direction and the rapidity distribution of the  $J/\psi$  when  $J/\psi$  and neutron have the same rapidity direction for low- $p_T$ (top left) and high- $p_T$ (top right)  $J/\psi$ . Bottom: Ratios  $R_{opp/same}$  for low- $p_T$ ( left) and high- $p_T$ ( right)  $J/\psi$ .

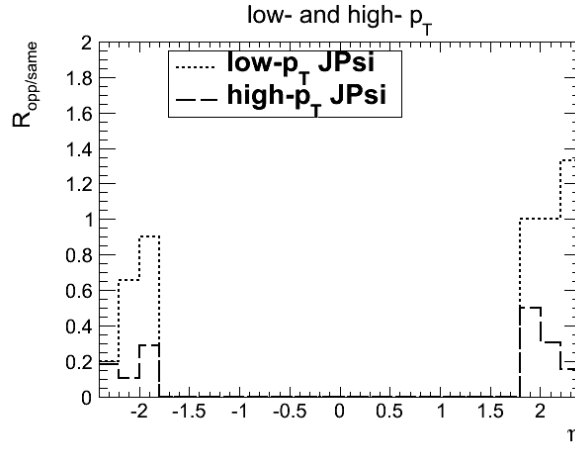


Figure 5.8: Rapidity ratios  $R_{opp/same}$  for low- $p_T$ ( left) and high- $p_T$ ( right)  $J/\psi$ .

$$R_{(\mu\mu)^-}^{n^-/n^+} = \frac{y_{\mu\mu}^- \wedge y_n^-}{y_{\mu\mu}^- \wedge y_n^+} \quad \text{and} \quad R_{(\mu\mu)^+}^{n^-/n^+} = \frac{y_{\mu\mu}^+ \wedge y_n^-}{y_{\mu\mu}^+ \wedge y_n^+} \quad (5.3)$$



	$y_{\mu\mu}^- \wedge y_n^-$	$y_{\mu\mu}^- \wedge y_n^+$	$y_{\mu\mu}^+ \wedge y_n^+$	$y_{\mu\mu}^+ \wedge y_n^-$	$R_{(\mu\mu)^-}^{n^-/n^+}$	$R_{(\mu\mu)^+}^{n^-/n^+}$
low- $p_T J/\psi$	$78 \pm 8.8$	$47 \pm 6.8$	$81 \pm 9$	$74 \pm 8.6$	$1.66 \pm 0.31$	$0.91 \pm 0.15$
high- $p_T J/\psi$	$132 \pm 11.5$	$17 \pm 4.1$	$117 \pm 10.8$	$29 \pm 5.4$	$7.76 \pm 2.0$	$0.25 \pm 0.05$
$\mu^+ \mu^-$ from $\gamma\gamma$	$80 \pm 8.9$	$81 \pm 9$	$75 \pm 8.7$	$83 \pm 9.1$	$0.99 \pm 0.16$	$1.11 \pm 0.18$

Table 5.4: Number of dimuon pairs for different directions of the neutron rapidity direction together with  $R_{(\mu\mu)^-}^{n^-/n^+}$  and  $R_{(\mu\mu)^+}^{n^-/n^+}$ .

	$R_{(\mu\mu)^-}^{\varepsilon_{ZDC}(n^-/n^+)}$	$R_{(\mu\mu)^+}^{\varepsilon_{ZDC}(n^-/n^+)}$
low- $p_T J/\psi$	$1.59 \pm 0.29$	$0.88 \pm 0.14$
high- $p_T J/\psi$	$7.45 \pm 1.87$	$0.24 \pm 0.05$
$\mu^+ \mu^-$ from $\gamma\gamma$	$0.95 \pm 0.15$	$1.06 \pm 0.17$

Table 5.5: Ratios  $R_{(\mu\mu)^-}^{\varepsilon_{ZDC}(n^-/n^+)}$  and  $R_{(\mu\mu)^+}^{\varepsilon_{ZDC}(n^-/n^+)}$  i.e.  $R_{(\mu\mu)^-}^{n^-/n^+}$  and  $R_{(\mu\mu)^+}^{n^-/n^+}$  corrected by the ZDC<sup>+</sup> and ZDC<sup>-</sup> efficiencies.

Integrated over rapidity, separately for  $y < 0$  and  $y > 0$  ratios from Table 5.5 are shown in the Figure 5.10.

From the Tab 5.4 and the Fig. 5.9 it is seen as expected that there is no correlation between the  $J/\psi$  rapidity and neutron rapidity in the case of the low- $p_T J/\psi$  and dimuons coming from  $\gamma\gamma$  sample. In the case of the high- $p_T J/\psi$  the correlation is clearly visible.

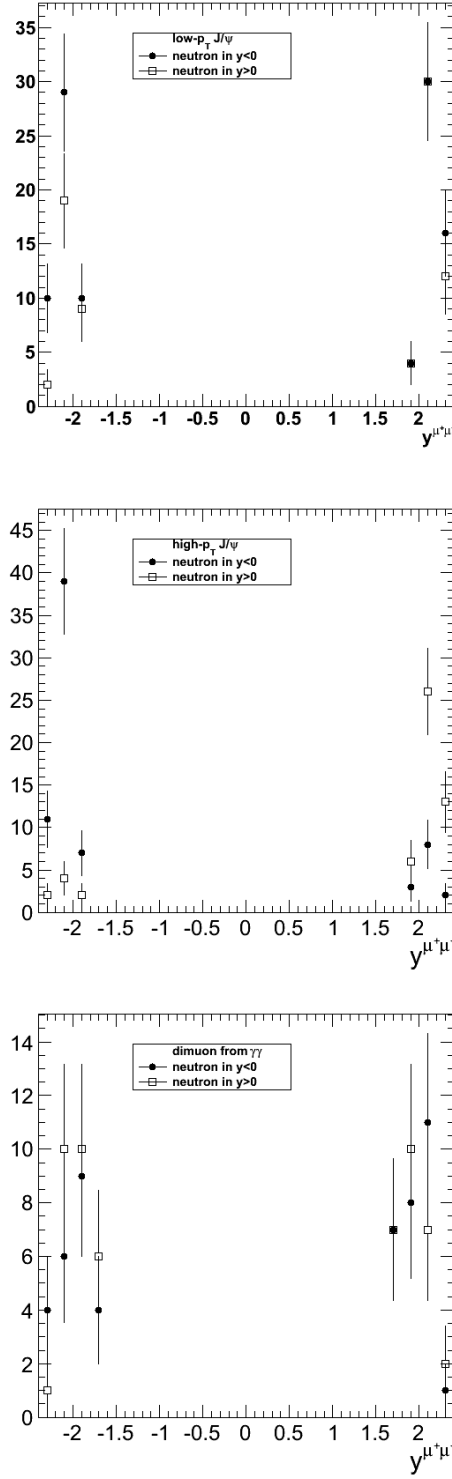


Figure 5.9: Rapidity distribution of  $J/\psi$  in the case of the events having the neutron in negative and positive rapidity for the low- $p_T J/\psi$  (top), high- $p_T J/\psi$  (middle) and dimuons from  $\gamma\gamma$  sample (bottom).

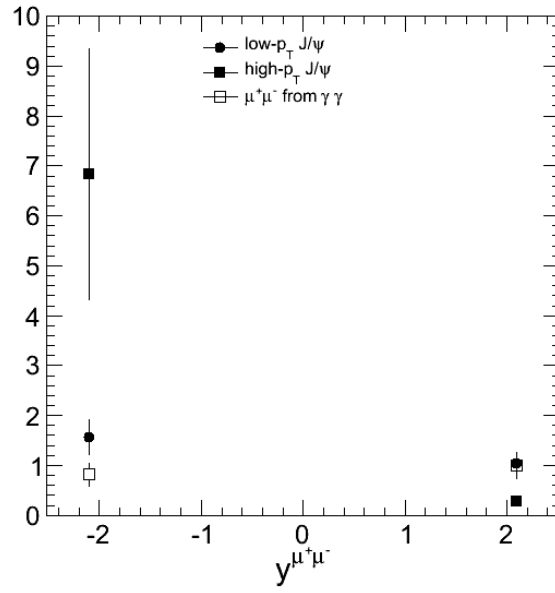


Figure 5.10:  $R^{\varepsilon_{ZDC}(n^-/n^+)}_{(\mu\mu)^-}$  and  $R^{\varepsilon_{ZDC}(n^-/n^+)}_{(\mu\mu)^+}$  integrated over one side in rapidity for low- and high- $p_T J/\psi$  and also for dimuons from  $\gamma\gamma$  sample.

# **Chapter 6**

## **Conclusion**

### **6.1 xsection results**

### **6.2 correlation results**

# Chapter 7

## Future Works

### 7.1 Studies of 2011 PbPb data

#### 7.1.1 High mass $\gamma - \gamma \rightarrow e^+ e^-$ in PbPb 2011

A study of the di-electron production in UPC events is already possible from the recorded 2011 data. This measurement would make use of the electron triggers and combined the current di-muon data with di-electron data from the triggers using the ECAL. The electron triggered sample potentially offers a large increase in statistics. By adding the additional channel the statistics would already increase. However in addition to this, because of the smaller mass of the electron, di-electron production is slightly favor compared to di-muon production. STARlight predicts that di-electron cross section is a factor of more than 2.5 higher in Xn break-up mode than the di-muons channel when looking at masses above 4 GeV. The acceptance for electrons is potential higher as well. The ECAL is position just beyond the tracker, whereas the muon system is outermost sub-detector. This elevates the main reduction of muon acceptance, which is the material budget. There is simply a lot a detector in front the muon system.

In order to perform the study several key additions would need to be made relative to the current di-muon analysis. The original reconstruction of the data used in the current di-muon analysis does not contain electron objects. Either the analysis would have to migrated to reconstruction of the

data done in a newer software version, or reconstruction of the electrons would have to be added to the current analysis chain. There are currently no electron UPC MC samples produced. In order to study the acceptance and efficiency for electrons these samples would be needed. The ultimate limitation on this study is the 2 GeV threshold in  $p_T$  in the ECAL trigger. This limits the di-electron mass range to where the trigger is efficient.

The contribution of higher order diagrams can be explored by the photoproduction of di-lepton pairs is to explore. With additional contributions to the physics communities understanding of this process this study will help to determine necessity or non-necessity of including higher order of corrections in simulations such as STARlight. Having an additional channel to help constrain the current di-muon measure of the of UPC  $\gamma - \gamma$  interaction will also help to constrain the  $J/\psi$  measurement by adding a data driven check on the normalization  $\gamma - \gamma$  background to the  $J/\psi$

### 7.1.2 UPC Hadronic Overlap and PbPb 2011

In the model calculations explored in this analysis of UPC quarkonia photoproduction all hadronic interactions are rejected. Photoproduction in events where hadronic interactions occur are not included in the cross section calculation. However, inclusive  $p_T$  spectra of  $J/\psi$  measured by ALICE in peripheral PbPb collisions show a low momentum peak consistent with coherent photoproduction [18]. CMS has the opportunity to explore this overlap between hadronic interactions and photoproduction using PbPb data from 2011 that is already recorded.

To study the overlap between photoproduction and hadronic production of quarkonia event the inelastic sample and the UPC sample could both be used. The looseness of the veto designed to reject hadronic interactions, which uses the BSC detector, leaves a significant overlap with peripheral hadronic collisions. The inclusive quarkonia sample from typical hadronic collisions can also be utilized. Coherent quarkonia photoproduction has a distinctive low  $p_T$  structure that can be used to identify photoproduced candidates in a sample that contains photoproduction combined with hadronic interactions. This measurement would open up the door to exploring the boundary between photoproduction and hadronic production. By looking at the mixing of the two, both

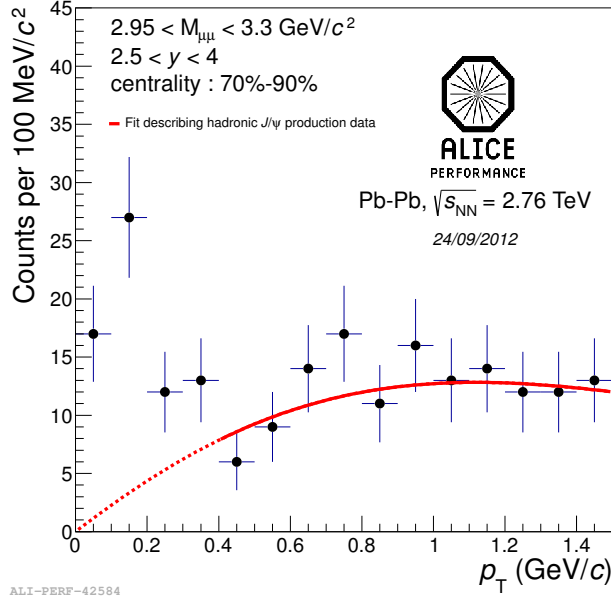


Figure 7.1: Coherent excess in inclusive  $J/\psi$   $p_T$  spectrum.

process, hadronic production and photoproduction, will be better understood.

In order to compliment each others strengths, the inclusive hadronic sample and the UPC sample of dimuon candidates would be utilized in this study. The two samples muon and centrality biases are orthogonal allowing each to serve as a check on the other. The inclusive hadronic sample is triggered by a higher  $p_T$  threshold double trigger, whereas the UPC sample is uses a lower  $p_T$  single muon trigger. The UPC sample is strongly biased toward peripheral events, which would lead to inefficiencies as events become more central, whereas, the inclusive sample is slightly biased in the most peripheral events due to an inefficiency an event selection efficiency in the most peripheral centrality bin. If these offsetting biases can be exploited, clarity about the transition between and mixing of photoproduction and hadronic production of quarkonia can be produced. A measurement of the kind proposed here will both produce a better understanding of the low  $p_T$  portion of the inclusive spectrum as well as the hadronic overlap with UPC measurements.

### 7.1.3 UPC with muons in HF

As higher rapidities are explored both lower and higher momentum partons of the nucleus are probed. Because these two contributions to the UPC photoproduction cross section can be separated using neutron tagging in incoherent events, exploring higher dimuon rapidities becomes attractive. HF extends to 5 in  $\eta$ , 2.6 units beyond the edge of the tracker. By combining hits in HF with tracks in the tracker the higher dimuon rapidities could be explored. When combined with neutron tagging of incoherently produced quarkonia, the current study can be extended to probe lower- $x$  nuclear partons by identifying muons in HF.

## 7.2 Studies of 2013 pPb data and 2015 PbPb data

Specific UPC triggers were also developed for the pPb run in 2013. For this period of running a much higher total trigger rate was read out relative to 2011. The total rate allocated for UPC triggers at the L1 in 2013 was 5kHz and 50 Hz at the HLT. This factor of 5 increase in the bandwidth, especial in L1 rate, allowed for a different triggering strategy than in 2011.

The basic strategy in 2013 was the same as in 2012, use the loosest available ECAL and muon L1 triggers to push to capture the lowest  $p_T$  electrons and muons possible and veto on hadronic interactions, but was implemented differently. Because of the L1 bandwidth restrictions in 2011, both the ZDC and the BCS were used on the L1 to reduce rates. In 2013 only the muon and ECAL triggers were used on the L1 allowing for rejection of hadronic interactions through cuts on track multiplicity. In addition, a more sophisticated trigger using full dimuon reconstructed was developed to increase purity. The main advantage in this shift in strategy was a higher purity due to the increased sophistication of the reconstruction on the HLT. In addition, an increase in cross section of the underlying physics process was achieved by relaxing the neutron emission requirement.

The HLT triggers in 2013 rejected hadronic interactions through counting tracks. For the five UPC trigger paths included in the HLT menu, three levels of reconstruction were done at the HLT.



Pixel tracks were reconstructed from the inner pixel section of the silicon tracker alone, tracks were reconstructed using the full tracker using the strips as well, and full dimuon reconstruction was done using the tracker and muon detector. The least restrictive pixel track paths required at least one track reconstructed from the pixel detector and less than 10 pixel tracks in the event. Full tracking paths were added on top of the pixel track paths and included an additional requirement of one full track and less than 7 reconstructed tracks. The most restrictive path added to the pixel and full tracking paths and required reconstruction of dimuons with a mass between 2 and 10 GeV. The design of these triggers allowed for higher signal purity relative to 2012 through use of full tracking on the HLT and allowed for increased exposure to the cross section by removing the break-up requirement implicit in requiring a ZDC trigger on the L1.

The PbPb run in 2015 will be at higher beam energies and luminosities. The  $\sqrt{s_{NN}}$  will increase from 2.76 TeV in 2011 to 5.1 TeV with a project integrated luminosity between  $0.3/nb$  and  $1/nb$ . The factor of 2 to 10 increase in integrated luminosity will increase the number of events directly. In addition, both the increase in energy, which increases the photon flux, and the ability to utilize the 2013 trigger strategy of sifting the onus of the trigger selection to the HLT will increase the measured yields relative to 2011. The higher beam energy, higher integrated luminosity, and added selectivity of the HLT will create the opportunity to explore both  $J/\psi$  with greater statistical precision and novel objects such as  $\Upsilon$ , and jets.

### 7.2.1 pPb $J/\psi$

$J/\psi$  photoproduction in pPb collisions is dominated  $\gamma - p$  interactions. The measurement would primarily probe the proton gluon densities. In Eq. 2.13 the photon flux depends on the square of the number of protons in parent nucleus,  $Z^2$ . However, the cross section of the target only increase as the total number of nucleons to the 2/3rds power,  $A^{2/3}$ . The much higher photon flux from the Pb ion more than compensates for the decreased size of the proton.

A pPb UPC  $J/\psi$  measurement will compliment the measurements done at HERA, and measurements done by ALICE. CMS will contribute by adding additional kinematic coverage and

cover a unique range of proton-photon center of mass energies,  $W_{p\gamma}$ . The difference in beam energies and species at LHC versus HERA result in access to different  $W_{p\gamma}$ . ALICE and CMS have different acceptance in  $J/\psi$  rapidity, which also translates to coverage of different  $W_{p\gamma}$ . In addition, an excess in the UPC cross section compared to HERA measurements would indicate a non-exclusive contribution to the pPb UPC  $J/\psi$  cross section. This measurement will both help enhance the current understanding of the  $p\gamma J/\psi$  photoproduction cross section as a function of  $W_{p\gamma}$ , and validate the UPCs measurements as an extension of the work done at HERA.

### 7.2.2 UPC $J/\psi$ and $\Upsilon$ in 2015

A measurement of the UPC  $J/\psi$  in 2015 will produce a strong constraint on the low- $x$  portion of the nuclear gluon distribution relative to the current analysis from the 2011 data. The  $J/\psi$  measurement will probe lower- $x$  than in 2011 due to the increase in beam energy. A measurement in 2015 will also have lower statistical errors due to the increase in integrated luminosity and increased L1 bandwidth. UPC  $J/\psi$ s in 2015 will push farther towards the onset of low- $x$  parton saturation.

Measurement of the UPC  $\Upsilon$  cross section from the 2015 data will be the first from PbPb collisions. As with the  $J/\psi$ , Additional L1 bandwidth, increased beam energy, and and intensity will increase the  $\Upsilon$  yield significantly relative to 2011. The acceptance for  $\Upsilon$  is near 40% for all rapidities between -2.4 to 2.4 (see Fig 7.2). Conversely,  $J/\psi$  acceptance is 8% near 2 in dimuon rapidity only. Below 1.6 in rapidity there is not acceptance for for UPC  $J/\psi$ . Estimates from STARlight predict a factor of 17-60 increase in yield depending on the total delivered integrated luminosity. The  $\Upsilon$  measurement will be a new measurement that will expand the range of  $x$  and  $Q^2$  probed with a higher energy probe that is better suited to the acceptance of CMS.

### 7.2.3 UPC jets

Like  $\Upsilon$ s, UPC photoproduction of jets is a novel probe. The LHC 2015 heavy ion run presents an opportunity do this measurement for the first time. The cross section for photoproduction of

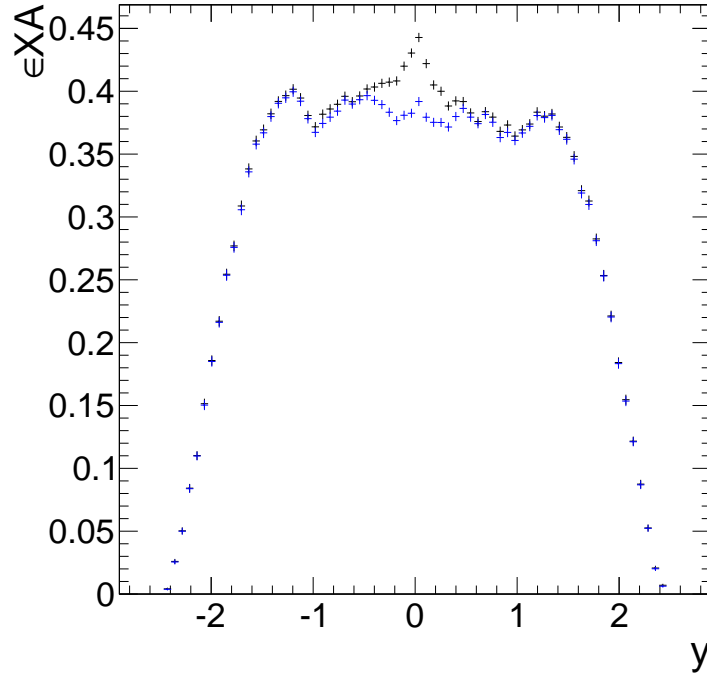


Figure 7.2:  $v$  efficiency times acceptance in CMS from STARlight for  $\sqrt{s_{NN}} = 5.1$  TeV as function of  $y$ .

jets was estimated in Ref [?] and found  $b\bar{b}$  and  $c\bar{c}$  on the order of 1 mb and 1b respectively. With the integrated luminosity expected for 2015 as many as  $1 \times 10^6$   $b\bar{b}$  events and  $1 \times 10^9$   $c\bar{c}$  events. Jet photoproduction is not constrained by the mass of the bound onia states like in  $J/\psi$  and  $\Upsilon$  photoproduction. For this reason, jet photoproduction probes a wider range of  $x$  and  $Q^2$ . UPC jets therefore will both expand on the  $J/\psi$  and  $\Upsilon$  measurements in addition to providing an additional validating compliment to the onia measurements.

The jet measurement will require additional trigger development and analysis design. The jet signal differs significantly from the dimuon signals used in the current analysis. The trigger scheme used in the 2013 pPb run selected UPC events by vetoing events with high numbers of track. The track multiplicity of the jets will not pass this requirement. However, new L1 trigger logic is currently being developed to separate the jet from the underlying event in nuclear collisions. This trigger logic could also be utilized to select jet events that produce very little to no underlying event. In addition to the trigger, jet reconstruction algorithms would needed to be adapted to push

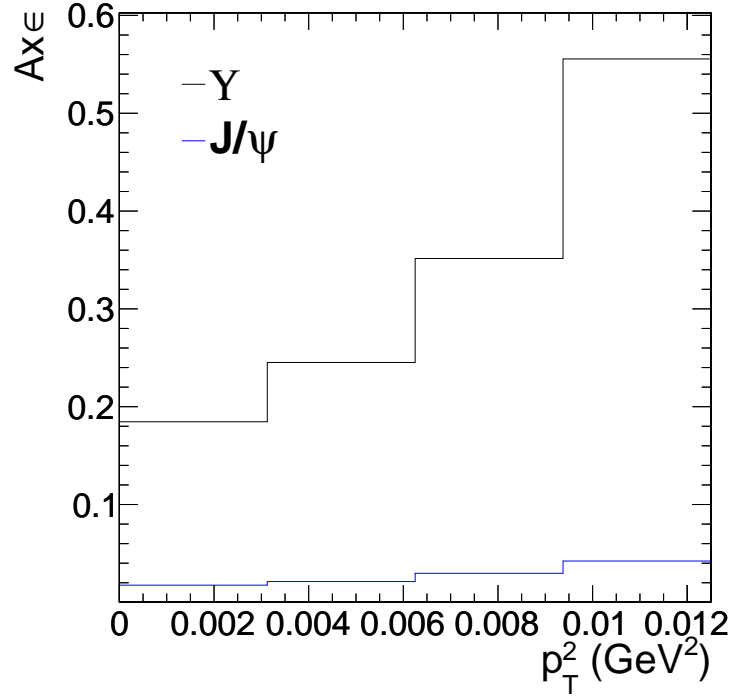


Figure 7.3: Comparison of  $\Upsilon$  and  $J/\psi$  efficiency times acceptance in CMS from STARlight for  $\sqrt{s_{NN}} = 5.1$  TeV as function of  $p_T$ .

to the lower  $p_T$  jets they are produced by photoproduction. The UPC jet measurement will demand extra preparation compared to the onia measurements, but the development will overlap with many of the goals that are already being pursued by the CMS Heavy Ion group and will allow for wider collaboration.

# References

- [1] L. McLerran, “The Color Glass Condensate and Glasma,” arXiv:0804.1736 [hep-ph].
- [2] S. Chatrchyan *et al.*, “The cms experiment at the cern lhc,” *Journal of Instrumentation* **3** no. 08, (2008) S08004. <http://stacks.iop.org/1748-0221/3/i=08/a=S08004>.
- [3] **PHENIX Collaboration** Collaboration, A. Adare *et al.*, “Cold Nuclear Matter Effects on  $J/\psi$  Yields as a Function of Rapidity and Nuclear Geometry in Deuteron-Gold Collisions at  $\sqrt{s_{NN}} = 200$  GeV,” *Phys.Rev.Lett.* **107** (2011) 142301, arXiv:1010.1246 [nucl-ex].
- [4] F. Gelis, “Color glass condensate and glasma,” *Nuclear Physics A* **854** no. 1, (2011) 10 – 17. <http://www.sciencedirect.com/science/article/pii/S0375947410006615>.  
Saturation, the Color Glass Condensate and the Glasma: What Have We Learned from RHIC?
- [5] J. D. Jackson, *Classical electrodynamics*. Wiley, New York, NY, 3rd ed. ed., 1999. <http://cdsweb.cern.ch/record/490457>.
- [6] E. Fermi, “On the Theory of Collisions between Atoms and Electrically Charged Particles,” in *Electromagnetic Probes of Fundamental Physics*, W. Marciano and S. White, eds., pp. 243–252. Sept., 2003. hep-th/0205086.
- [7] C. A. Brau, *Modern Problems in Classical Electrodynamics*. Oxford, New York, NY, 1st ed. ed., 2004.

- [8] S. R. Klein and J. Nystrand, “Exclusive vector meson production in relativistic heavy ion collisions,” *Phys. Rev. C* **60** (Jun, 1999) 014903.  
<http://link.aps.org/doi/10.1103/PhysRevC.60.014903>.
- [9] V. Rebyakova, M. Strikman, and M. Zhalov, “Coherent  $\rho$  and  $J/\psi$  photoproduction in ultraperipheral processes with electromagnetic dissociation of heavy ions at RHIC and LHC,” *Phys.Lett.* **B710** (2012) 647–653, arXiv:1109.0737 [hep-ph].
- [10] V. Rebyakova, M. Strikman, and M. Zhalov, “Coherent  $\rho$  and  $J/\Psi$  photoproduction in ultraperipheral processes with electromagnetic dissociation of heavy ions at RHIC and LHC,” *Physics Letters B* **710** no. 4–5, (2012) 647 – 653.  
<http://www.sciencedirect.com/science/article/pii/S0370269312003152>.
- [11] A. Adeluyi and C. A. Bertulani, “Gluon distributions in nuclei probed at energies available at the CERN large hadron collider,” *Phys. Rev. C* **84** (Aug, 2011) 024916.  
<http://link.aps.org/doi/10.1103/PhysRevC.84.024916>.
- [12] A. Adeluyi and T. Nguyen, “Coherent photoproduction of  $\psi$  and  $\Upsilon$  mesons in ultraperipheral pPb and PbPb collisions at the CERN Large Hadron Collider at  $\sqrt{s_{NN}} = 5$  TeV and  $\sqrt{s_{NN}} = 2.76$  TeV,” *Phys. Rev. C* **87** (Feb, 2013) 027901, arXiv:1302.4288 [nucl-th]. <http://link.aps.org/doi/10.1103/PhysRevC.87.027901>.
- [13] **ALICE** Collaboration, B. Abelev *et al.*, “Coherent  $J/\psi$  photoproduction in ultra-peripheral Pb-Pb collisions at  $\sqrt{s_{NN}} = 2.76$  TeV,” *Physics Letters B* **718** no. 4–5, (2013) 1273 – 1283.  
<http://www.sciencedirect.com/science/article/pii/S0370269312012257>.
- [14] V. Guzey, E. Kryshen, M. Strikman, and M. Zhalov, “Evidence for nuclear gluon shadowing from the ALICE measurements of pbpb ultraperipheral exclusive production,” *Physics Letters B* **726** no. 1–3, (2013) 290 – 295.  
<http://www.sciencedirect.com/science/article/pii/S0370269313006825>.
- [15] **CMS Collaboration** Collaboration, “Measurement of CMS Luminosity,”.

- [16] T. C. collaboration, “Performance of cms muon reconstruction in pp collision events at  $\sqrt{s} = 7$  tev,” *Journal of Instrumentation* **7** no. 10, (2012) P10002.  
<http://stacks.iop.org/1748-0221/7/i=10/a=P10002>.
- [17] **Particle Data Group** Collaboration, J. Beringer *et al.*, “Review of particle physics,” *Phys. Rev. D* **86** (Jul, 2012) 010001.  
<http://link.aps.org/doi/10.1103/PhysRevD.86.010001>.
- [18] A. Lardeux, “ $J/\psi$  production in Pb-Pb collisions at  $\sqrt{s_{NN}} = 2.76$  TeV in the ALICE experiment,” *J.Phys.Conf.Ser.* **446** (2013) 012042.

# **Appendix A**

## **My Appendix, Next to my Spleen**

There could be lots of stuff here